Topics in Solar Convection and Magnetic Buoyancy

Author: Abrar A. Ali

Supervisors: Lara J. Silvers

Oliver S. Kerr

Submitted in accordance with the requirements for the degree of Doctor of Philosophy

City, University of London

Department of Mathematics

October 2019

My Lord, increase me in knowledge

Contents

List of Figures

List of Tables

Acknowledgements

I wish to express my sincere and heartfelt gratitude and appreciation to my supervisor, Dr Lara Silvers, for her tireless academic supervision, unwavering support, and tenacious encouragement. Her scholarly knowledge, inspirational leadership, and invaluable experience have immensely improved my research and continue to push me to excel and challenge myself.

To Dr Oliver Kerr go my sincere thanks for his insightful discussions and valuable guidance, particularly at the initial stages of this doctoral research. His kind words have been a great source of strength for me.

I am grateful to the solar physics community for their enthusiasm, commitment, and generosity in sharing their knowledge. I would like to express my thanks to Benjamin Favier and Veronika Witzke for their useful suggestions that led to new avenues of research.

I am also grateful to my family, friends, and colleagues. Their continuous encouragement, support, and faith have made all of the difference. Finally, I wish to thank the Science and Technology Facilities Council (STFC) for funding this research.

Declaration

The candidate confirms that the work submitted is her own and that appropriate credit has been given where reference has been made to the work of others. This copy has been supplied on the understanding that it is copyright material and that no quotation from the thesis may be published without proper acknowledgement.

Abstract

Understanding and characterising the dynamics inside the Sun is vital to interpret the large diversity of complex and variable magnetic phenomena that continually appear on the solar surface. Owing to the theory of magnetohydrodynamics, many aspects of solar physics have been and continue to be investigated in order to unpuzzle the fundamental processes within the layers of the Sun. Of crucial importance, is the central role of convection that underlies the structure and features we observe of the Sun. This thesis is devoted to develop mathematical and computational modelling frameworks for the purpose of exploring the interaction of magnetic fields with granular convection in the unobservable layers of the Sun, to better understand the distributions of field over the solar surface. In particular, I aim to address the influence of convective turbulence on the emergence of solar magnetic structures.

By conducting a series of idealised numerical experiments, I first explore how small-scale turbulent pumping in the convection zone can affect properties of the large-scale buoyancy-driven magnetic field. This investigation is pursued by an extension to account for more realistic turbulent pumping configurations, where the effect of turbulent convection and magnetic buoyancy are further examined. Finally, I focus on providing an insight into how the simplifying assumptions introduced in the general modelling of thermal convection can alter the behaviour of a system.

Publications

Work from this thesis has been published in:

- Ali, A.A. and Silvers, L.J., 2018. The Effect of Time-Dependent γ-Pumping on Buoyant Magnetic Structures. *Geophysical and Astrophysical Fluid Dynamics*, **112**, 414.

Chapter 1

Introduction

1.1 The Sun: An Overview

Our Sun is a fascinatingly complex rotating body that has been a topic of interest for thousands of years (Herschel, 1795; Pugh, 2007). Its proximity to Earth gives us the ability to examine it in fine detail, unlike many other stars, while it also serves as a valuable cosmic laboratory for stellar investigations. The Sun has provided an exquisite view into the surface features and processes, in parallel to the impressive advances in theoretical and observational techniques (see Christensen-Dalsgaard, 2008, and references therein). However, the physical mechanisms underlying a plethora of dynamical phenomena observed on the Sun today remain a current outstanding problem that is yet to be fully understood.

The Sun is the sole star in our solar system formed some 4.6 billion years ago (Dziembowski *et al.*, 1999). It is a middle-aged dwarf star of stellar class G2 on the main-sequence of the Hertzsprung-Russell (HR) diagram (Battrick, 1990). The HR diagram represents the relationship between luminosity (or absolute magnitude) and effective temperature (or spectral class) for various stellar sequences. As shown in Figure 1.1, most stars are grouped along the diagonal band known as the main sequence, that spans from cool, dim stars in the bottom right to hot, luminous stars in the top left corner.

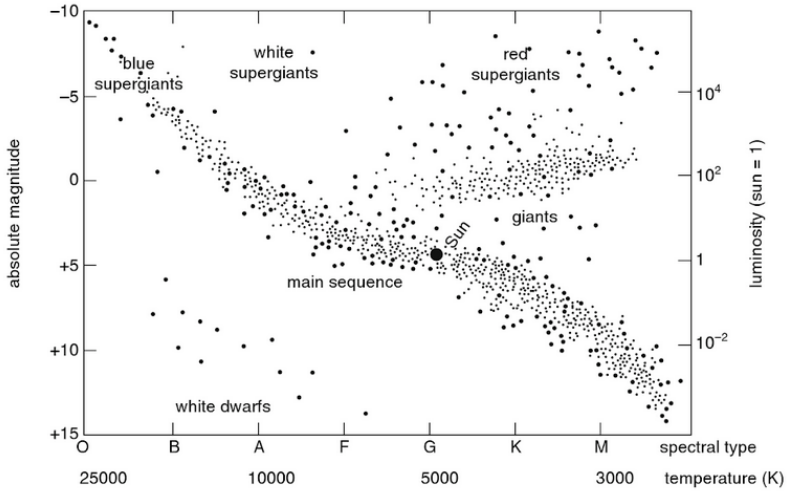

Figure 1.1: Hertzsprung-Russell (HR) diagram. The plot illustrates the various stages of stellar evolution, with the Sun positioned near the middle of the main sequence. Image taken from Vita-Finzi (2008).

The Sun consists of plasma interacting with its own solar magnetic field. It is an enormous source of heat and energy, with a surface temperature of approximately 5800 K, a total mass, $M_{\odot}$, of 1.99×10^{30} kg and a radius, $R_{\odot}$, of 6.96×10^{8} m (NASA, 2016). Like many celestial bodies, the Sun rotates on its axis but with latitude variations (Livingston and Duvall, 1978), and it rotates faster near the equator with a rotational period of 27 days compared to higher latitudes (Mullan, 2009).

Figure 1.2 shows that the Sun embodies a complex underlying structure, which is divided into different regions. Below the visible solar surface lies the solar interior, which comprises three main parts: the core, radiative zone, and convection zone. Although the solar interior is not directly accessible to observations, we have some valuable information about the internal structure. The conditions in the inner core are extreme owing to a density of order 10^5 kgm^{-3}, and a temperature of order 10^7 K (Priest, 2014). As a result of this immense pressure and sufficiently high temperature, the process of nuclear fusion takes place. Hydrogen nuclei are converted into helium nuclei every second, releasing mass in the form of energy (Priest, 2014). This tremendous energy is slowly

propelled, despite moving at the speed of light, across the radiative zone by radiation (Bhatnagar and Livingston, 2005; Ryan and Norton, 2010). Moving away from the radiative zone that extends from $0.25R_{\odot}$ to $0.7R_{\odot}$, convection becomes the predominant mechanism to transport energy.

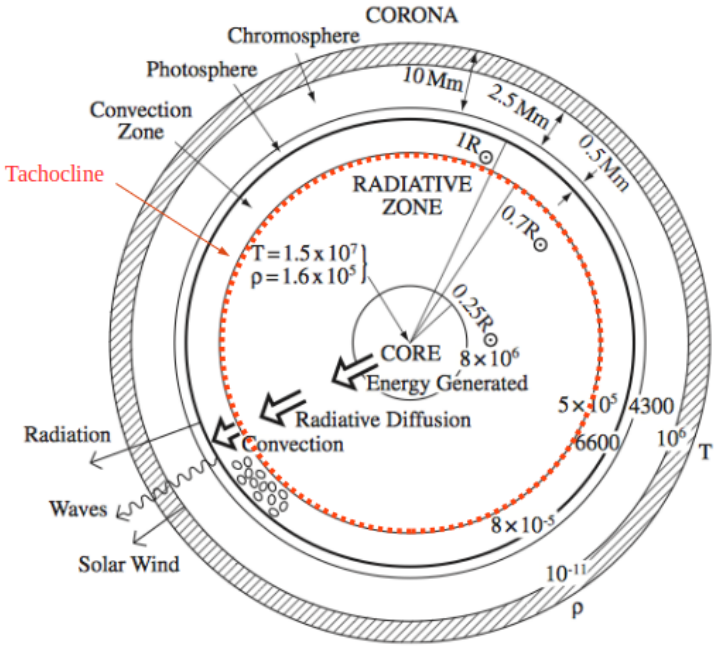

Figure 1.2: Anatomy of the Sun. Schematic illustration of the structure of the Sun, associated with the temperature, density and size of the layers. Image taken from Priest (2014) and adapted to include the tachocline layer, located at the base of the convection zone.

Above the convection zone lies the solar surface. The solar surface is distinguished as the layer with continuum optical depth unity (Heng, 2017), while for the solar atmosphere, the definition is rather ambiguous. Some authors consider the atmosphere as the photosphere, and the chromosphere (see, for example, Stix, 2002), while others extend the definition to the heliopause (Jokipii *et al.*, 1997). In this thesis, the solar atmosphere will be defined as the outer regions of the Sun, namely the photosphere, the chromosphere, and the corona.

The photosphere is the innermost thin layer of the atmosphere and is the visible surface of the Sun (Mullan, 2009). It emits the maximum intensity of

solar radiation in the form of visible light (Jenkins, 2009). The chromosphere is situated above the photosphere and is more transparent (Jenkins, 2009). The corona is the outermost region of the solar atmosphere; it is a low-density cloud of plasma with higher transparency due to temperature (Jenkins, 2009). Temperature and density decrease gradually away from the solar interior, as shown in Figure 1.2. However, at the outer regions of the chromosphere temperature rises from a minimum temperature of 4300 K to over 10^6 K in the corona (Priest, 2014; NASA, 2016). Such heating cannot be due to thermal processes as it would contradict the second law of thermodynamics. This inhomogeneous temperature problem of the solar corona is known as the coronal heating problem.

In the next subsection, a detailed discussion will be provided on parts of the Sun that are of great relevance to the current research – the base of the solar convection zone. This is followed by an overview of the vast variety of features seen on or above the solar surface.

1.1.1 The Convection Zone and Tachocline

The convection zone is the outermost region of the solar interior, and it extends from a depth of $0.7R_\odot$ to near the surface. In the convection zone, as the name implies, energy is transferred by turbulent thermal convection to the solar surface (Bhatnagar and Livingston, 2005; Ryan and Norton, 2010). Analogous to boiling water, hot plasma rises, and cooler plasma falls to be reheated and rise again (see Subsection 2.4.1 for details on the onset of convection). Generally, convection cells propagate and dissipate on four main scales: granulation, meso-granulation, supergranulation, and giant cells (Rast, 2003; Priest, 2014). The scale of the cells increases with increasing depth, due to the significant change in the pressure scale height from the bottom of the convection zone to the photosphere (Hathaway *et al.*, 2000; Proctor, 2004).

Surface manifestation of convection shows granular and supergranular scales;

the presence of meso-granulations and giant cells are suspected, but no strong evidence exists that distinctively identifies them (Hood and Hughes, 2011; Tlatov, 2012). Granular motions are visible in white light and are typically 10^6 m in diameter with vertical plasma velocities of $1-2$ kms^{-1} and lifetime of 0.2 h (Rast, 2003). Supergranular motions, on the contrary, are not visible in white light and can be detected by Doppler velocity measurements that extract the horizontal flow components (Leighton *et al.,* 1962; Muller, 2011). The typical size of a supergranular cell is about 3×10^7 m in diameter, with a lifetime of 24 h and horizontal flow speeds of $0.4-0.5$ kms^{-1} (Muller, 2011). The vertical velocity amplitude is difficult to detect for supergranules due to the effect of granulation noise, but it is reported to be very weak with downflows of order $0.05-0.1$ kms^{-1} (November *et al.*, 1981; Muller, 2011). Differential rotation within the convection zone is known to contribute towards the transport of convective cells. However, the exact internal structure of the solar differential rotation has remained unknown until the late 20th-century (Deubner *et al.*, 1979).

Over the past few decades, new methods empowered observers to look beneath the surface of the photosphere (see the review by Kosovichev, 2011). The study of acoustic wave propagation in the solar interior, namely helioseismology, contributed towards our knowledge of the internal rotation and dynamics of the Sun (Demarque and Guenther, 1999).

Figure 1.3 displays the obtained estimates of the internal rotation profile from the Helioseismic and Magnetic Imager (HMI: Schou *et al.*, 2012). Results reveal that the rotation profile is in agreement with solar surface observations, and extends in a differential manner throughout the bulk of the convection zone (Harvey, 1988). However, at the base of the convection zone, the rotation rate transitions to a latitudinally uniform rotation (Thompson *et al.*, 2003). This relatively thin ($\sim 0.04R_\odot$, c.f. Charbonneau *et al.*, 1999) transition layer that lies at the lower boundary of the convection zone exhibits an intense ra-

dial shear and is known as the tachocline (Spiegel and Zahn, 1992). Although it has been postulated for many years (see Spiegel, 1972), the solar tachocline has been of particular interest since it was proven to exist by helioseismology and more details have emerged about it. The current prevailing idea is that the tachocline plays a critical role in the evolution of the solar magnetic field (see, for example, Gilman, 2005; Hanasoge *et al.*, 2015).

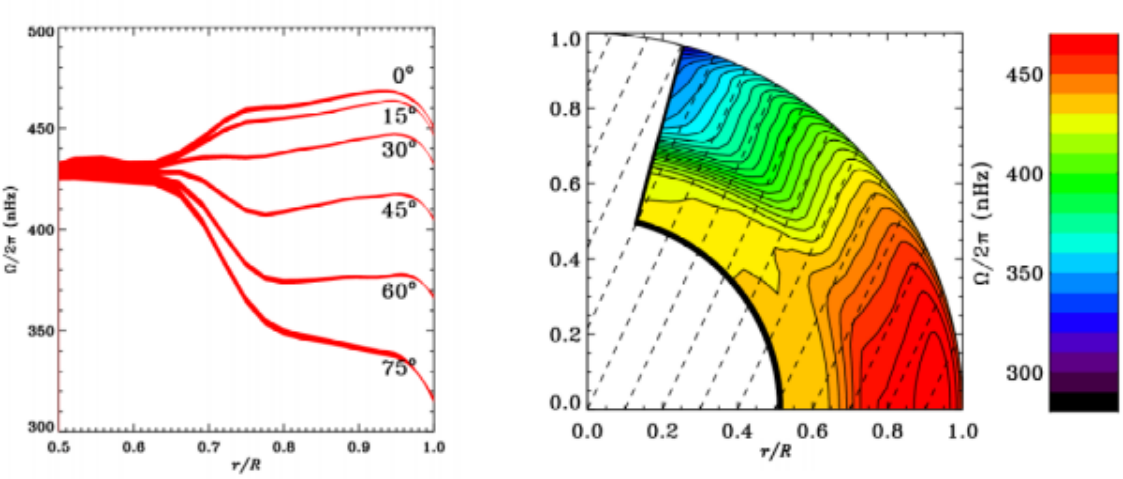

Figure 1.3: Solar internal rotation. Depth profiles of the rotation rate (left), and angular velocity isolines (right). Data is obtained with the HMI instrument onboard Solar Dynamics Observatory (SDO), and is derived from helioseismic inversion. Courtesy of GONG: Global Oscillation Network Group.

1.1.2 Magnetic Fields of the Sun

Records show that astronomers in ancient China first recorded small, dark, evolving patches on the surface of the Sun hundreds of years ago (Graham, 2000; Stewart, 2016). These observations, however, interfered with the ancient Greek beliefs (Graham, 2000; Stewart, 2016). This is because, in the West, the teaching of Greek philosopher Aristotle that heavenly objects (such as the Sun) are of unblemishing perfection and unchanging meant that such claims were impossible! Later in the 1600s, the invention of telescopes allowed scholars, namely Galileo, to witness these dark spots, later called sunspots, and their movements (Graham, 2000; Stewart, 2016). Though, some people believed sunspots were simply an astronomical transit (shadows of undiscovered

planets) (Scheiner, 1612).

With the increased observability of sunspots over the next two decades, Schwabe (1843) was able to show that the regular appearance of sunspots follows a cycle with a periodicity of approximately 11 years. The statistics of sunspot emergence revealed an equatorward propagation as the cycle advanced (Carrington, 1858). In 1904, the butterfly diagram was first constructed by Edward Maunder to monitor this migration characteristic of sunspots (see Figure 1.4).

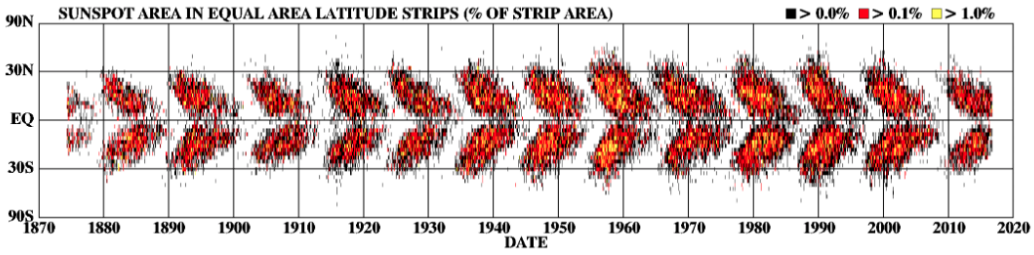

Figure 1.4: Maunder's butterfly diagram. The graph highlights the size and frequency of sunspots occurrence at different solar latitudes versus time, from the years 1874 to 2015, where the colours black, red, and yellow denotes small, medium, and large spots respectively. Image taken from Hathaway (2015).

Until the early 20th century, no evidence bridging sunspots and the magnetic field were yet found. Astronomical objects, other than the Earth, possessing a magnetic field was conclusively established owing to the discovery of George Hale. He identified sunspots as the seat of strong magnetic fields through observations of the Zeeman splitting in sunspots (Hale, 1908). This influential discovery of Hale became the gateway to understanding the dynamical role of magnetic fields in the Sun, the stars, and the universe.

Today, we know that sunspots are dark, cool regions of the solar surface (Priest, 2014). The sunspot only looks dark relative to the brightness of its surroundings, and it is cool since strong magnetic field suppresses the flow of energy from below to the surface (Mullan, 2009). Over the interval of 11 years, the solar activity changes continuously as the strong, twisted magnetic field lines,

from below, breakthrough the visible surface to form sunspot pairs of opposite polarity with a strong tendency for east-west orientation. The relative orientation of sunspot pairs is opposite with respect to the solar hemisphere (Solanski, 2003; Choudhuri, 2015).

Besides the trend of sunspots movement seen in Figure 1.4, the butterfly diagram uncovers several properties of sunspot groups (Hale *et al.*, 1919). At the beginning of a new 11 years solar cycle, the magnetic polarities of sunspot pairs located in the northern and southern hemisphere reverse. Therefore, making the full magnetic cycle repeat approximately every 22 years. In addition, the orientation of the bipolar sunspot pairs is tilted such that the leading spot is closer to the solar equator than the following spot (Davidson, 2001; Lang, 2012).

The magnetic concentrations on the surface of the Sun fuel a list of multi-scale and highly intermittent solar phenomena (see Figure 1.5). Solar flares are one of the most interesting violent eruptions on the Sun, which can provoke disruptive effects on Earth (Hanslmeier, 2007). The first ever recorded flare was observed by Carrington (1859); a flare is defined as the sudden release of intense electromagnetic radiation and energised particles into interplanetary space (Priest, 2014). Other forms of solar phenomena include prominences. A prominence is an area of relatively cool, dense loop-like gaseous structure (plasma) suspended through the ultra low-density, hot corona by a strong magnetic field (Priest, 2014). It appears bright when viewed extending from the Sun's surface, but when viewed against the body of the Sun, it appears as a dark thread-like cloud, namely filament.

These energetic solar phenomena, illustrated in Figure 1.5, are examples of the various other features perceived on the Sun. Our understanding of the magnetic Sun, through exhaustive observational and theoretical measurements, has continually developed over time. However, many questions related to the

exact nature, the complexity of the Sun's magnetic field and its unpredictable features remain a topic of investigation.

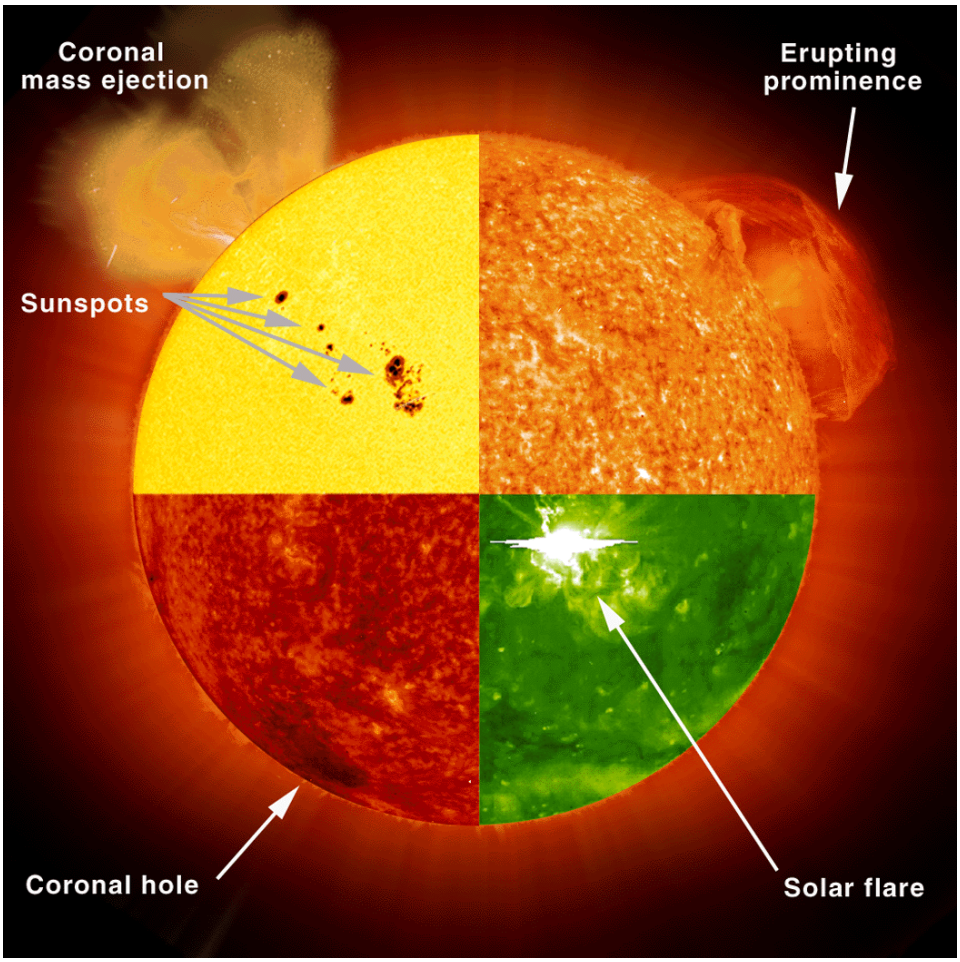

Figure 1.5: Surface features of the Sun. Active regions around sunspots trigger immense explosions, such as coronal mass ejections (CME) and solar flares. Erupting prominences are plasma structures suspended in magnetic field loops in the solar atmosphere. Dark areas called coronal holes appear in the corona, and are the source of high-speed solar wind streams. Image taken from NASA (2000).

1.2 Dynamics of the Large-Scale Solar Magnetic Field

Solar surface magnetic features, such as sunspots, appear in concentrations as opposed to in a diffuse, evenly distributed manner from below (Bumba and Suda, 1971; Solanki, 2003). In order to understand the underlying mechanism,

one must explore the interactions occurring in the layers underneath the visible layer of the Sun.

Motivated by such astrophysical problems, Thompson (1951) and Chandrasekhar (1952) conducted studies on the effect of magnetic field on convective motions, in the framework of linear stability theory. This was followed by numerical investigations of the non-linear evolution initiated by Weiss (1981). Interactions between the magnetic field and convection were found to be able to divide into magnetic and non-magnetic regions. Magnetic field is expelled in regions where vigorous convection dominates, whereas convection is suppressed in regions of concentrated magnetic field as tension of the field lines inhibit convection, and so reducing heat transport efficiency.

The dynamics of the solar convection is one of the most prominent areas of investigation, as it contains the essential ingredients for an internally-generated magnetic field, that is turbulent motions and/or differential rotation. Observations on the solar surface indicate the presence of a (large-scale) magnetic field somewhere in the convection zone. However, it is still a matter of dispute (see the review articles by Ossendrijver (2003) and Charbonneau (2014)). Additionally, the detailed mechanism for generating a magnetic field, namely solar dynamo, remains controversial (see Leighton, 1969; Charbonneau, 2005; Hood and Hughes, 2011, and references therein).

The first plausible paradigm of the large-scale solar dynamo was pioneered by Parker (1955b), when he proposed the concept of flux conversion between toroidal and poloidal components of the field. The magnetic field can be expressed using spherical polar coordinates in the following form: $\boldsymbol{B} = B_r\hat{r} + B_\theta\hat{\theta} + B_\phi\hat{\phi}$, with respect to the rotation axis of the axisymmetric astrophysical body. The $B_\phi\hat{\phi}$ term is known as the toroidal (or azimuthal) component of the magnetic field $\boldsymbol{B}_T$, whereas the sum of the remaining terms, $B_r\hat{r} + B_\theta\hat{\theta}$, is known as the poloidal component of the magnetic field $\boldsymbol{B}_P$.

Figure 1.6(a) demonstrates how differential rotation, in the toroidal direction, causes stretching of the magnetic field in the poloidal plane, thus producing a toroidal field of opposite directions in the two hemispheres. Parker (1955b) established the likely scenario to complete the solar dynamo cycle through the action of helical (small-scale) turbulence upon the toroidal magnetic field, to produce the poloidal component of the field as shown in Figure 1.6(b). Cyclonic convective motions are subject to Coriolis force that causes buoyancy-driven flux tubes, frozen into the plasma, to helically twist out and produce (large-scale) magnetic loops in the poloidal plane as displayed in Figure 1.6(c). This qualitative argument of Parker (1955b) was later interpreted in a mathematical context by Steenbeck *et al.* (1966) using the approach of mean-field theory of magnetohydrodynamics (see Subsection 2.4.3).

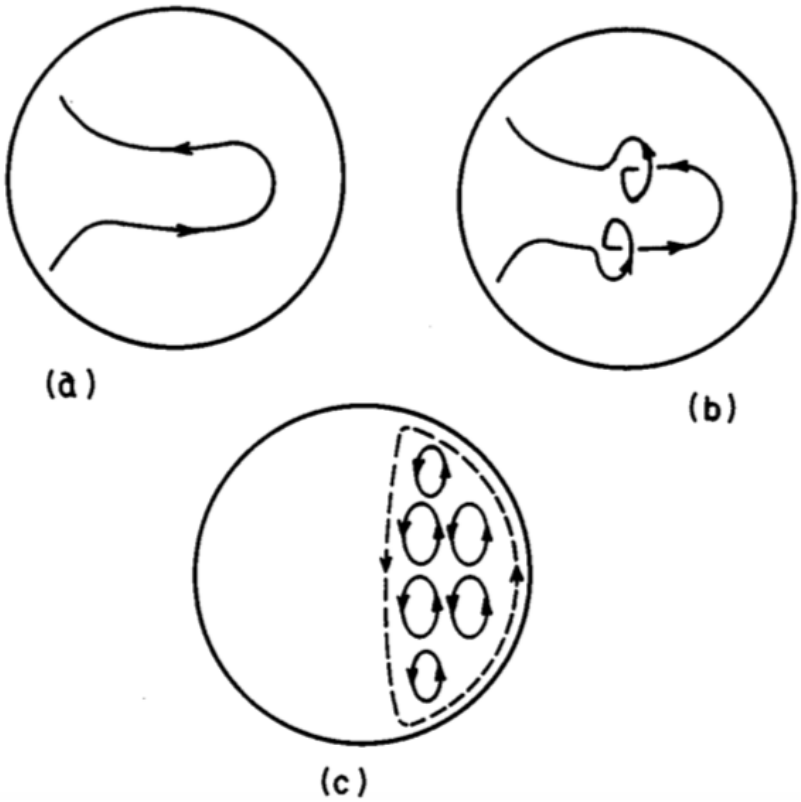

Figure 1.6: The dynamo process. The cyclic feedback loop on the poloidal and toroidal components of the magnetic field, by differential rotation and helical turbulence, propose a self-sustained dynamo. Image taken from Choudhuri (1998).

Although there are some uncertainties and discrepancies, the dynamo mechanism is believed to hold the key to understanding the dynamics of the Sun (Jones *et al.*, 2010). The site and physics of the solar dynamo is currently an active subject of research (see, for example, Tobias, 2009; Charbonneau, 2014; Brun and Browning, 2017). To date, our observational tools can only allow us to optically see magnetic fields beyond the visible surface of the Sun. Thus, to further delve into the intricate dynamics below the surface, one must seek mathematical formulations and numerical simulations.

The dynamics in the solar interior relies critically on the indirect information gained over the past years. Such includes helioseismic measurements, which deduce the profiles of temperature, pressure, density, and composition with depth. This allows one to impose constraints on standard theoretical models of the Sun (Watanabe and Shibahashi, 2001).

From the combination of theoretical models and observational methods, one can draw the following plausible picture: the generation and maintenance of the solar magnetic field involve a dynamo operating at a region of strong shear, the tachocline (Spiegel and Zahn, 1992). Large-scale magnetic field is produced in the tachocline attributable to the action of downward penetrating weak, small-scale magnetic fields generated in the convection zone and the sharp radial gradient within the tachocline (Parker, 1993). The tachocline is generally regarded as the seat of strong large-scale magnetic field due to coinciding with the quiescent radiative zone, where the destabilising actions of the magnetic field is suppressed (Spiegel and Weiss, 1980) and its exposure to overshooting convection that intrudes from above, allowing field amplification up to a commensurate level (Hughes, 2007; Priest, 2014). The possibility of large-structured magnetic fields residing in the highly buoyant convection zone is ruled out, as this would pose frequent rise of magnetic flux tubes (Parker, 1975, 1979).

Inspection of the solar photospheric layer displays strong structured magnetic fields in sunspots (see, for example, Fan, 2009), which suggests that magnetic flux tubes must be triggered by instabilities of the large-scale magnetic field in the non-turbulent tachocline, and maintain some degree of coherence through the distortion and shredding of the turbulent convection zone. One of the main issues in our knowledge, beside identifying the generation and evolution of the magnetic field, is the emergence of intense magnetic concentrations from the deep interior that imprints onto the surface of the Sun. In this thesis, I seek to develop further our understanding of the dynamics near the base of, and within, the convection zone.

This thesis is structured as follows. In Chapter 2, the essential equations that underlie the physics present within the Sun will be outlined. Chapter 3 will construct a simplified model that reflects on the interactions at the base of the convection zone, discuss numerical techniques to solve the governing equations, and present results that detail the transport of magnetic field throughout the convection zone. Chapter 4 will focus on extending the results established in Chapter 3 by modifying the model to incorporate more realistic configurations that resemble the base of the solar convection zone, and thereafter explore the dynamics of the system. In Chapter 5, attention will be directed to study the development of convective instability by devising a theoretical framework that intends to improve the modelling of thermal convection in complex systems like the Sun. This is followed by a discussion in Chapter 6, where key findings will be summarised and directions for future research will be suggested.

Chapter 2

Key Equations

In this chapter, the fundamental physical principles are applied to formulate the required governing equations. This is followed by extending the equations to magnetic fields in order to obtain the general set of equations that characterise the system of interest. Various approximation techniques and simplifying hypotheses are introduced to interpret the phenomena on desired scales.

2.1 Equations of Stellar Structure

A simple approach to explore the internal structure of astrophysical objects, such as the Sun, involves the use of stellar models for static, spherically symmetric, and homogeneous gas (see, for example, Demarque and Guenther, 1991). Within this framework, mass is assumed to vary radially according to

$$\frac{dM(r)}{dr} = 4\pi r^2 \rho(r), \tag{2.1}$$

where $M(r)$ is the mass interior to a radius r, and ρ is the density. Furthermore, stable stars (like the Sun) must obey the law of hydrostatic equilibrium, which states that all forces acting on a gas element inside the star should be very nearly in balance. This involves the balance of gravitational and pressure forces within the star

$$\frac{dp(r)}{dr} = -\frac{GM(r)}{r^2}\rho(r) = -g(r)\rho(r), \tag{2.2}$$

where p is the pressure, G is the universal gravitational constant, and g is the gravitational acceleration. Both Equations (2.1) and (2.2) determine the mechanical structure of a star in hydrostatic equilibrium. However, to obtain a closed set of equations, a relation between p and ρ, called the polytropic relation, is introduced:

$$p = K\rho^{1+\frac{1}{m}}, \tag{2.3}$$

where K is the polytropic constant, and m is the polytropic index. The above equations were formally obtained in the 19th-century, to describe a star as a polytropic self-gravitating gaseous sphere, and continue to be useful as crude approximations to more realistic stellar models (Foukal, 1990; Chandrasekhar, 2003). Introducing the dimensionless quantities

$$\rho = \rho_c\theta^m, \qquad p = p_c\theta^{m+1}, \qquad \alpha^2 = \frac{K(m+1)\rho_c^{\frac{1-m}{m}}}{4\pi G}, \qquad r = \alpha\xi, \tag{2.4}$$

where θ is the polytropic temperature, α is a length constant, ξ is a new radial variable, and subscript c denotes central values of the star, and coupling Equations (2.1)-(2.3) yield the well-known Lane-Emden equation for polytropic stars

$$\frac{1}{\xi^2}\frac{d}{d\xi}\left(\xi^2\frac{d\theta}{d\xi}\right) = -\theta^m. \tag{2.5}$$

The Lane-Emden equation provides solutions, known as polytropes of index m, that determine the stability conditions for stars over a range of stellar masses and radii. For $m \leq 1.5$, the solutions approximate an atmosphere in adiabatic convective equilibrium, such as fully convective stars, while $m > 1.5$ corresponds to stars in radiative equilibrium.

White dwarfs, fully radiative stars, or fully convective stars are well modelled as polytropes. However, to fairly approximate the Sun, one would require a composite polytropic model, such as proposed by Hendry (1993), for example. Beneath the convection zone, the solar body is believed to be in radiative equilibrium, and therefore stably stratified. Similarly, the tachocline

is believed to lie in a region of strong, stable stratification, but is additionally subject to convective overshooting. In other words, it experiences intrusion of convective plumes from the overlying unstably-stratified convection zone. Therefore, given that a small portion of the solar interior will be the main focus of this thesis, a two-layer composite polytropic model will be considered where appropriate.

2.2 Hydrodynamics

The basic hydrodynamic equations, which describe the macroscopic changes and evolution of a fluid, follow from conservation laws: the conservation of mass, the conservation of momentum, and the conservation of energy. The equations consist of the standard mass continuity equation, the Navier-Stokes equation, and the energy equation.

Mass Continuity

The equation for the mass is defined as:

$$\frac{\partial \rho}{\partial t} + \nabla \cdot (\rho \boldsymbol{u}) = 0, \tag{2.6}$$

where ρ is the fluid density, and $\boldsymbol{u}$ is the velocity field.

The Navier-Stokes equation

The Navier-Stokes equation arises from the momentum conservation, and is given by:

$$\rho\left(\frac{\partial \boldsymbol{u}}{\partial t} + (\boldsymbol{u} \cdot \nabla)\boldsymbol{u}\right) = -\nabla p + \boldsymbol{F}, \tag{2.7}$$

where p is the pressure and $\boldsymbol{F}$ indicates external forces, which includes the effect of forces such as gravitational forces, $\boldsymbol{F}_g$, and viscosity, $\boldsymbol{F}_v$. Provided that a Newtonian fluid is considered, the effect of viscosity

$$\boldsymbol{F}_v = \nabla \cdot (\mu \boldsymbol{\tau}) \tag{2.8}$$

is expressed in terms of the viscous stress tensor

$$\tau_{ij} = \frac{\partial u_i}{\partial x_j} + \frac{\partial u_j}{\partial x_i} - \frac{2}{3}\frac{\partial u_k}{\partial x_k}\delta_{ij}. \tag{2.9}$$

In Equation (2.8), μ is the dynamic viscosity and is the product of kinematic viscosity, ν, and density, i.e. $\mu = \rho\nu$.

Energy Equation

The energy equation can take different forms (see Priest 2014); in terms of the internal energy, e, this gives:

$$\rho\frac{de}{dt} + p\nabla\cdot\boldsymbol{u} = -\mathcal{L}, \tag{2.10}$$

where $\mathcal{L}$ corresponds to the net effect of energy. The internal energy in a polytropic atmosphere is defined as $e = c_v T$, where c_v is the specific heat at constant volume. Additionally, c_p is the specific heat at constant pressure and we have a relation that links c_p, c_v, and the gas constant $R_* = c_p - c_v$. Equation (2.10) can be expressed in an often more helpful form, in terms of temperature variations in time, as

$$\rho c_v\frac{\partial T}{\partial t} + \rho c_v(\boldsymbol{u}\cdot\nabla T) + p\nabla\cdot\boldsymbol{u} = -\mathcal{L}, \tag{2.11}$$

where T is the temperature. Including the relevant components of $\mathcal{L}$,

$$\mathcal{L} = \nabla\cdot\boldsymbol{q} - H_v, \tag{2.12}$$

where $\boldsymbol{q} = -K\nabla T$ is the heat flux (K is the heat conductivity), and $H_v = \mu\tau^2/2$ is the viscous heating. The energy equation reads

$$\rho c_v\left(\frac{\partial T}{\partial t} + (\boldsymbol{u}\cdot\nabla T)\right) = -p\nabla\cdot\boldsymbol{u} + \nabla\cdot\big(K\nabla T\big) + \frac{\mu\tau^2}{2}. \tag{2.13}$$

Perfect Gas Law

Throughout the thesis, the fluid is assumed to obey the equation of state for a perfect gas, that links temperature, density, and pressure

$$p = R_* \rho T, \tag{2.14}$$

where R_* is the gas constant.

2.3 Magnetohydrodynamics

Matter in stellar interiors exists in the plasma state. With the purpose of understanding the dynamics of the solar interior and the magnetic features observed on the outer parts of the Sun, we require the magnetohydrodynamics (MHD) equations. MHD equations are a self-consistent framework that enables us to detail the large-scale dynamics of space plasmas in modern astrophysical problems (Powell *et al.*, 2003; Zhang and Feng, 2016).

The governing equations, stated below, follow from the complete set of Maxwell's equations coupled with the equations of mass, momentum and energy, described in Section 2.2, together with Ohm's law. This includes the induction equation, which is of vital importance to determine the evolution of the magnetic field $\boldsymbol{B}$[1], derived by eliminating the electric fields $\boldsymbol{E}$ in Faraday's law, Ampère's law, and Ohm's law. The induction equation will be derived below based on Fearn (2013) and Priest (2014).

[1]To be precise, $\boldsymbol{B}$ is the magnetic induction but is commonly referred to as the magnetic field (Fearn, 2013).

Maxwell's Equations

Maxwell's equations are the governing equations for magnetic and electric fields. In *mks* units, these are

$$\nabla \cdot \boldsymbol{B} = 0, \qquad \text{(Gauss' law for magnetism)} \tag{2.15a}$$

$$\nabla \cdot \boldsymbol{E} = \frac{\rho_c}{\epsilon_0}, \qquad \text{(Gauss' law)} \tag{2.15b}$$

$$\frac{\partial \boldsymbol{B}}{\partial t} = -\nabla \times \boldsymbol{E}, \qquad \text{(Faraday's law)} \tag{2.15c}$$

$$\frac{1}{c^2}\frac{\partial \boldsymbol{E}}{\partial t} = \nabla \times \boldsymbol{B} - \mu_0 \boldsymbol{j}, \qquad \text{(Ampère's law)} \tag{2.15d}$$

under the relations $\boldsymbol{B} = \mu_0 \boldsymbol{H}$ and $\boldsymbol{D} = \epsilon \boldsymbol{E}$, to eliminate the magnetic field strength $\boldsymbol{H}$ and the electric displacement field $\boldsymbol{D}$. The permittivity, ϵ_0, and magnetic permeability, μ_0, are approximated by their values in free space.

The equations of MHD, together with appropriate boundary conditions, form a complicated set of coupled differential equations, thus making it essential to reduce the system further by including simplistic assumptions that are appropriate for modelling the inside of the Sun. A fundamental assumption for many astrophysical applications, known as the MHD approximation, is that relative velocities are minimal compared to the speed of light, $c = 1/(\epsilon_0 \mu_0)^2$. One consequence of this relation is the reduction of Ampère's law (Equation 2.15d) to

$$\nabla \times \boldsymbol{B} = \mu_0 \boldsymbol{j}. \tag{2.16}$$

Ohm's Law

Ohm's law is a relation between electric field and current density. In a moving conductor, the total electric field is proportional to the current density $\boldsymbol{j}$. Further to the electric field $\boldsymbol{E}$ acting on a medium at rest, plasma moving with velocity $\boldsymbol{u}$ is subject to an electric field $\boldsymbol{u} \times \boldsymbol{B}$. Hence,

$$\boldsymbol{j} = \sigma(\boldsymbol{E} + \boldsymbol{u} \times \boldsymbol{B}), \tag{2.17}$$

where σ is the electrical conductivity.

The Induction Equation

The induction equation plays a fundamental role in determining the behaviour of a magnetic field $\boldsymbol{B}$. The induction equation is derived as follows: starting with the reduced form of Ampère's law (Equation 2.16) and Ohm's law (Equation 2.17), one obtains

$$\eta \nabla \times \boldsymbol{B} = (\boldsymbol{E} + \boldsymbol{u} \times \boldsymbol{B}), \tag{2.18}$$

where $\eta = 1/(\sigma\mu_0)$ is the magnetic diffusivity. Taking the curl of Equation (2.18) implies that

$$\nabla \times \big(\eta \nabla \times \boldsymbol{B}\big) = \nabla \times \boldsymbol{E} + \nabla \times (\boldsymbol{u} \times \boldsymbol{B}). \tag{2.19}$$

Given Gauss' law for magnetism (Equation 2.15a) and Faraday's law (Equation 2.15c), Equation (2.19) reads

$$\frac{\partial \boldsymbol{B}}{\partial t} = \nabla \times (\boldsymbol{u} \times \boldsymbol{B} - \eta \nabla \times \boldsymbol{B}). \tag{2.20}$$

The above equation consists of the principal quantities in MHD, $\boldsymbol{u}$ and $\boldsymbol{B}$, and is known as the induction equation.

Modified hydrodynamical equations

To form a complete set of MHD equations, the significant contribution of the magnetic field to the evolution of the system must be taken into account. Returning to the basic hydrodynamic equations introduced in Section 2.2, an additional forcing term appears for the magnetised plasma in the Navier-Stokes equation (Equation 2.7), known as the Lorentz force,

$$\boldsymbol{F}_l = \boldsymbol{j} \times \boldsymbol{B}. \tag{2.21}$$

Using the relation deduced from Ampère's law (Equation 2.16) and vector identity $\nabla(\boldsymbol{A}\cdot\boldsymbol{B}) = (\boldsymbol{A}\cdot\nabla)\boldsymbol{B} + (\boldsymbol{B}\cdot\nabla)\boldsymbol{A} + \boldsymbol{A}\times(\nabla\times\boldsymbol{B}) + \boldsymbol{B}\times(\nabla\times\boldsymbol{A})$, $\boldsymbol{F}_l$ can be decomposed into two terms. The magnetic pressure force, $\nabla|\boldsymbol{B}|^2/2\mu_0$, and the magnetic tension force, $(\boldsymbol{B}\cdot\nabla)\boldsymbol{B}/\mu_0$, that acts only when field lines are curved. Thus, the Navier-Stokes equation (Equation 2.7) is modified to

$$\rho\left(\frac{\partial \boldsymbol{u}}{\partial t} + (\boldsymbol{u}\cdot\nabla)\boldsymbol{u}\right) = -\nabla p - \nabla\left(\frac{|\boldsymbol{B}|^2}{2\mu_0}\right) + \frac{(\boldsymbol{B}\cdot\nabla)\boldsymbol{B}}{\mu_0} + \nabla\cdot\mu\boldsymbol{\tau} + \boldsymbol{F}_g. \quad (2.22)$$

Furthermore, Ohmic dissipation, $|j|^2/\sigma$, is an additional source of energy and is incorporated into the energy equation (Equation 2.13) to become

$$\rho c_v\left(\frac{\partial T}{\partial t} + (\boldsymbol{u}\cdot\nabla T)\right) = -p\nabla\cdot\boldsymbol{u} + \nabla\cdot\big(K\nabla T\big) + \frac{\eta|\nabla\times\boldsymbol{B}|^2}{\mu_0} + \frac{\mu\tau^2}{2}. \quad (2.23)$$

2.4 Instabilities, Turbulence and Mean-Field Theory

Convection is an important physical process in which thermal energy is transferred by the motion of a fluid. Resulting from the large gradients in temperature, together with gravity, convective flows are often present in atmospheres of celestial bodies such as stellar interiors, and accretion disks. Convectively driven flows within stars like the Sun are considered turbulent, rather than laminar, and are important for the generation of a large-scale magnetic field through dynamo action (refer to Section 1.2).

2.4.1 Convective Instability

The onset of convective instabilities crucially depends on the characteristics of the fluid. Suppose a perfect gas in hydrostatic balance in a uniform gravitational field. With the direction of the vertical coordinate, z, chosen opposite to the direction of gravity, density $\rho(z)$ and pressure $p(z)$ are expected to decrease with height z. Now, assume a parcel of gas in equilibrium with the ambient medium, i.e. density ρ and pressure p are the same as the surroundings. By

considering a small vertical displacement of the parcel against gravity, as illustrated in Figure 2.1, the parcel deviates to a surrounding environment of lower density and pressure, ρ' and p' respectively. Acoustic waves quickly diminish the imbalance of pressure and so, engender an adiabatic expansion of the parcel to reach pressure equilibrium (Clarke and Carswell, 2007). However, heat exchange takes place rather slowly, which results in a change of temperature inside the parcel and hence to the density at the new position, ρ^*. If $\rho^* > \rho'$, then the displaced parcel will tend to sink back to its original position, and the gas is said to be stable against convection. If $\rho^* < \rho'$, the parcel will rise due to buoyancy force (according to Archimedes' principle), and the gas is said to be convectively unstable.

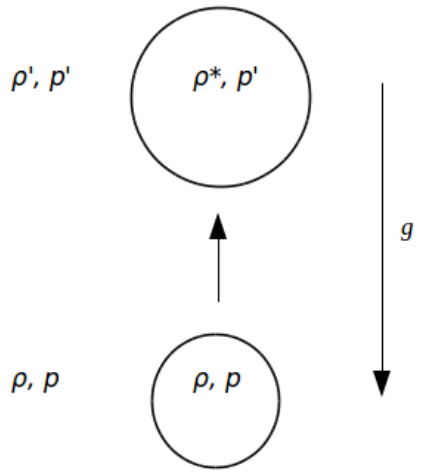

Figure 2.1: Convective instability. Illustration of a rising parcel of gas in a stratified environment.

Mathematically, the stability of the system can be expressed by looking at the density difference. In a perfect gas, this is given by

$$\rho^* - \rho' = \left[-\left(1 - \frac{1}{\gamma_s}\right)\frac{\rho}{p}\frac{dp}{dz} + \frac{\rho}{T}\frac{dT}{dz}\right]\Delta z. \tag{2.24}$$

Here $\gamma_s = c_p/c_v$ is the adiabatic index, where c_p is the specific heat at constant pressure, and c_v is the specific heat at constant volume. Noting that the gradients of pressure and temperature are negative, the system is stable against

convection if

$$\left|\frac{dT}{dz}\right| < \left(1 - \frac{1}{\gamma_s}\right)\frac{T}{p}\left|\frac{dp}{dz}\right|. \tag{2.25}$$

This value of dT/dz is known as the adiabatic temperature gradient, while the above condition (Equation 2.25) is known as the Schwarzschild instability criterion (Schwarzschild, 1906). By solving a simplified momentum equation of the gas parcel, the behaviour can also be expressed in terms of a buoyancy frequency, known as the Brunt-Väisälä frequency,

$$N = \pm\sqrt{\frac{g}{T}\left[\frac{dT}{dz} - \left(1 - \frac{1}{\gamma_s}\right)\frac{T}{p}\frac{dp}{dz}\right]}. \tag{2.26}$$

The quantity N is the frequency of oscillation, and it determines the behaviour of the solution. If $N \in \mathbb{R}$, the gas is convectively stable, and the solutions are oscillations. If $N \in \mathbb{C}$, the gas is convectively unstable, and the solutions represent an exponentially decaying and an exponentially growing mode (Choudhuri, 1998).

Strictly speaking, the above analysis for stability is simplified. In particular, the conditions for stability are sensitive to disturbances, in addition to radiative diffusion and conduction within the gas parcel. A more general criterion for instability can be provided in terms of the dimensionless Rayleigh number (Rayleigh, 1916; Jeffreys, 1926)

$$Ra = \frac{gd^4}{\nu K}\left(\alpha\left|\frac{dT}{dz}\right|\right), \tag{2.27}$$

where d denotes the depth of the domain, and ν, K, and α are respectively the coefficients of kinematic viscosity, thermal conductivity, and volume expansion. For a given system, and depending on the boundary conditions, there must exist a critical Rayleigh number, Ra_c, above which the system is linearly unstable, and oscillatory patterns arise. For growing Ra values, convection is likely to become more vigorous. A more detailed discussion of the derivation and analysis are contained in Chandrasekhar (1961) and Stix (2002).

2.4.2 Magnetic Buoyancy

Due to stretching caused by differential rotation, magnetic field beneath the radiating surface is presumed to exist in the form of toroidal flux tubes of strong field concentration. Assume an isolated flux tube with magnetic field strength, B, internal gas pressure, $p_{\rm in}$, and external gas pressure, $p_{\rm ext}$. In order to maintain pressure equilibrium between the flux tube and its surrounding atmosphere,

$$p_{\rm ext} = p_{\rm in} + \frac{B^2}{2\mu_0}, \tag{2.28}$$

must be satisfied. In thermal equilibrium, the above equation implies that the density in the region of the field is less than the surrounding density, i.e. $\rho_{\rm ext} \geq \rho_{\rm in}$. If such configuration takes place in parts of the toroidal magnetic flux tube, then the tube would experience a buoyant force and rise against the gravitational field. This classic transport mechanism is known as magnetic buoyancy instability and was introduced by Parker (1995a) in a discussion of sunspots formation by instabilities associated with the deep-seated solar toroidal field below the surface, and is invoked in most models of solar dynamo.

2.4.3 Mean-Field Approximation

Turbulence is one of the most unpredictable physical phenomena, underlying the complicated and irregular motion of rapidly evolving fluids, that can contribute to many different length-scales significantly (see, for example, Yoshizawa *et al.*, 2002). A physical representation of a fluid, from small to large scales, remains notoriously difficult to contain in one consistent framework. Within the theory of mean-field approximation, the behaviour of the large-scale fields due to small-scale turbulence is described by parameterising the effects of turbulence. This statistical approach is one plausible way of handling turbulence in the solar context, since complexity within the highly turbulent solar convection zone, for example, poses a broad spectrum of dynamical scales to be present.

In view of the definition by Steenbeck *et al.* (1966), the magnetic and velocity fields can be decomposed in terms of mean and fluctuating parts:

$$\boldsymbol{B} = \bar{\boldsymbol{B}} + \boldsymbol{B}', \qquad \boldsymbol{u} = \bar{\boldsymbol{u}} + \boldsymbol{u}', \tag{2.29}$$

where

$$\bar{\boldsymbol{u}'} = \bar{\boldsymbol{B}'} = 0. \tag{2.30}$$

Here, the overline denotes the mean part of the corresponding field, and the prime corresponds to the fluctuating part of the fields. Generally, the mean quantities follow from defining an appropriate averaging procedure (e.g. spatial, temporal, ensemble), whereby the average is taken over scales sufficiently larger than the turbulent eddy scales.

Accordingly, the induction equation (Equation 2.20) can be expressed as

$$\frac{\partial(\bar{\boldsymbol{B}} + \boldsymbol{B}')}{\partial t} = \nabla \times ((\bar{\boldsymbol{u}} + \boldsymbol{u}') \times (\bar{\boldsymbol{B}} + \boldsymbol{B}') - \eta \nabla \times (\bar{\boldsymbol{B}} + \boldsymbol{B}')). \tag{2.31}$$

By spatially averaging the terms in Equation (2.31) over some intermediate length-scale, following Reynolds rules (see, for example, Hoyng, 2012), the mean-field induction equation is derived. That is,

$$\frac{\partial \bar{\boldsymbol{B}}}{\partial t} = \nabla \times (\bar{\boldsymbol{u}} \times \bar{\boldsymbol{B}} + \mathcal{E} - \eta \nabla \times \bar{\boldsymbol{B}}), \tag{2.32}$$

where $\mathcal{E} = \overline{\boldsymbol{u}' \times \boldsymbol{B}'}$ is the mean electromotive force (e.m.f.) due to fluid velocity and magnetic field fluctuations. This mean e.m.f., $\mathcal{E}$, allows the system to behave differently from laminar fields and so plays a vital role in turbulent dynamo (Moffatt, 1978, 1983; Krause and Radler, 1980). By taking the difference of Equations (2.31) and (2.32), an equation for the magnetic fluctuation is deduced:

$$\frac{\partial \boldsymbol{B}'}{\partial t} = \nabla \times (\boldsymbol{u}' \times \bar{\boldsymbol{B}} + \bar{\boldsymbol{u}} \times \boldsymbol{B}' + \boldsymbol{u}' \times \boldsymbol{B}' - \mathcal{E} - \eta \nabla \times \boldsymbol{B}'). \tag{2.33}$$

Suppose the small-scale field $\boldsymbol{B'}$ is zero at $t = 0$, then a linear relation can consequently be established between the mean field $\bar{\boldsymbol{B}}$ and mean e.m.f $\mathcal{E}$, if no magnetic fluctuation at small scales ($\boldsymbol{B'} = 0$) is present. Let us further assume the spatial scale of fluctuation to be small compared to that of the mean field. This implies that $\mathcal{E}$ can be represented in the form of a Taylor expansion:

$$\mathcal{E}_i = \alpha_{ij}\bar{B}_j + \beta_{ijk}\frac{\partial \bar{B}_j}{\partial x_k} + \gamma_{ijkl}\frac{\partial^2 \bar{B}_j}{\partial x_k \partial x_l} + ... + a_{ij}\frac{\partial \bar{B}_j}{\partial t} + b_{ijk}\frac{\partial^2 \bar{B}_j}{\partial x_k \partial t} + ..., \quad (2.34)$$

where α_{ij}, β_{ijk}, γ_{ijkl} are pseudo-tensors that depend on properties of the flow. Reducing Equation (2.34) to first-order spatial derivative terms gives

$$\mathcal{E}_i = \alpha_{ij}\bar{B}_j + \beta_{ijk}\frac{\partial \bar{B}_j}{\partial x_k}. \quad (2.35)$$

At this stage, it is necessary to specify the form of α_{ij} and β_{ijk}, and so determine their effect in the evolution of the mean magnetic field. Due to the lack of adequate knowledge on convective turbulence, the simplest case is considered where the mean flow is zero, $\bar{\boldsymbol{u}} = 0$, and fluctuations in the velocity field, $\boldsymbol{u'}$, correspond to homogeneous and isotropic turbulence. That is such

$$\alpha_{ij} = \alpha\delta_{ij} \quad \text{and} \quad \beta_{ijk} = -\beta\epsilon_{ijk}, \quad (2.36)$$

where α is a pseudo-scalar, β is a scalar, δ_{ij} is the Kronecker tensor, and ϵ_{ijk} is the Levi-Civita tensor. Thus, back to Equation (2.35), the mean e.m.f. for homogeneous isotropic turbulence reads

$$\mathcal{E}_{\boldsymbol{A}} = \alpha\bar{\boldsymbol{B}} - \beta\nabla \times \bar{\boldsymbol{B}}. \quad (2.37)$$

By assuming inhomogeneity and anisotropy on the turbulent flow, one can provide an alternative representation of $\mathcal{E}$. In this case, the coefficients α_{ij} and β_{ijk} may be split into symmetric and antisymmetric parts. Given that the main focus is on terms up to first order, the α-tensor is only expressed into

symmetric and antisymmetric components, i.e.

$$\alpha_{ij} = \alpha_{ij}^{(S)} + \alpha_{ij}^{(A)} = \alpha\delta_{ij} - \epsilon_{ijk}\gamma_k, \tag{2.38}$$

so that,

$$\alpha_{ij}^{(A)}\bar{B}_j = (\boldsymbol{\gamma} \times \boldsymbol{B})_i. \tag{2.39}$$

From this, the mean e.m.f. equation for inhomogeneous anisotropic turbulence is obtained:

$$\mathcal{E}_{\boldsymbol{B}} = \alpha\bar{\boldsymbol{B}} - \boldsymbol{\gamma} \times \bar{\boldsymbol{B}} - \beta\nabla \times \bar{\boldsymbol{B}}, \tag{2.40}$$

where

$$\alpha = -\frac{\tau}{3}\overline{\boldsymbol{u}' \cdot (\nabla \times \boldsymbol{u}')},$$

$$\beta = \frac{\tau}{3}\overline{\boldsymbol{u}' \cdot \boldsymbol{u}'},$$

and

$$\boldsymbol{\gamma} = -\frac{\tau}{3}\nabla\overline{\boldsymbol{u}' \cdot \boldsymbol{u}'},$$

are the dynamo coefficients. Here the term α depends on helical flows associated to turbulence, and so the "α-effect" presents the twisting of the average field driven by helical turbulent convection, where τ is the correlation time for turbulence. The β-effect denotes the diffusive transport of $\bar{\boldsymbol{B}}$ arising from turbulence and is also known as turbulent diffusivity. Lastly, the γ-effect corresponds to the additive advection of mean magnetic field by inhomogeneous turbulence with pumping velocity $\boldsymbol{\gamma}$.

In conjunction with the specification of the dynamo-coefficients and definition of the mean flow $\bar{\boldsymbol{u}}$, the mean-field induction equation (Equation 2.32) can be solved to determine the evolution of the mean magnetic field $\bar{\boldsymbol{B}}$. This framework provides a simple, parametric modelling approach to tackle challenging questions associated with the role of turbulence in layers inaccessible to direct observations, and to explain many of the observed features on the Sun.

Chapter 3

The Effect of γ-Pumping On Buoyant Magnetic Structures

3.1 Introduction

Perceived magnetic features on, and above, the surface of the Sun have given rise to a number of open questions concerning the mechanisms responsible for the generation, maintenance, and emergence of magnetic fields from the deep interior to the visible surface of the Sun (Zwaan, 1985; Solanki, 2003; Silvers, 2008). To address these topics, numerous investigations have been undertaken (see, for example, Parker, 1993; Dikpati and Gilman, 2001; Tobias and Weiss, 2007, and references therein), and it has become clear that the tachocline region, which is located just beneath the convection zone, is a crucial component of both the dynamo mechanism and also in the formation of strong structures that emerge to form magnetic phenomena at the solar surface (see, for example, Spiegel and Zahn, 1992; Gilman, 2005; Christensen-Dalsgaard and Thompson, 2007).

The solar tachocline proves to be a region of great dynamical interest. It is regarded as the seat of strong, large-scale toroidal magnetic field and is a region of intense radial gradient (Charbonneau, 2010). Magnetic structures must be generated in this region and retain their coherence throughout the turbulent

convection zone, in order to reach the solar surface and give rise to sunspots and other magnetic features. A key outstanding issue is to understand how structures are formed with sufficient intensity, and on an appropriate timescale, in the tachocline to emerge into the turbulent convection. While more recent research has focused on the formation of solar surface magnetic concentrations within the convection zone itself (Perri and Brandenburg, 2018), a substantial body of literature has sought to examine magnetic buoyancy instabilities of a shear-generated magnetic field (see, for example, Cline *et al.*, 2003; Vasil and Brummell, 2008; Silvers *et al.*, 2009, and references therein). For the sake of simplicity, many of these calculations investigate buoyant magnetic tubes in isolation, i.e. by neglecting the presence of an overlying convective layer. However, to develop an enhanced picture of the dynamics, it is essential to consider and understand the evolution of magnetic structures in the presence of convection.

Previous studies of the interaction between buoyant magnetic flux structures and convection (Nordlund *et al.*, 1992; Brandenburg *et al.*, 1996; Tobias *et al.*, 1998, 2001) have explored the influence of turbulent convection on the transport and storage of the underlying magnetic field. In their frameworks, they achieve a radial pumping that arises naturally from the turbulent convective flow. However, resulting from the complex interactions in these models, it is difficult to extract more general phenomena that permit global features, particularly the emergence of magnetic flux structures, to take place. A small number of studies have implemented the simpler approach of parameterising the pumping effects observed in magnetoconvection simulations using the theory of mean-field electrodynamics (refer to Subsection 2.4.3), to capture such global features (see, for example, Ossendrijver *et al.*, 2002). This so-called γ-pumping implies a secondary advection term of the mean magnetic field relative to the flow and can be characterised to describe properties of the turbulent convective flow without the associated complications of full convection calculations (Moffatt, 1983; Tobias *et al.*, 2001).

Theoretical investigations of turbulent transport coefficients, including the turbulent γ-pumping effect, have been previously studied (see Krause and Rädler, 1980; Moffatt, 1983; Kichatinov, 1991; Brandenburg and Subramanian, 2005). Vertical pumping mechanisms are long known to play a prominent role in the maintenance and generation of the solar magnetic field; the pumping effect is found to expel magnetic flux from regions associated with strong turbulence and so, is also known as the diamagnetic effect (Zel'dovich, 1957). However, the role of turbulent pumping in the horizontal direction did not receive adequate attention, though its existence has been suggested from symmetry considerations in the context of mean-field electrodynamics (Krause and Rädler, 1980) and from analytical calculations using the first order smoothing approximation (FOSA) (Kichatinov, 1991).

The first insight into the non-radial γ-pumping in a numerical framework was performed by Ossendrijver *et al.* (2002). Their work revealed interesting measures of the directional-dependent turbulent pumping. Latitudinally, for instance, the pumping effects of the mean toroidal field favour an equatorward motion which may indicate the propagation of emerging sunspots as a result of such pumping, rather than to meridional circulations.

Recently, Barker *et al.* (2012) carried out the γ-pumping approach in their model in order to capture the dynamics of overshooting convection on buoyant magnetic structures forming in the tachocline. Results from their numerical calculations establish an equipartition relation between the magnetic field and the γ-pumping under which the evolution of the large-scale field is determined; proposing a plausible mechanism of restraining and intensifying the magnetic field before buoyancy instabilities play a significant role in the emergence of flux structures. However, their investigation in this framework was preliminary as several features were not included and therefore may not capture the entire picture of the dynamics of the magnetic field in the presence of tur-

bulent convection. Turbulent motions naturally depend on variables of time and space (Toomre *et al.*, 1984; Weiss *et al.*, 1996, 2004), and it is unclear how the system would evolve if the static pumping profile in the Barker *et al.* (2012) model were extended to account for temporal characteristics. A time-dependent γ-pumping will lead to temporal variations in the mean downward force and hence, the equipartition value. The research presented here will build on the work of Barker *et al.* (2012) by exploring the effect of time-dependent pumping on the formation and evolution of magnetic structures.

3.2 Model and Method

To investigate the dynamics within the Sun, it is possible to study the interaction acting at local scales or otherwise global scales. Global-scale modelling, however, cannot capture the many processes that occur over a large range of spatiotemporal scales, and so would require scale-truncation conditions (see, for example, Browning *et al.* 2006). Local-scale investigations, where a small portion of the region of interest is considered, can provide a more detailed description. For example, instabilities due to magnetic buoyancy are thought to act primarily locally. Therefore, a local three-dimensional Cartesian domain of electrically conducting, compressible fluid will be considered here, with coordinates (x, y, z) extending from $x, y = 0$ to $x, y = \lambda_{x,y}$ in the horizontal directions and from $z = 0$ to $z = d$ in the vertical direction. The z-axis is chosen to point vertically downwards, parallel to the constant gravitational force, $g\hat{\boldsymbol{z}}$ (refer to Figure 3.1 for an illustration).

The evolution of the desired system is governed by the induction equation (Equation 2.20), the equations of conservation of mass (Equation 2.6), momentum (Equation 2.22), and energy (Equation 2.23), in addition to the ideal gas equation of state (Equation 2.14). Properties such as temperature, density, and pressure within the Sun depend on other interrelated transport properties of the medium. These include the thermal conductivity, viscosity and magnetic

diffusivity (Burnell, 2004). The challenge to solar physicists is to provide an accurate relationship between the various properties. This issue is addressed in more detail in Chapter 5. However, by adapting simplifying assumptions, it is possible to draw some qualitative information about the underlying dynamics.

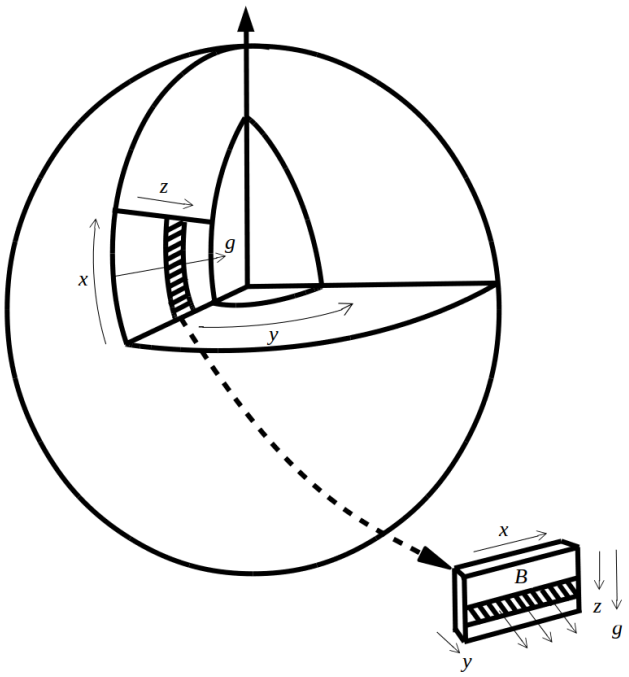

Figure 3.1: A schematic representation of the three-dimensional Cartesian plane considered for the model.

3.2.1 The Equations

To reduce the complexity of the system, it is convenient to cast the equations into dimensionless form by eliminating the measurement units. The depth of the domain, d, and the sound-crossing time, $t = d/\sqrt{R_* T_0}$, are chosen as the fundamental units of length and time, respectively, where T_0 corresponds to the temperature at the top boundary and is the unit of temperature. In a similar vein, ρ_0 is the unit of density and is scaled by the initial value at the top boundary. Furthermore, the magnetic field is assumed to be initially uniform and is scaled by the magnitude of the undisturbed strength B_0.

Suppose the dynamic viscosity, μ, magnetic diffusivity, η, thermal conductivity, K, and specific heats at constant density and pressure, c_v and c_p respectively, all constant, then the set of non-dimensional equations read:

$$\frac{\partial \rho}{\partial t} + \nabla \cdot (\rho \boldsymbol{u}) = 0, \tag{3.1}$$

$$\rho\left(\frac{\partial \boldsymbol{u}}{\partial t} + (\boldsymbol{u}\cdot\nabla)\boldsymbol{u}\right) = -\nabla p - \nabla\left(\frac{F|\boldsymbol{B}|^2}{2}\right) + F(\boldsymbol{B}\cdot\nabla)\boldsymbol{B} + \sigma C_k(\nabla\cdot\boldsymbol{\tau}) + \rho g\hat{\boldsymbol{z}}, \tag{3.2}$$

$$\frac{\rho}{(\gamma_s - 1)}\left(\frac{\partial T}{\partial t} + (\boldsymbol{u}\cdot\nabla)T\right) = -p\nabla\cdot\boldsymbol{u} + \frac{\gamma_s C_k}{(\gamma_s-1)}\nabla^2 T + C_k\left(F\zeta_0|\nabla\times\boldsymbol{B}|^2 + \frac{\sigma\tau^2}{2}\right), \tag{3.3}$$

$$\frac{\partial \boldsymbol{B}}{\partial t} = \nabla\times(\boldsymbol{u}\times\boldsymbol{B} - C_k\zeta_0\nabla\times\boldsymbol{B}), \tag{3.4}$$

$$\nabla\cdot\boldsymbol{B} = 0, \tag{3.5}$$

$$p = \rho T. \tag{3.6}$$

Consequently, a number of non-dimensional quantities parameterise the problem. These are: the Prandtl number $\sigma = \mu c_p/K$, the dimensionless thermal diffusivity $C_k = K/\rho_0 c_p d\sqrt{R_* T_0}$, the ratio of magnetic to thermal diffusivity at the top of the domain $\zeta_0 = \eta c_p \rho_0/K$, the temperature gradient $\theta = \Delta d/T$, the polytropic index $m = gd/R_*\Delta T - 1$, and lastly the dimensionless field strength $F = {B_0}^2/R_* T_0 \rho_0 \mu_0$.

3.2.2 Boundary and Initial Conditions

To close the system of equations, certain boundary conditions are prescribed. In the horizontal directions, the system is assumed to satisfy periodic boundary conditions. The imposed boundary conditions at the top and bottom of the domain ($z = 0$ and $z = d$, respectively) are such that the system is impermeable, stress-free, and the magnetic field is vertical, i.e. the mass flux and mechanical energy flux vanishes at the boundaries. Temperature is fixed at

the upper surface, whilst heat flux is assumed to be a constant at the lower surface, which means that the imposed heat flux is the only flux of energy into and out of the system. These conditions are summarised by

$$\begin{aligned} u_z = \frac{\partial u_x}{\partial z} = \frac{\partial u_y}{\partial z} = B_x = B_y = 0, \quad T = T_0 \text{ at } z = 0, \\ u_z = \frac{\partial u_x}{\partial z} = \frac{\partial u_y}{\partial z} = B_x = B_y = 0, \quad \frac{\partial T}{\partial z} = \frac{T_0 \theta}{d} \text{ at } z = d. \end{aligned} \tag{3.7}$$

The governing equations exhibit an equilibrium solution describing a stratified polytropic atmosphere in hydrostatic balance. Thus, the initial configuration for temperature and density distributions take the form

$$T = T_0(1 + \theta z/d), \quad \rho = \rho_0(1 + \theta z/d)^m, \tag{3.8}$$

where m is the polytropic index introduced earlier. All simulations start from this initial state together with small amplitude perturbations of the temperature profile. The early stages of evolution exhibit sensitivity to the initial conditions prescribed, however the specific details of the initial perturbation do not greatly influence the long-term evolution of the system. Examples of different initial temperature and density profiles are displayed in Figure 3.2.

3.2.3 Magnetic Pumping Profiles

As in Barker *et al.* (2012), the model has been modified to incorporate the γ-effect, derived in Subsection 2.4.3, via an additional term $\nabla \times (\boldsymbol{\gamma} \times \boldsymbol{B})$ in the induction equation (Equation 3.4). It is worth emphasising that this modulation of pumping only captures the effect of small-scale turbulence on the evolution of the large-scale magnetic field. Although this mathematical approach does not consider the scales of convection which are comparable or larger than the buoyancy modes, it is to provide an understanding of the underlying physical interactions that influence buoyant magnetic structures.

Given that the computational box in the Cartesian space has periodic bound-

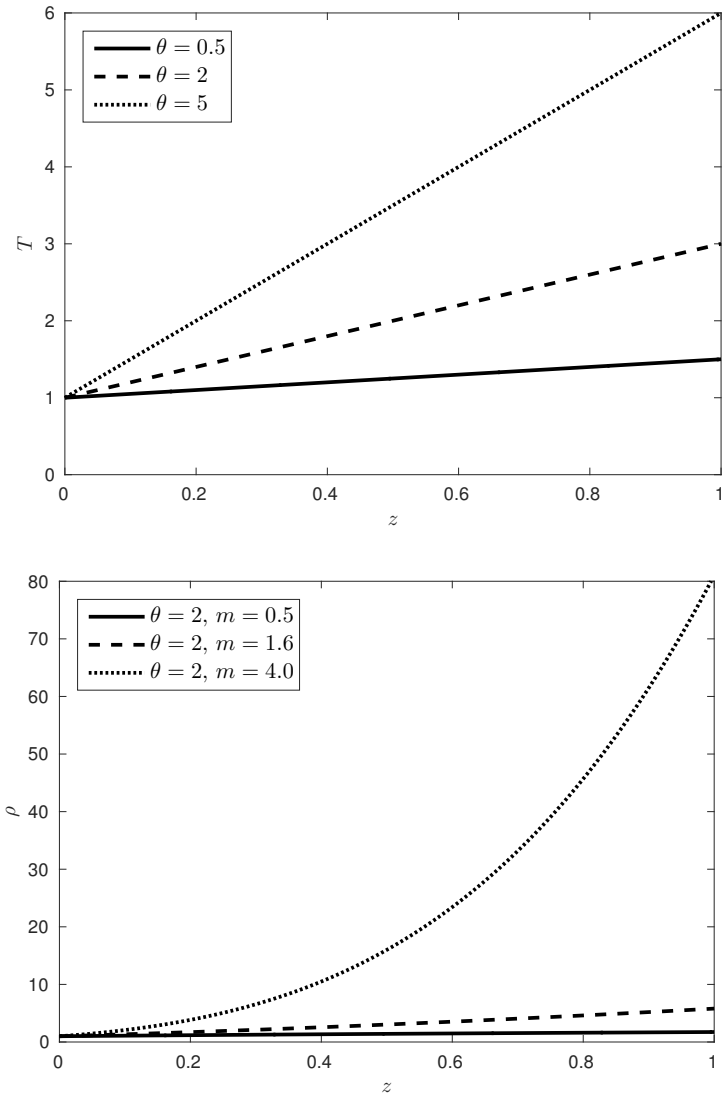

Figure 3.2: Plots of the initial temperature distribution (top panel) and density distribution (bottom panel) for several values of θ and m, where $d = T_0 = \rho_0 = 1$.

ary conditions imposed in the horizontal directions, it is appropriate to express the mean quantities as horizontal averages. Convection cells with relatively small spatial scale, comparable with the horizontal length scales of the box, are considered. Therefore, an average of these small-scale convection cells can be defined. In these simulations, the magnetic field $\boldsymbol{B}$ is introduced as a mean field, with scales being larger than the artificial convection.

The initial vertical profile of magnetic pumping described by Barker *et al.* (2012) had the following form:

$$\boldsymbol{\gamma} = \gamma(z)\hat{\boldsymbol{z}} = \frac{\gamma_m}{2}\left[1 + \tanh\left((\Delta z_B)^{-1}(z_B - z)\right)\right]\hat{\boldsymbol{z}}, \tag{3.9}$$

where γ_m is the magnetic pumping strength, z_B is the bottom of the pumping layer, and $(\Delta z_B)^{-1}$ is the width of transition layer.

This spatial dependency of the pumping was selected to represent the change that occurs between the radiative and convection zones with the pumping gradually decaying to zero at the interface of the two zones. However, such pumping profile does not convey the full picture of the dynamics of magnetic field in the presence of turbulent convection. The chosen profile can be interpreted as a solid wall acting upon the magnetic field, i.e. there is no variability in the mean downward force overlying the magnetic layer.

Unlike in Barker *et al.* (2012), $\boldsymbol{\gamma}$ will be time-dependent as its derivation incorporates spatial but not temporal averaging. The form of the γ-pumping is formally discussed in, for example, Moffatt (1983), where it is shown that the vector $\boldsymbol{\gamma}$ can be time-dependent in a similar way that the α-effect can be time variant (see Hughes *et al.*, 2011). In this work, the time-dependent, vertical γ-pumping profile is chosen to have the following form:

$$\boldsymbol{\gamma} = \gamma(z,t)\hat{\boldsymbol{z}} = \frac{\gamma_m}{2}\left[1 + \sin(kt)\right]\left[1 + \tanh\left((\Delta z_B)^{-1}(z_B - z)\right)\right]\hat{\boldsymbol{z}}\,, \tag{3.10}$$

where k controls the variation of the pumping in time, and where γ is always greater than, or equal to, zero. As this is the first inclusion of a time-dependent γ-pumping in such a model, the motivation was to first mathematically understand the effect of time-dependence on the γ-pumping. Therefore, the time-dependent nature of the pumping has been chosen to behave in a simple oscillatory pattern to ease our understanding of the dynamics in a controlled, and well-defined, framework. Figure 3.3 illustrates an example of how the γ-pumping varies throughout space and time in this model.

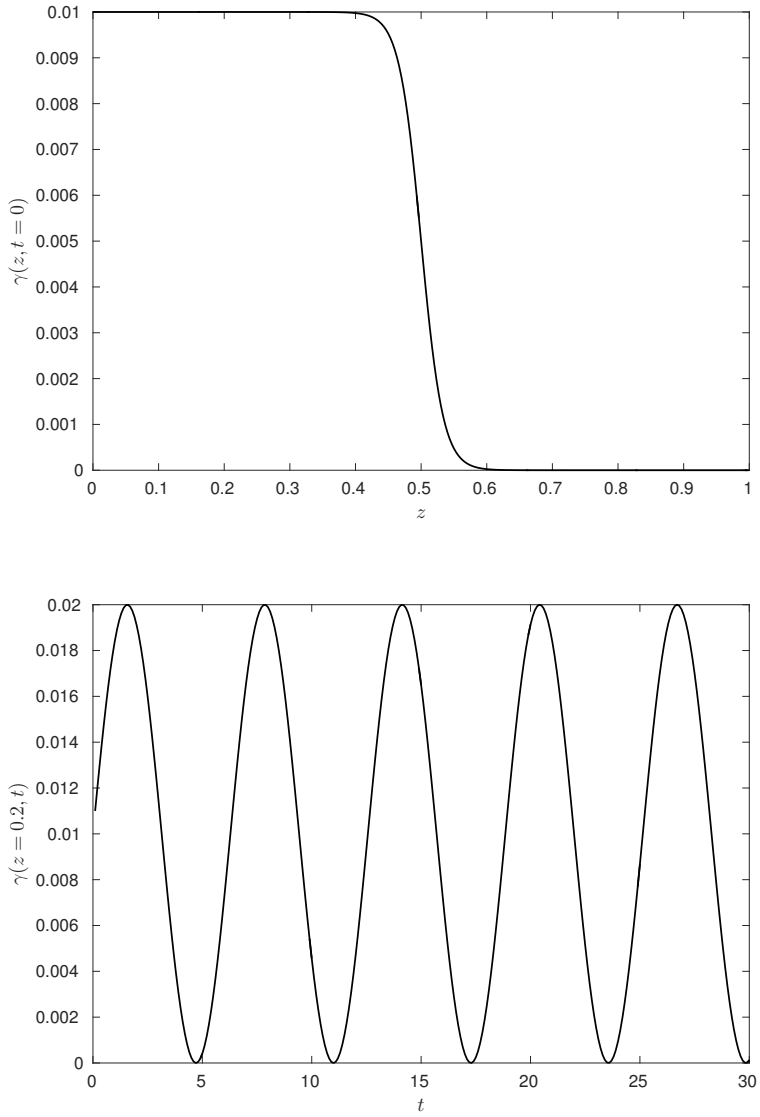

Figure 3.3: A pumping profile, $\gamma(z,t)$ with $k = 1$, $\gamma_m = 0.01$, $z_B = 0.5$, and $(\Delta z_B)^{-1} = 30$, as function of depth at time $t = 0$ (top panel) and time at depth $z = 0.2$ (bottom panel).

3.2.4 Parameter Choices

The dynamical evolution of a uniform, horizontal magnetic layer $\boldsymbol{B} = B_y\hat{\boldsymbol{y}}$, positioned in the region bounded by $z = z_1$ and $z = z_2$ and is zero everywhere, is evaluated under the influence of magnetic flux pumping. To accommodate the imposed magnetic field, upon the existing hydrodynamic state, the density in the magnetic layer is adjusted, so the system is in equilibrium. Table 3.1 displays the parameter choices for this model. These are chosen exactly as in Barker *et al.* (2012) to allow direct comparison with the results of the current investigation when a time-dependent pumping profile is included.

Parameter	Description	Value
σ	Prandtl number	0.005
C_k	Thermal diffusivity	0.01
θ	Thermal stratification	2.0
γ_s	Ratio of specific heats	5/3
ζ_0	Magnetic diffusivity	0.01
F	Magnetic field strength	0.01
m	Polytropic Index	1.6
γ_m	Magnetic pumping strength	0.1
z_B	Bottom of pumping layer	0.5
$(\Delta z_B)^{-1}$	Width of transition layer	30.0
z_1, z_2	Top and bottom of magnetic layer	0.6, 0.8
λ_x, λ_y	Box horizontal aspect ratio	1.0, 4.0
d	Vertical depth of box	1.0
$B_y(t=0)$	Initial horizontal magnetic strength	1.0
k	Frequency associated with magnetic pumping	Variable

Table 3.1: The choice of parameters for the γ-pumping model.

The choice of parameters represents a sub-adiabatic, stratified layer achieved by setting $\gamma_s = 5/3$ and $m = 1.6$, which is noted to be less appropriate for the region straddling the boundary of the convection zone. However, the results in Barker *et al.* (2012) did not differ significantly from considering a piece-wise polytropic layer. The strength of the magnetic pumping is constrained to $\gamma_m < 0.5$ in order to mimic the magnetic effects resulting from compressible turbulent convection (see Tobias *et al.*, 2001). While the chosen values of thermal diffusivity, viscosity, and magnetic diffusivity are less extreme than in the

Sun, the same order as associated with the solar interior, i.e. $1 \gg \zeta_0 \gg \sigma$ and $C_k \ll 1$, is maintained (Gough, 2007). Magnetic field strength is restricted to $F \ll 1$ on adopting the plasma beta present in the tachocline, $\beta \sim 10^7$, which is the ratio of magnetic and gas pressures (Tobias and Hughes, 2004). The only variable quantity in the present simulations is k. Here, three cases are discussed: Case 1 where $k = 1$, Case 2 where $k = 0.1$, and Case 3 where $k = 0.01$.

Pumping effect on scalar fields of density and temperature, arising from turbulence, are ignored as they are not directly related to the magnetic pumping velocity. Also, the computational domain is elongated in parallel to the imposed discontinuous field to allow vortex-induced instabilities and three-dimensional structures to form (Matthews *et al.*, 1995a). Non-zero diffusion coefficients are incorporated into the system by explicitly defining the diffusive length scales to be considerably more significant than the scale of the unresolved convection. As in Barker *et al.* (2012), these diffusivities should be considered as eddy diffusivities due to the unresolved small-scales of convection, which is consistent with the spirit of the mean-field framework.

3.2.5 Numerical Scheme

The complex non-linear interactions and the broad range of spatial and temporal scales that occur in astrophysical systems pose significant challenges in solving the MHD equations, by which all scales of motion are fully resolved. To date, several numerical techniques have been devised to solve the full set of coupled equations with acceptable accuracy. The direct numerical simulation (DNS) is the most exact method as the full, time-dependent set of equations are solved numerically, and so it directly captures all scales contained in the field. However, it is the most expensive approach due to the huge computational resources required. Current resources are insufficient to span all relevant scales of turbulence down to the diffusion scale, for instance.

With the desire of predicting accurate dynamic properties of turbulent flows, the local approach of solving the MHD equations is employed using the DNS scheme in a Cartesian framework. A modified version of a mixed finite-difference/pseudo-spectral code is used, where detail on the original numerical set-up can be found in Matthews *et al.* (1995b). Time discretisation is carried out based on an explicit, third-order Adams-Bashforth scheme, whilst spatial discretisation is performed using fourth-order finite-difference in the vertical direction (upwind derivatives being utilised for the advection terms), and fast Fourier transforms in the horizontal direction.

Spatial-discretisation

To approximate gradients in the vertical direction, an explicit fourth-order finite difference method is applied to the conservative form of the governing equations. The concept of a finite-difference scheme follows from invoking the definitions of a derivative, and Taylor series expansion. For a differentiable function f, the derivative with respect to x is expressed by the limit

$$\frac{df}{dx} = \lim_{\Delta x \to 0} \frac{f(x+\Delta x) - f(x)}{\Delta x}, \tag{3.11}$$

and using Taylor's theorem, the function f can be expanded as a Taylor series around x,

$$\begin{aligned} f(x+\Delta x) =& f(x) + \Delta x \frac{df(x)}{dx} + \frac{\Delta x^2}{2}\frac{d^2 f(x)}{dx^2} + \frac{\Delta x^3}{3!}\frac{d^3 f(x)}{dx^3} + ... \\ &+ \frac{\Delta x^{n-1}}{(n-1)!}\frac{d^{n-1} f(x)}{dx^{n-1}} + \mathcal{O}(\Delta x^n). \end{aligned} \tag{3.12}$$

By assuming that the grid spacing is uniform and rearranging the Taylor series, the first derivative of f at grid point i reads as follows:

$$f_i^{(1)} = \left.\frac{df}{dx}\right|_i = \frac{f_{i+1} - f_i}{\Delta x} - \frac{\Delta x}{2} f_i^{(2)} - \mathcal{O}(\Delta x^2) \tag{3.13}$$

$$f_i^{(1)} \approx \frac{f_{i+1} - f_i}{\Delta x}, \tag{3.14}$$

where subscript $i+1$ denotes the mesh point $i+1$. The last two terms on the right-hand side of Equation (3.13) refer to the error committed by truncating the series and is known as the truncation error. The accuracy of the approximation relies on terminating the expansion and considering the truncation error at higher orders. Equation (3.14) is called the first-order forward difference formula. Similarly, expressions for the backward and central differences can be determined by calculating $f_i - f_{i-1}$ and $f_{i+1} - f_{i-1}$ respectively. For the central difference scheme, that is

$$\frac{f_{i+1} - f_{i-1}}{2\Delta x} = f_i^{(1)} + \frac{\Delta x^2}{3!} f_i^{(3)} + \frac{\Delta x^4}{5!} f_i^{(5)} + \mathcal{O}(\Delta x^6). \tag{3.15}$$

Thus to obtain the second-order central difference approximation, terms of order $\mathcal{O}(\Delta x^2)$ and higher are eliminated. For fourth-order approximation, it is essential to include additional neighbouring points. Using Taylor series expansion, one can derive an expression for $f_{i+2} - f_{i-2}$ and eliminate the second order error term to get

$$\frac{8(f_{i+1} - f_{i-1}) - (f_{i+2} - f_{i-2})}{12\Delta x} = f_i^{(1)} - \mathcal{O}(\Delta x^4). \tag{3.16}$$

This fourth-order central difference scheme is employed on all interiors points, while the backward or forward schemes can be utilised at the boundaries.

The periodicity in the horizontal directions of the domain encourages the pseudo-spectral approach of computing the derivatives using fast Fourier transforms, such that a spectral domain is used merely to obtain approximations of the spatial derivatives at the grid points. This consequently leads to better accuracy, with respect to the resolution, relative to the standard finite-difference schemes (Fox and Orszag, 1973; Durran, 2013).

To illustrate the pseudo-spectral approach, suppose the periodic function $f(x)$ with period L discretised for N values by taking samples at the frequencies nL/N such that $f_n = f(nL/N)$, where $n = 0, 1, ..., N-1$. Expressing f_n in

the following form:

$$f_n = \sum_{k=0}^{N-1} F_k e^{\frac{2\pi i}{N} nk}, \tag{3.17}$$

the Fourier coefficients F_k are determined using the discrete Fourier transform (DFT) (Johnson, 2011)

$$F_k = \frac{1}{N} \sum_{n=0}^{N-1} f_n e^{\frac{-2\pi i}{N} nk}. \tag{3.18}$$

Therefore, applying the differential operator $\mathrm{d}/\mathrm{d}x$ simply involves pointwise multiplication of each F_k term in the k-space. The direct computation of the DFT would involve $\mathcal{O}(N^2)$ operations, while by adapting the algorithm of fast Fourier transform (FFT), this is reduced to $\mathcal{O}(N \log N)$ (Nussbaumer, 2013). Thus, providing an effective way of computing the transition between spatial and Fourier domains and a rapid means of calculating the derivatives. A complete review of FFT can be found in Manolakis and Ingle (2011) and Ryan (2019).

It is important to note, however, that one would deduce the exact samples f_n for terms $F_k e^{\frac{2\pi i}{N} nk}$ and $F_k e^{\frac{2\pi i}{N} n(k+mN)}$, given that $e^{2\pi inm} = 1$ for any integers n and m. This sample reconstruction, based on wrong frequencies, is known as aliasing. The re-sampling of f_n is unaffected, but the additional m-oscillations between the sample points return significant changes on the derivatives. Several methods do exist to eliminate the aliasing error (see Canuto *et al.*, 2006), which includes setting a bandlimit to frequencies $|k + m_k N| \leq N/2$ or alternatively minimising the first derivative of the interpolated $f(x)$. The latter approach of minimising the mean-square slope (see Johnson 2011 for a complete derivation) yields minima for $m_k = 0$ if $0 \leq k < N/2$ and for $m_k = -1$ if $N/2 < k < N$. However, solutions are not unique for the $k = N/2$ component, for even N. Following from Johnson (2011), the unique trigonometric

interpolation of the form

$$f(x) = F_0 + \sum_{0<k<N/2} \left(F_k e^{\frac{2\pi i}{L}kx} + F_{N-k} e^{-\frac{2\pi i}{L}kx} \right) + F_{N/2} \cos\left(\frac{\pi}{L} N x\right) \quad (3.19)$$

provides the minimal oscillation between the sample points.

The approach considered in this work to control the aliasing error and ensure calculations of more spectral accuracy, is to place a cut-off at one-third of the possible frequencies $(N/2)/3$.

Time-discretisation

To advance a system in time, several numerical time-stepping treatments exist that can be classified as explicit or implicit. Both types of procedures have advantages and disadvantages, depending on the nature of the problem. In explicit schemes, solutions are determined at each time-step based on the solution at the current and previous time-steps. Therefore, explicit methods are simple, as solutions can be directly calculated at each point; however, appropriate small time-steps must be selected to capture the correct physical behaviour and circumvent numerical instabilities (Wriggers, 2008). In implicit schemes, conversely, solutions are determined at each time-step based on the solution at the current and approximate future time-steps. Implicit methods are not limited by time-step size and so can converge to the same solution more efficiently, in comparison to explicit methods. However, to approximate future time-steps, implicit schemes would require additional computational efforts (Wriggers, 2008).

Besides the general classification of implicit and explicit schemes, time-discretisation methods can also be identified as single-step or multi-step. One-step methods include the Euler method, and the multi-stage Runge-Kutta method, where only the solution of the previous state is required to compute the future state (Grasselli and Pelinovsky, 2008). The Adam-Bashford method and

the Leapfrog method are examples of multi-step methods, where several previous state solutions are considered to calculate the future state (LeVeque, 2007).

To allow the solutions of the governing MHD equations evolve in time, an explicit Adams-Bashforth method of third-order is employed. The timescale for diffusion and wave propagation through a mesh interval can become a source of numerical instability, and thus impose limitations on the length of the computational time-step. Additionally, such time-steps must be continuously checked and modified during run-time, thus making it appropriate to adopt this multi-step approach. In Matthew *et al.* (1995b), both for diffusion and wave propagation the time-step limits were found to be of the same order of magnitude.

The Euler method can be interpreted as the basis to all numerical methods. Thus, prior to illustrating the third-order Adams-Bashforth scheme, consider the initial value problem (Süli and Mayers, 2003):

$$f(t_0, x) = f_0(x), \qquad \frac{\partial f(t,x)}{\partial t}\Big|_{t=t_0} = f_0^{(1)}(x). \tag{3.20}$$

The solution of $f(t, x)$ at time $t = t_0 + h$, where h is the step size, can be computed using the following forward Euler formula

$$f(t_0 + h, x) = f(t_0, x) + h f_0^{(1)}(x). \tag{3.21}$$

The first iteration in the Adams-Bashforth scheme is determined using Equation (3.21) and is also known as the first-order Adams-Bashforth. This is followed by the second-order Adams-Bashforth in which the preceding time-derivative is adapted to evaluate the next iteration

$$f_{n+1} = f_n + \alpha_0 f_n^{(1)} + \alpha_1 f_{n-1}^{(1)}, \tag{3.22}$$

where subscript n denotes the present time-step, and the weights α_0 and α_1 are to be found. This scheme is based on the idea of approximating the derivative $f^{(1)}$ with a polynomial on the interval $[t_n, t_{n+1}]$ via integration, where a p-order polynomial results in a $(p+1)$-order method.

For the second-order Adams-Bashforth, the polynomial takes the form $P(t) = At + B$, where the coefficients of the polynomial are determined using the previously calculated points, n and $n-1$. That is, the equations

$$At_n + B = f_n^{(1)}, \qquad At_{n-1} + B = f_{n-1}^{(1)}, \tag{3.23}$$

are solved to give the polynomial coefficients

$$A = \frac{f_n^{(1)} - f_{n-1}^{(1)}}{h_0}, \qquad B = \frac{t_n f_{n-1}^{(1)} - t_{n-1} f_n^{(1)}}{h_0}, \tag{3.24}$$

where $h_0 = t_n - t_{n-1}$. Integrating the polynomial P within the interval $[t_n, t_{n+1}]$, where non-uniform step size is assumed gives

$$\begin{aligned} f_{n+1} =& f_n + \frac{A}{2}(t_{n+1}^2 - t_n^2) + B(t_{n+1} - t_n) \\ =& f_n + f_n^{(1)}\left(\frac{(t_{n+1}^2 - t_n^2)}{2h_0} - \frac{h_1 t_{n-1}}{h_0}\right) - f_{n-1}^{(1)}\left(\frac{(t_{n+1}^2 - t_n^2)}{2h_0} - \frac{h_1 t_n}{h_0}\right) \\ =& f_n + f_n^{(1)}\left(h_1 + \frac{h_1^2}{2h_0}\right) - \frac{h_1^2}{2h_0} f_{n-1}^{(1)}, \end{aligned} \tag{3.25}$$

where $h_1 = t_{n+1} - t_n$. The weights for the second-order Adams-Bashforth (Equation 3.22) are therefore given by

$$\alpha_0 = h_1\left(1 + \frac{h_1}{2h_0}\right), \qquad \alpha_1 = \frac{h_1^2}{2h_0}. \tag{3.26}$$

Similarly, the second-order method can be expanded for third-order or higher. The third-order Adams-Bashforth scheme would require knowledge of two previously computed solution values

$$f_{n+1} = f_n + \alpha_0 f_n^{(1)} + \alpha_1 f_{n-1}^{(1)} + \alpha_2 f_{n-2}^{(1)}, \tag{3.27}$$

with weights

$$\begin{aligned}
\alpha_0 &= h_1 + \frac{h_1^2(h_0+h_2)}{2h_0h_2} + \frac{h_1}{3h_0h_2}, \\
\alpha_1 &= \frac{h_1^2h_2}{2h_0(h_0-h_2)} + \frac{h_1^3}{3h_0(h_0-h_2)}, \\
\alpha_2 &= -\frac{h_1^2h_0}{2h_2(h_0-h_2)} - \frac{h_1^3}{3h_2(h_0-h_2)},
\end{aligned} \tag{3.28}$$

where $h_2 = t_n - t_{n-2}$.

When implementing the numerical algorithm discussed above to solve the desired system, the choice of stress-free boundaries may raise an issue relating to the momentum conservation, as reported by Jones *et al.* (2011). The conservation form of the mass, momentum, and magnetic field equations are considered in order to ensure that the mass, momentum, and the divergence of the magnetic field are well conserved as the simulation proceeds. However, numerical errors, including round-off and truncation errors during each time-step, tend to add a small change in momentum. As the time-step magnitude increases, these small changes can produce non-physical solutions. The solutions reported in this thesis are carefully checked, where mass and momentum remain conserved.

3.3 Results (Nonlinear Breakup)

This section is devoted to a discussion of the non-linear breakup of a uniform, artificially imposed, horizontal magnetic layer, in the presence of a time-dependent magnetic flux pumping at the upper fraction of the domain, using the numerical model detailed in Section 3.2. In the absence of the γ-pumping, the physics underlying this configuration has been elucidated in a series of numerical experiments carried out by Cattaneo and Hughes (1988) and Matthews *et al.* (1995a). The here presented results are an extension of work previously performed by Barker *et al.* (2012) on the emergence of magnetised structures at the base of the convection zone.

The effects of a time-dependent γ-pumping are explored by considering a selection of different pumping timescales. In Case 1, the pumping profile is as given in Equation (3.10) where $k = 1$, such that the γ-pumping evolves in line with the sound-crossing time. Snapshots of the magnetic field for this regime (Case 1) are shown in Figure 3.4. The system initiates with the uniform magnetic layer embedded in the lower part of the domain (Figure 3.4(a)). As time evolves, a Rayleigh-Taylor type instability occurs as a result of the dense medium supported by the less dense magnetised layer under gravity, leading to the formation of buoyancy-driven magnetic structures ascending towards the pumping region (Figure 3.4(b)). Once the magnetic field reaches the base of the γ-pumping region, z_B, magnetic flux concentrations begin to intensify.

The enhancement of the magnetic field strength is influenced by several factors. These include the vertical variation in the downward pumping which can contribute to field amplification according to the induction equation, the competing effect of magnetic buoyancy and γ-pumping below the interface, and the complex interaction due to the magnetic field generating vortices. Locally ascending magnetic structures and descending fluid are known to cause the onset of Kelvin-Helmholtz instability, giving rise to three-dimensional arching of the magnetic field (Matthews *et al.*, 1995a; Fan, 2001), as seen in Figure 3.4(c).

Emerging magnetic flux tubes continue to ascend in Figure 3.4(d) but are soon pushed back down in Figure 3.4(e). This is in contrast with the earlier findings of Barker *et al.* (2012), where concentrated magnetic structures were seen to rise continually once the magnetic field reaches the equipartition value determined by the Alfvénic Mach number for the γ-pumping at the interface,

$$M_\gamma \;=\; (B_y(t))^{-1}\gamma_m\sqrt{\rho(z_B)/F}\,. \tag{3.29}$$

In this model, the Alfvénic Mach number must be modified to allow for tem-

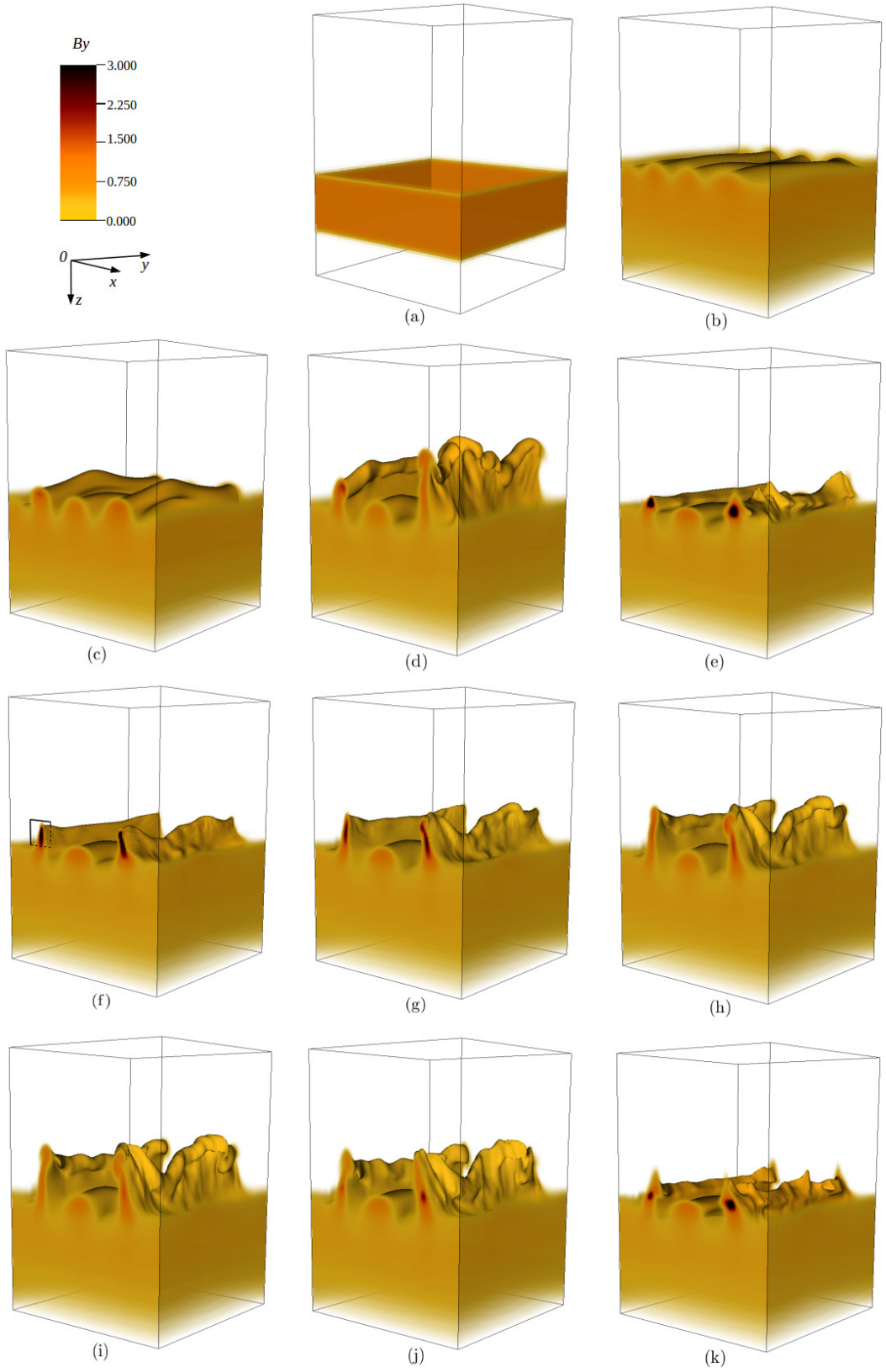

Figure 3.4: Snapshots of the y-component of the magnetic field for Case 1 at (a) $t = 0.69$, (b) $t = 156.8$, (c) $t = 188.5$, (d) $t = 206.5$, (e) $t = 208.6$, (f) $t = 210.8$, (g) $t = 211.5$, (h) $t = 212.2$, (i) $t = 212.9$, (j) $t = 213.6$, and (k) $t = 214.4$ respectively.

poral and spatial variations. That is, to take into account the time-dependent nature of the γ-pumping and to determine the action of the magnetic field across various depths, i.e.

$$M_\gamma \;=\; (B_y(t))^{-1}\gamma(z,t)\sqrt{\rho(z)/F} \;=\; (B_y(t))^{-1}B_{eq}(z,t)\,, \tag{3.30}$$

where B_{eq} denotes the equipartition value of the mean magnetic field with the γ-pumping.

To study the behaviour of emerging magnetic flux in more detail, the horizontal magnetic component of the field in the y-direction is examined, as a function of time and depth. Magnetic components in the x- and z-directions are of least interest and remain significantly small throughout all calculations. Figure 3.5 provides an example of the changes that are occurring to the magnetic field in relation to the strength of the γ-pumping by focusing on an individual magnetic structure (see the box in Figure 3.4(f) for a visualisation of the region of interest) at the particular point $x = 0.25$ and $y = 0$. To allow a clearer physical interpretation of the results, the difference $B_{eq} - B_y$ (plotted in Figure 3.5) is introduced. Positive values of $B_{eq} - B_y$ represent changes in the magnetic field and/or the magnetic flux pumping such that the γ-pumping counteracts the upward transport of the magnetic field, i.e. $M_\gamma \gtrsim 1$.

From Figure 3.5(a) it can be seen that at the near-interface region, z_B, the intense magnetic structure begins to escape the lower layer where $B_{eq} - B_y < 0$. The extent to how far the structure can traverse depends on whether an equipartition-strength mean magnetic field is attained. This magnetic structure continues to rise to the upper layer in Figures 3.5(b) and 3.5(c), while the field generally decreases in magnitude. Eventually, further through the upper domain, the magnetic strength, B_y, becomes insufficient to overcome the threshold equipartition value, and hence transitioning to the $B_{eq} - B_y > 0$ regime, where the pumping is able to hold back the magnetic field from rising.

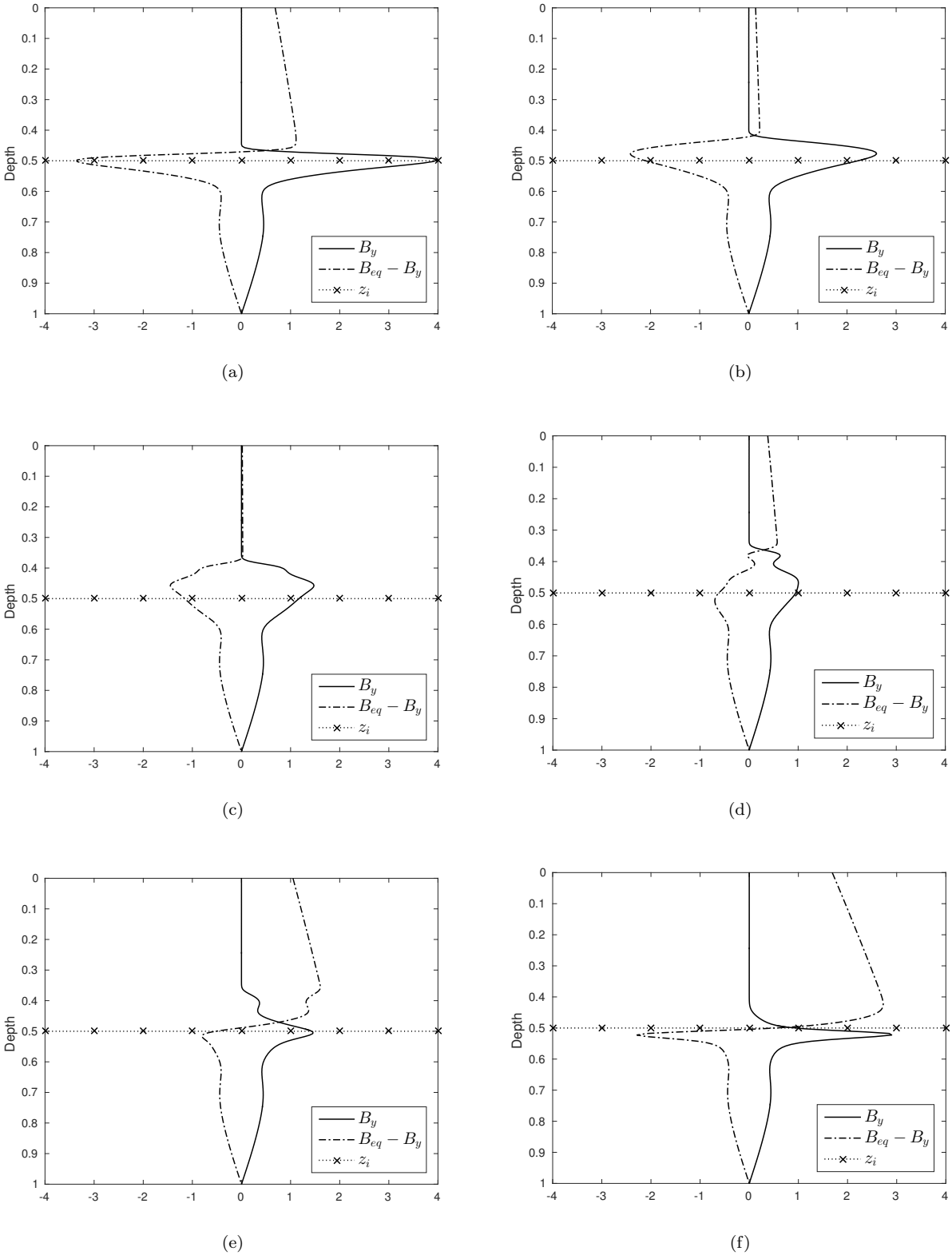

Figure 3.5: The horizontal magnetic field B_y and the difference $B_{eq} - B_y$ vs. depth for a magnetic structure in Case 1, located at $x = 0.25$ and $y = 0$, at times (a) $t = 210.8$, (b) $t = 211.5$, (c) $t = 212.2$, (d) $t = 212.9$, (e) $t = 213.6$, and (f) $t = 214.4$.

Given the temporal variation of the γ-pumping in Case 1, the magnitude of the pumping and hence the equipartition value begin to increase in Figure 3.5(d). This can be traced by the difference $B_{eq} - B_y$ at the upper part of the domain, i.e. $z < 0.2$, where $B_y \approx 0$. Emerging magnetic structures experience the maximum downward force at the upmost depth achieved, due to the nature of the pumping profile. Hence, the intensification of the magnetic field, B_y, observed just above $z \approx 0.4$, in addition to the magnetic field being pushed downwards. This behaviour persists with the growth of the equipartition value, as a result of the increase in the pumping strength, in Figure 3.5(e). Finally, Figure 3.5(f) shows that the γ-pumping achieves sufficient strength to push and maintain the magnetic field below $z \approx 0.5$, in addition to the amplification of the magnetic field.

In Case 1, magnetic structures are observed to be continuously pushed down and repelled back up due to the temporal variation of the magnetic pumping. Further, a dependency on the Alfvénic Mach number M_γ that controls the rise of localised magnetic structures is established. The magnetic field is found to be held down, with intense concentrations generated below the interface, in the phase where $M_\gamma \gtrsim 1$, i.e. $B_{eq} - B_y > 0$. Transitioning to $M_\gamma \lesssim 1$, these magnetic concentrations become sufficiently stronger than the present equipartition threshold. Thus, ascending to the upper domain until the periodic pumping cycle reaches high levels of strength, returning background magnetic field to the lower domain. The γ-pumping, occupying the region above z_B, acts as a filter allowing magnetic structures to emerge into the upper domain once the desired strength is achieved while sustaining the magnetic field at the lower domain. Nonetheless, variations in the pumping timescale play an important role in the emergence of magnetic structures.

To explore the relationship that exists between the time-dependent γ-pumping and emerging magnetic structures in greater detail, the frequency of the pump-

ing cycle is scaled down by setting $k = 0.1$. In this case (Case 2), the spreading of the initial magnetic field is found consistent with Case 1. However, the contribution of different pumping timescales becomes evident once the magnetic field has diffused and reached the pumping zone. To elaborate, Figure 3.6 follows the evolution of a magnetic structure in Case 2, located at $x = 0.25$ and $y = 0$ for a period of time, similar to that in Figure 3.5.

As opposed to Case 1, Figures 3.6(a) and 3.6(b) show that the rise of the magnetic structure, through the γ-pumping region, is delayed to a later stage. This arises from the magnetic pumping strength, γ_m, varying at a slower rate in Case 2. Accordingly, the interactions between the γ-pumping and magnetic field occur over a longer timescale, causing the formation of stronger magnetic concentrations below $z \approx 0.5$, as shown in Figures 3.6(c)$-$3.6(f). Within the time period where an apparent magnetic emergence process in Case 1 is found, the magnetic equipartition value is always dominant in the upper domain for Case 2. Therefore, no flux emergence is observed, and so it is useful to explore the magnetic emergence across a broader time range.

Figure 3.7 demonstrates the evolution of the particular magnetic structure considered in Figure 3.6 during a complete pumping cycle. The equipartition criterion established earlier remains consistent with the emergence of magnetic flux. However, in this regime, the magnetic field is noticed to spread further throughout the pumping region. This is because, for slower temporal variation in the γ-pumping, magnetic structures are able to propagate further once emergence takes place. Moreover, at particular stages, the pumping strength decays, followed by the equipartition value. Hence, permitting buoyancy-driven magnetic structures to rise. Snapshots of the non-linear evolution of the horizontal magnetic field in Case 2 are displayed in Figure 3.8.

Evolution of the total kinetic and magnetic energies for Case 1, Case 2 and an additional Case 3, where $k = 0.01$, are shown in Figure 3.9. The kinetic and

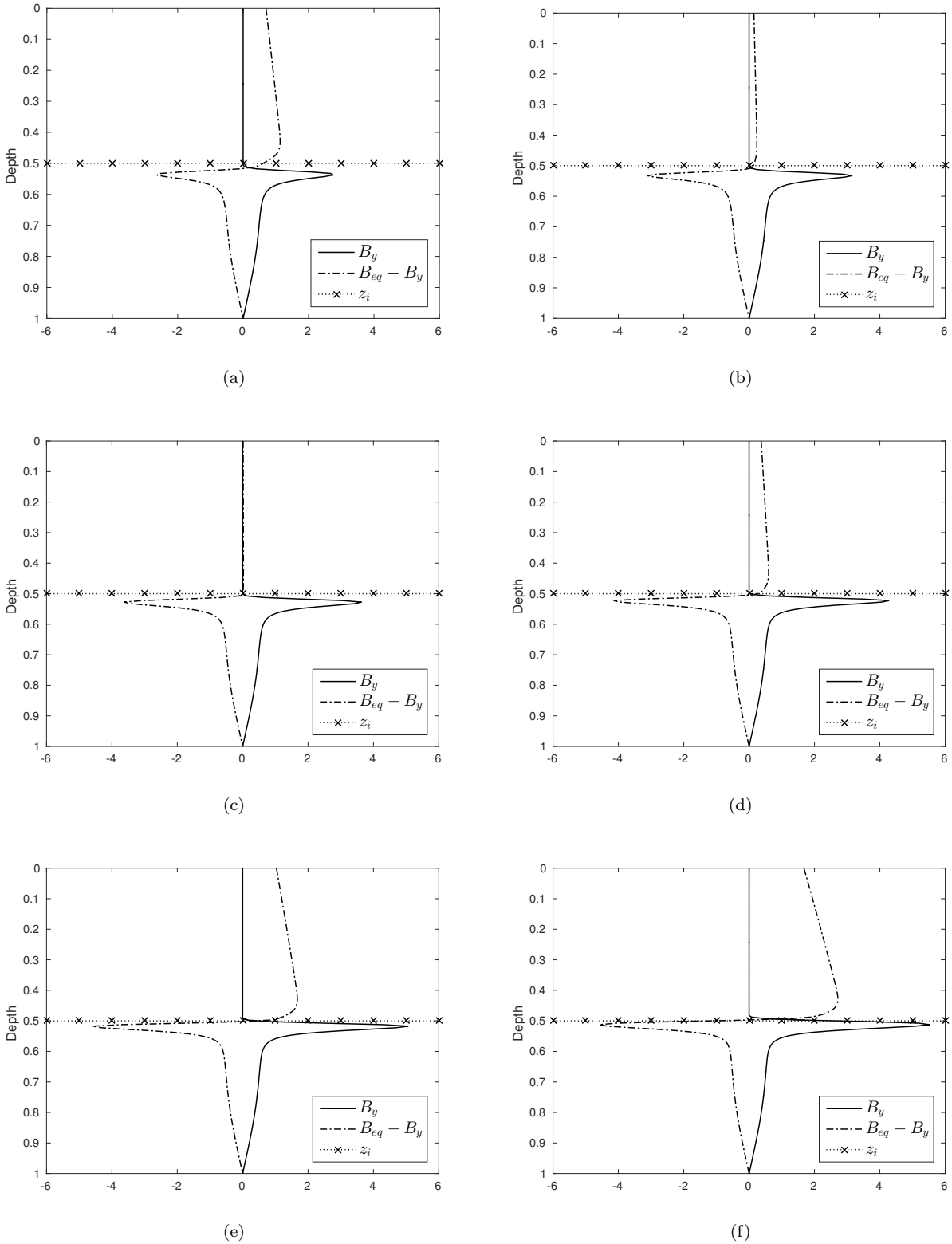

Figure 3.6: The horizontal magnetic field B_y and the difference $B_{eq} - B_y$ vs. depth for a magnetic structure in Case 2, located at $x = 0.25$ and $y = 0$, at times (a) $t = 210.8$, (b) $t = 211.5$, (c) $t = 212.2$, (d) $t = 212.9$, (e) $t = 213.6$, and (f) $t = 214.4$.

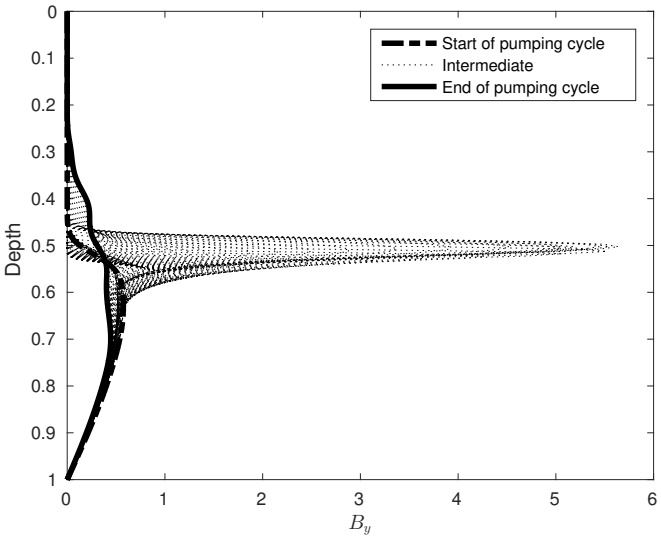

Figure 3.7: Line graphs of B_y vs. depth, for a magnetic structure in Case 2, located at $x = 0.25$ and $y = 0$, at regularly-spaced time intervals. The pumping cycle starts at $t = 171.9$ and ends at $t = 236.8$.

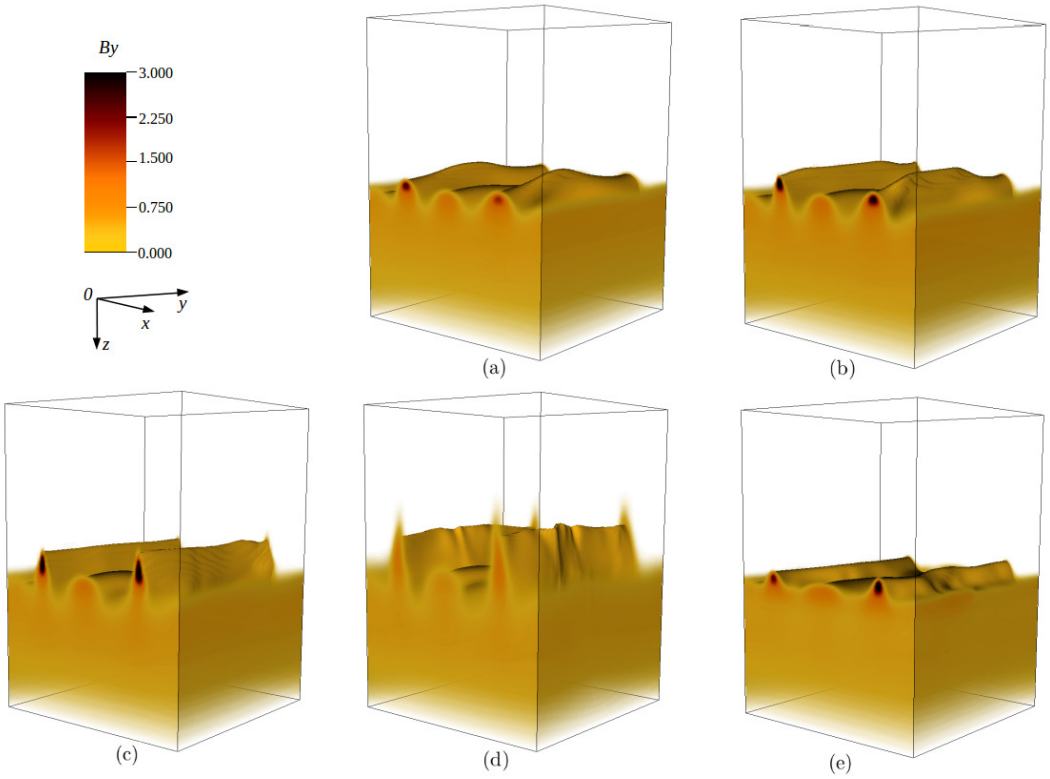

Figure 3.8: Snapshots of the y-component of the magnetic field for Case 2 at (a) $t = 210.8$, (b) $t = 214.4$, (c) $t = 222.3$, (d) $t = 233.9$, and (e) $t = 254.8$ respectively.

magnetic energies are expressed as

$$E_K = \int_V \frac{1}{2}\rho \boldsymbol{u}^2 \mathrm{d}V, \tag{3.31}$$

and

$$E_M = \int_V \frac{1}{2} F \boldsymbol{B}^2 \mathrm{d}V, \tag{3.32}$$

respectively, where the volume integral is computed over the whole domain. The growth of the kinetic and magnetic energies result from the mechanisms responsible for the enhancement of the local magnetic field. This is followed by the almost periodic release of energies, based on the characteristics of the imposed γ-profile, leading to the emergence of magnetic structures through the upper layer. For Case 1, magnetic concentrations emerge frequently, but with weaker field strengths in comparison to Case 2 and Case 3. The magnetic intensification process in Case 3 is found more effective, due to the pumping strength varying over a longer timescale, hence allowing the magnetic field to interact efficiently with the γ-pumping.

The temporal variation of the γ-pumping reveals a correlation with the action of buoyant magnetic structures. This is shown in Figure 3.10 by comparing the evolution of a γ-pumping profile with its associated magnetic energy for Case 1. Pumping peaks are shown to be in agreement with the generation of the strongest magnetic concentration at each cycle of the turbulent pumping profile.

To examine further the dissimilarities in the three cases considered here, standard measures of depth with respect to the maximum value and centre of the magnetic field are applied (Wissink *et al.*, 2000; Tobias *et al.*, 2001). These quantities are given by

$$z_{max} \; = \; z \Big| \max_z \langle B_y \rangle (z) \, , \tag{3.33}$$

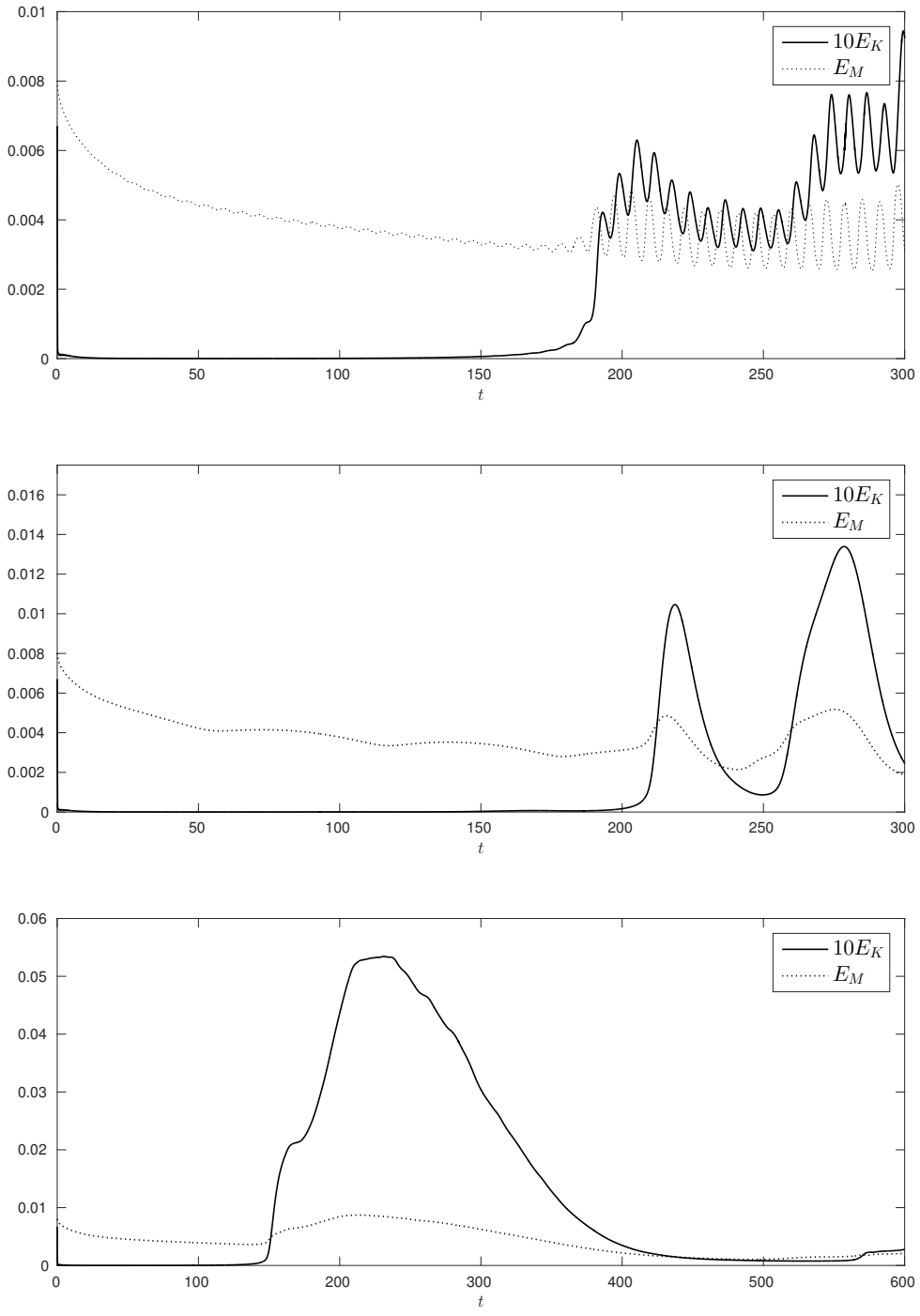

Figure 3.9: Temporal evolution of the total kinetic energy and magnetic energy for Case 1 (top panel), Case 2 (middle panel), and Case 3 (bottom panel). The kinetic energy is scaled up by a factor of 10 to ease comparison with the magnetic energy. Note that Case 3 is shown for a longer period than Cases 1 and 2 to consider a complete pumping cycle.

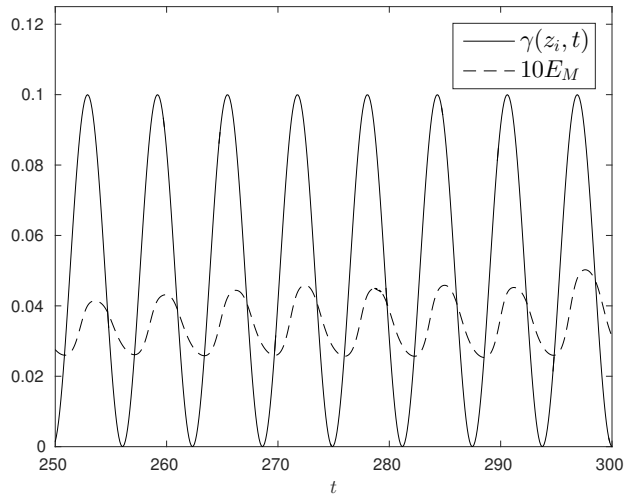

Figure 3.10: Comparison between the variation of the imposed pumping profile and magnetic energy for Case 1. The magnetic energy is scaled up by a factor of 10 to ease comparison with the γ-pumping profile.

and

$$z_B \;=\; \int_0^1 z\langle B_y\rangle \,\mathrm{d}z \Big/ \int_0^1 \langle B_y\rangle \,\mathrm{d}z\,, \tag{3.34}$$

respectively, where $\langle B_y\rangle = \iint B_y \;\mathrm{d}x\mathrm{d}y$. In addition, the fraction of magnetic flux present in the part of the domain above the initial location of the magnetic field ($z_1 = 0.6$) is quantified and given by

$$\Phi \;=\; \int_0^{0.6} \langle B_y\rangle \,\mathrm{d}z \Big/ \int_0^1 \langle B_y\rangle \,\mathrm{d}z\,. \tag{3.35}$$

The evolution of z_{max}, z_B, and Φ in time is shown in Figure 3.11 for Cases 1−3. A general decline in z_{max} is initially observed as the magnetic field is subject to diffusion. This is shortly restored by the magnetic buoyant force, leading to the rise of magnetic fields within the lower region of the domain. Interactions between the γ-pumping and magnetic buoyancy become more pronounced, after $t \approx 50$, once the redistribution of the magnetic flux reaches the interface region. This competition continues along with the generation of magnetic flux concentrations, near z_B.

The depth to which maximal magnetic strengths are achieved, z_{max}, in time

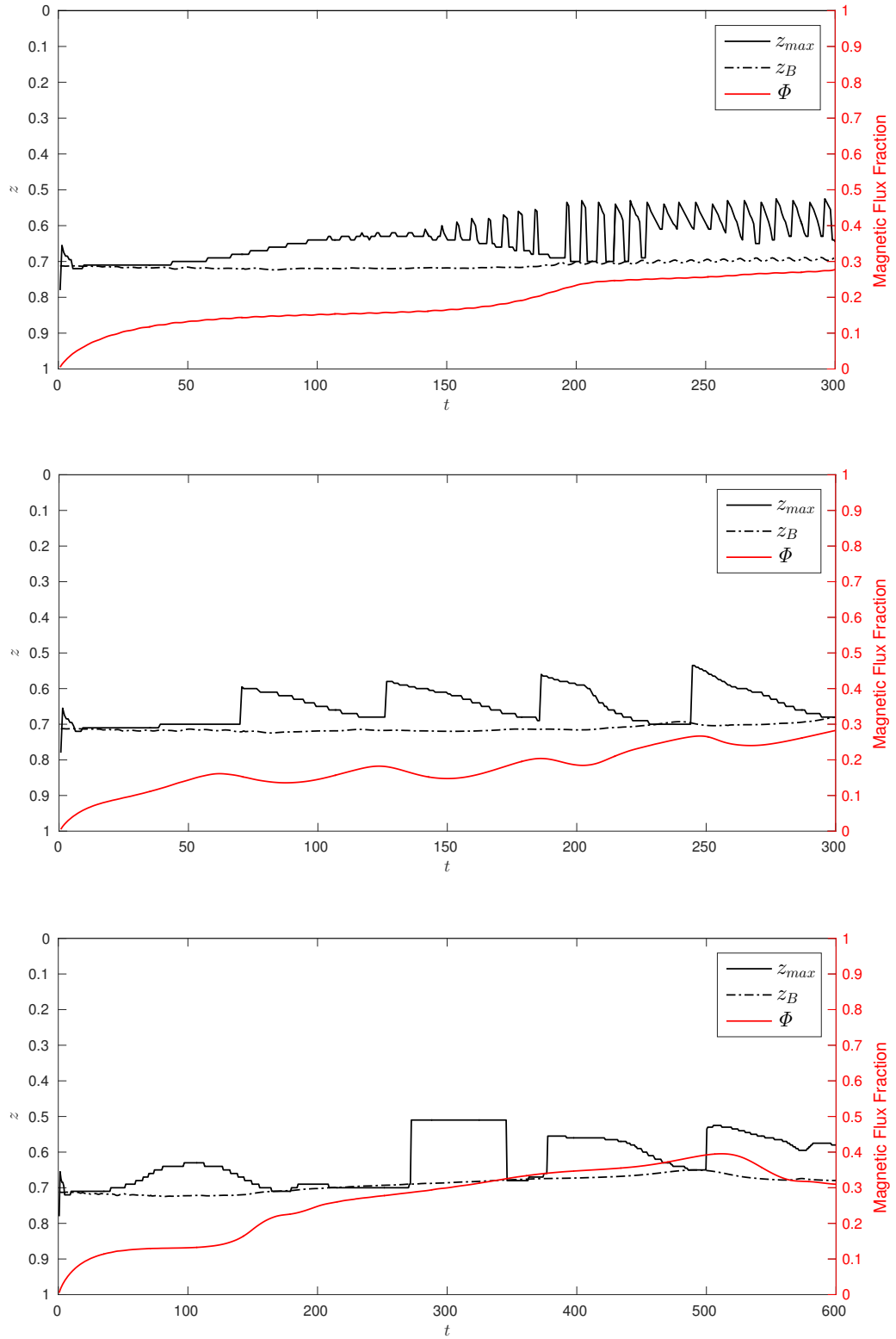

Figure 3.11: The location of the maximum magnetic field, z_{max}, location of centre of magnetic field, z_B, and the magnetic flux fraction contained above the initial location of magnetic field, Φ, in time, for Case 1 (top panel), Case 2 (middle panel), and Case 3 (bottom panel).

vary depending on the particular choice of k. In Case 3, for instance, since the pumping evolves on a slower pace, the intensification and breakout of the magnetic field occur over a longer timescale. However, in Case 1, the dynamics are observed to be more varied, where local field amplification occurs more frequently. Generally, for all cases, the bulk of the field is maintained at the lower fraction of the domain, as shown by the global measure z_B. The variable Φ highlights the effect of the γ-pumping on the dispersion of magnetic field above where it is initially located. The fraction of magnetic flux is shown to be greater for Case 3, reaching approximately 40% of the total initial flux, which indicates that magnetic concentrations can spread further for slower temporal variations in the γ-pumping.

3.4 Conclusion

In this chapter, I have focused on examining the influence of time-dependent γ-pumping on the formation and evolution of buoyant structures, using an idealised mathematical framework. All the simulations began with an initial state, thermally perturbed, giving rise to buoyancy-driven magnetic structures at the surface of the discontinuous magnetic layer. Similar to the earlier work of Barker *et al.* (2012), the homogeneous magnetic slab, initially imposed in the lower layer, remains below the interface with only locally intense concentrations of magnetic flux rising against the γ-pumping. In other words, only structures where the magnetic field strength is comparable to equipartition strength are able to overcome the overlying pumping and rise. However, the effect of time-dependent γ-pumping was found to introduce a more complex evolution than previously recognised, where magnetic structures rise unhindered once the equipartition threshold was attained. In all cases considered, rising magnetic structures were shown to be regularly pushed down and repelled back up depending on the temporal evolution of the magnetic pumping. Furthermore, the competition between buoyant magnetic structures and downward, time-dependent pumping velocity was found to alter various properties

of the emerging magnetic flux structures.

Results from the three different pumping timescales considered revealed that the strength of magnetic concentrations, the rate of magnetic emergence, and the spread of magnetic field all depend on the characteristics of the pumping profile. The degree of magnetic emergence was found to directly correlate with the frequency of the imposed γ-pumping. Additionally, the intensity of flux structures was found to vary significantly with the choice of pumping timescale. Slower temporal variations in the pumping profile were found to permit magnetic structures of higher magnetic strength to travel further into the pumping zone.

In this model, I sought to explore the general impact of time-dependent pumping on the action of emerging magnetic structures. However, based on theoretically derived estimates of convective turnover timescale, Kim and Demarque (1996) defined two different convective timescales: a global, large-scale, convective turnover time for the complete convection zone and a local, smaller-scale, convective turnover time near the base of the convection zone. Measurements of the local solar convective timescale, in terms of the variable k, approximately fall within $k < 0.001$. Unfortunately, such calculation is not easily accessible in the current modelling framework. However, the gradual reduction in the magnitude of k provided meaningful patterns of the rising magnetic structures. Furthermore, the proposed model in this chapter assumes a regular periodicity in the pumping, which is unlikely to occur within the Sun, but it does reveal that the evolution of buoyant magnetic structures is greatly influenced by the changes in convection. Structures of sufficient strength, relative to the downward motions, will rise and can reach the solar surface. Weaker structures will be halted in the ascent and then will interact with the turbulence, forming part of the interface dynamo model.

Finally, while the principal motivation for this study was to better under-

stand events at the base of the convection zone, the solar photospheric layer also displays variation in the timescale of convective motions as well as in the scales of emerging magnetic structures through, for instance, granulation patterns (Cattaneo and Hughes, 2001; Priest, 2014). Therefore, a by-product of the work here is to give an insight into the dynamics driven by convective turbulence and magnetic fields in the photospheric region. The γ-pumping considered with the fastest time variation showed frequent rise of relatively weak, compared to the other cases considered, magnetic structures. This is clearly not the situation deep in the convection zone, but it is very likely in the near surface region of the Sun, where granular magnetic loops are observed to appear very frequently in small magnetic concentrations.

Chapter 4

The Interaction of Buoyant Magnetic Structures with Convective Plumes

4.1 Introduction

Until the late 1970s, solar physicists situated the mechanism maintaining solar dynamo entirely in the highly-turbulent convection zone, where magnetic fields undergo repeated stretching and folding due to the underlying turbulence (Parker, 1955b; Babcock, 1961; Steenbeck and Krause, 1969). It was then realised that magnetic fields could not fully be generated in the convection zone as the field can feedback on the flow in such a way as to disrupt the regeneration rate of the magnetic field, and so leading to spatial and temporal inconsistencies with the magnetic features observed on the solar surface (see Parker, 1975; Silvers, 2008 and references therein). The idea of an interface-type dynamo, partially situated in the stable overshoot layer just below the convective zone was put forward by Parker (1993), where the existence of a toroidal field in the tachocline was assumed due to the presence of important physical processes that can influence the generation and sustenance of a large-scale field (see Section 1.2).

This solar interface dynamo model was built on the mechanisms of magnetic field transport within the solar interior. In the convection zone, transport of flux is enhanced, relative to the underlying sub-adiabatic layer, due to turbulent convective motions (MacGregor and Charbonneau, 1997; Tobias *et al.*, 2001). Poloidal magnetic fields are primarily expelled to the tachocline as a result of turbulent diffusivity, while the shear-generated toroidal components are believed to reside within the low diffusion environment in the tachocline.

The non-linear interactions between compressible turbulence and the underlying, large-scale toroidal component of the magnetic field serve to transport magnetic flux into the stellar atmosphere. Emergence of magnetic flux tubes is considered to be triggered by instabilities of the field in the non-turbulent tachocline (Tobias and Weiss, 2007). Most notably, the process driven by magnetic buoyancy instability (Parker, 1955a) due to an unstable vertical gradient of the horizontally aligned magnetic field (see Subsection 2.4.2). However, there remain some uncertainties on the exact physical mechanisms that allow fairly strong magnetic structures to traverse the turbulent convection zone.

Inspired by the mechanism of magnetic flux emergence that yields the observed solar features, Barker *et al.* (2012) conducted a pilot study of the effects of turbulent flux pumping on the evolution of buoyancy instability, in a framework resembling the base of the convection zone. Results from their numerical calculations establish an equipartition relation between the Alfvén speed of the magnetic field and the pumping velocity under which the evolution of the large-scale field is determined; proposing a possible mechanism of suppressing the field before magnetic buoyancy instabilities play a significant role in the emergence of flux tubes.

Following this, given that convective patterns are highly time-dependent, Chapter 3 built on the model of Barker *et al.* (2012) to account temporal characteristics of the magnetic flux pumping and explore its effect on the formation and

evolution of magnetic structures. The rate of emergence of magnetic structures, as well as their strengths, were found to be related to the temporal characteristics of the imposed pumping. The results reported by Barker *et al.* (2012) and in Chapter 3 (published in Ali and Silvers (2018)) were based on mean-field approximations where a net transport of mean magnetic field, that results from the non-isotropic parts of the mean electromotive force expansion, is adapted to simplify the effects of turbulent convection (see Subsection 2.4.3).

Parametrisation of the small-scale turbulent pumping does reveal interesting properties relating to the emergence of magnetic structures throughout the convection zone. However, simplifications of the pumping mechanism may not capture the various physical factors that contribute to the overall dynamics of the magnetic field. The research presented in this chapter will focus on exploring the conclusions in the studies of Barker *et al.* (2012) and Chapter 3 in a more realistic attempt of modelling magnetoconvection, by establishing a radial pumping that arises naturally from the turbulent convective flow.

Earlier studies have looked at such magnetoconvection interactions (Nordlund *et al.*, 1992; Brandenburg *et al.*, 1996; Tobias *et al.*, 1998, 2001), but focused on the role of turbulent convection in transporting and storing the underlying magnetic field. Here, I aim to investigate the transport of magnetic structures through the turbulent convection zone, and mainly focusing on the effect of the equipartition criterion established in the previous work of Barker *et al.* (2012) and Chapter 3, in a framework of fully compressible convection.

Despite that convection in two-dimensions represents simplifications of the real-world three-dimensional convective problems, it provides an understanding of how the physical properties imply to three-dimensions. Furthermore, two-dimensional simulations require fewer demands in terms of computational power than three-dimensional simulations. Thus, as a first step in understanding the problem, quasi two-dimensional numerical experiments of compressible

magnetohydrodynamics are performed. This is followed by numerical simulations extended to three-dimensions, to explore and compare with the quasi two-dimensional findings.

4.2 Model

As in Chapter 3, a localised Cartesian system is considered with a plane layer of compressible fluid extending from $0 \leq x, y \leq \lambda_{x,y}$ in the horizontal direction, and $0 \leq z \leq d$ increasing vertically downwards, parallel to the constant gravitational acceleration. Throughout the domain, the fluid is assumed to satisfy the perfect gas law with the dynamic viscosity, μ, the magnetic diffusivity, η, the gravitational force, g, the specific heats at constant density and pressure, c_v and c_p respectively, all constant. Thus, the set of non-dimensional compressible MHD equations reads

$$\frac{\partial \rho}{\partial t} + \nabla \cdot (\rho \boldsymbol{u}) = 0, \tag{4.1}$$

$$\rho\left(\frac{\partial \boldsymbol{u}}{\partial t} + (\boldsymbol{u} \cdot \nabla)\boldsymbol{u}\right) = -\nabla p - \nabla\left(\frac{F|\boldsymbol{B}|^2}{2}\right) + F(\boldsymbol{B} \cdot \nabla)\boldsymbol{B} + \sigma C_k(\nabla \cdot \boldsymbol{\tau}) + \rho g \hat{\boldsymbol{z}}, \tag{4.2}$$

$$\frac{\rho}{(\gamma_s - 1)}\left(\frac{\partial T}{\partial t} + (\boldsymbol{u} \cdot \nabla)T\right) = -p\nabla \cdot \boldsymbol{u} + \frac{\gamma_s C_k}{(\gamma_s - 1)}\nabla \cdot \big(K \nabla T\big) + C_k\left(F\zeta_0|\nabla \times \boldsymbol{B}|^2 + \frac{\sigma \tau^2}{2}\right), \tag{4.3}$$

$$\frac{\partial \boldsymbol{B}}{\partial t} = \nabla \times (\boldsymbol{u} \times \boldsymbol{B} - C_k \zeta_0 \nabla \times \boldsymbol{B}), \tag{4.4}$$

$$\nabla \cdot \boldsymbol{B} = 0, \tag{4.5}$$

$$p = \rho T. \tag{4.6}$$

Initially, quasi two-dimensional simulations will be performed by assuming no gradients of quantities in the y-direction, i.e. motion only exists in the $x - z$ plane. This will be followed by considering the full three-dimensional problem.

In this specific model, the thermal conductivity, K, is assumed to be a function of depth and is scaled by its initial value at the upper surface, K_0. Following this, several non-dimensional control parameters obtained earlier in Chapter 3 are modified. These include the Prandtl number $\sigma = \mu c_p/K_0$, the dimensionless thermal diffusivity $C_k = K_0/\rho_0 c_p d\sqrt{(c_p - c_v)T_0}$, and the ratio of magnetic to thermal diffusivity at the top of the layer $\zeta_0 = \eta c_p \rho_0/K_0$.

The computational domain is split into two piecewise polytropic layers to mimic the interface region between the radiative zone and the convection zone. This is such that the top layer $0 \leq z \leq d/2$ is convectively unstable, and the bottom layer $d/2 \leq z \leq d$ is stable, with a smooth transition between the unstable layer and the stable layer, achieved by a hyperbolic tangent profile. This is built by defining the depth-dependent thermal conductivity as

$$K(z) = \frac{1}{2}\left[\left(\frac{m_B+1}{m_T+1}+1\right) + \left(\frac{m_B+1}{m_T+1}-1\right)\tanh\left(\frac{z-(d/2)}{0.1}\right)\right], \qquad (4.7)$$

where m_T and m_B denote the polytropic indices of the top and bottom layers respectively (see example in Figure 4.1). This approach was adapted in several previous investigations to account the effect of overshooting motions via penetrative convection on the stably stratified region below the convection zone (see Hurlburt *et al.*, 1994; Tobias *et al.*, 1998; Silvers *et al.*, 2009).

For convective instability, the super-adiabatically stratified medium must satisfy $m < 3/2$ for a monoatomic perfect gas (Chandrasekhar, 1939). With the effect of adiabatic expansion (compression) of an ideal gas taken into account, the form of the dimensionless Rayleigh number, Ra, that determines the onset of buoyancy-driven convection in this framework is explicitly given by

$$Ra = \frac{(m_T+1)\theta^2}{\sigma C_k^2 \gamma}(m_T + 1 - \gamma m_T)(1 + (\theta d)/4)^{(2m_T-1)}, \qquad (4.8)$$

where the Ra values quoted in this work are evaluated at the middle of the upper convective layer.

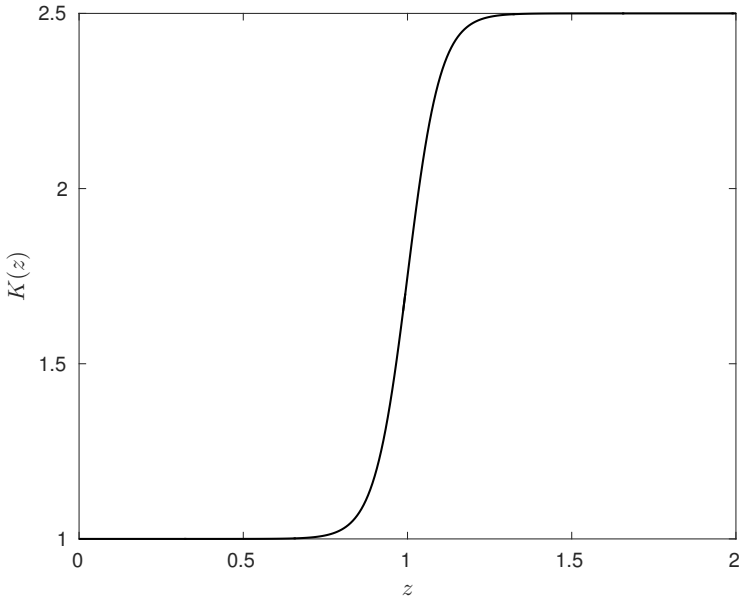

Figure 4.1: The thermal conductivity profile as a function of depth, where $d = 2$, $m_T = 1$, and $m_B = 4$.

To complete the description of this model, boundary conditions must be specified. As in Chapter 3, the system is assumed to satisfy periodic boundary conditions in the horizontal directions. The conditions at the upper and lower boundaries are

$$\begin{aligned} u_z = \frac{\partial u_x}{\partial z} = \frac{\partial u_y}{\partial z} = B_x = B_y = 0, \quad T = T_0 \text{ at } z = 0, \\ u_z = \frac{\partial u_x}{\partial z} = \frac{\partial u_y}{\partial z} = B_x = B_y = 0, \quad \frac{\partial T}{\partial z} = \frac{m_T + 1}{m_B + 1}\frac{\theta T_0}{d} \text{ at } z = d, \end{aligned} \tag{4.9}$$

where the constant heat flux at the bottom of the domain is modified to account for the composite polytropic domain.

For all calculations, an initial hydrostatic state is chosen by setting $\boldsymbol{u} = 0$. Accordingly, the equilibrium solutions for $\rho(z)$ and $T(z)$ are found numerically given the non-linearity of the static state thermal profile in this model. By

assuming no time-derivatives, the energy equation (Equation 4.3) reduces to

$$\nabla \cdot \big(K(z)\nabla T\big) = 0. \tag{4.10}$$

Therefore, choosing the steady state to be independent of horizontal coordinates, the background temperature profile is found by solving

$$K\frac{\mathrm{d}^2 T}{\mathrm{d}z^2} + \frac{\mathrm{d}K}{\mathrm{d}z}\frac{\mathrm{d}T}{\mathrm{d}z} = 0, \tag{4.11}$$

using fourth-order finite-difference subject to thermal boundary conditions (Equation 4.9).

Similarly, the background density profile is calculated by considering the ideal gas law (Equation 4.6) and the reduced momentum equation:

$$\frac{\mathrm{d}p}{\mathrm{d}z} = \frac{gp}{T}. \tag{4.12}$$

The equilibrium solutions are shown in Figure 4.2 for some values of m_T, m_B, θ, and d.

A uniform horizontal magnetic field $\boldsymbol{B} = B_y\hat{\boldsymbol{y}}$ is introduced into the existing hydrodynamic state, in the region bounded by $z = z_1$ and $z = z_2$, at later stages once convection has attained a statistically stationary state. To accommodate the imposed field, the density in the magnetic layer is adjusted so that the system is in equilibrium. This initial configuration is adapted together with the addition of small, random perturbations in the temperature profile. The equations are solved numerically using a parallel hybrid finite-difference/pseudo-spectral code, where time is advanced using a third-order Adams-Bashforth scheme as discussed in Subsection 3.2.5. All simulations, described below, are carried out using a spatial resolution of $256 \times n_y \times 400$, where $n_y = 1,256$ for the quasi two-dimensional and three-dimensional simulations respectively.

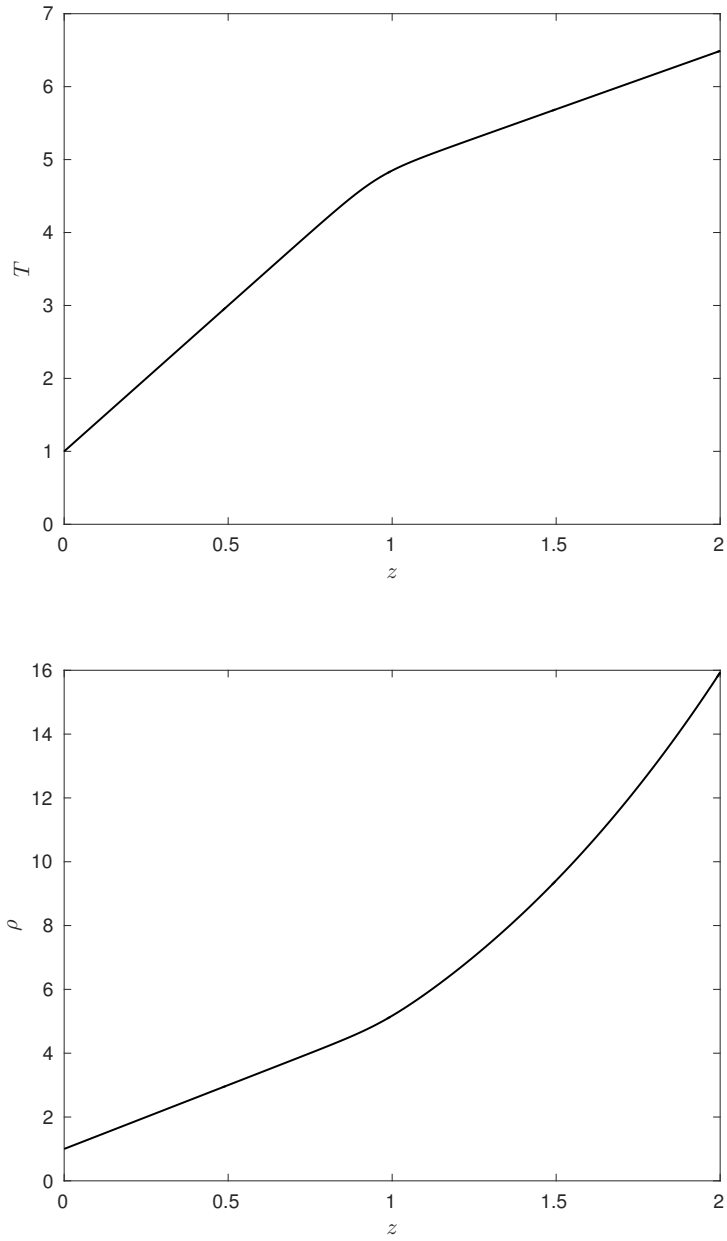

Figure 4.2: Initial background states of temperature (top panel) and density (bottom panel) for $d = 2$, $T_0 = 1$, $\rho_0 = 1$, $\theta = 4$ with $m_T = 1$ and $m_B = 4$.

This model problem is governed by a number of non-dimensional quantities, which leads to a broad parametric space that requires large numerical efforts. In the solar context, the parameter settings are not known exactly, but rather a range of estimates for the parameters are available (see, for example, Priest, 2014). For instance, in the lower parts of the convection zone, the Prandtl number is of order 10^{-6} or less (Brummell *et al.*, 1995; Christensen-Dalsgaard and Thompson, 2007). Current numerical limitations do not allow to simulate the extreme values within the Sun; however the aim is to gain an insight into the underlying physics by choosing appropriate parameter values. The parameter choices are outlined in Table 4.1 [1].

Parameter	Description	Value
σ	Prandtl number	Variable
C_k	Thermal diffusivity	0.07
θ	Thermal stratification	10.0
γ_s	Ratio of specific heats	5/3
ζ_0	Magnetic diffusivity	0.1
F	Magnetic field strength	Variable
m_T, m_B	Polytropic indicies	1.0, 9.0
z_1, z_2	Top and bottom of magnetic layer	1.35, 1.65
λ_x, λ_y	Box horizontal aspect ratio	6.0, 6.0
d	Vertical depth of box	2.0
B_y	Initial Horizontal magnetic strength	1.0

Table 4.1: The choice of parameters for the magnetoconvection model.

With the primary objective of simulating turbulent magnetoconvection, a supercritical convection is considered by setting the thermal stratification $\theta = 10$, specific gas $\gamma_s = 5/3$, thermal diffusivity $C_k = 0.07$, and Prandtl number $\sigma \leq 0.5$. A penetrative configuration is achieved, via the depth-dependent thermal conductivity profile in Equation (4.7), by considering a convectively unstable top layer with polytropic index $m_T = 1$, and a convectively stable bottom layer with polytropic index $m_B = 9$. As described earlier, the horizon-

[1]Prior to the choice of parameters in Table 4.1, some experiments on various convective patterns and their interactions with the magnetic field were conducted. The results are not essential for this chapter but can be found in Appendix A

tal magnetic layer will be introduced in the convectively stable region, with an initial magnetic field magnitude $B_y = 1$, magnetic diffusivity $\zeta = 0.1$, and magnetic field strength F chosen to vary to explore its dependence on flux emergence.

4.3 Results

4.3.1 Quasi Two-Dimensional Simulations

The investigation is initiated by restricting attention to quasi two-dimensional simulations, where the hydrodynamic evolution of the system is focused upon to establish a convective motion before imposing a magnetic layer. The topological structure of the penetrative compressible convection can be seen in Figure 4.3 for the parameter settings in Table 4.1 with $\sigma = 0.01$, which shows snapshots of the vertical velocity, w, and enstrophy density (vorticity squared), $\omega^2 = (\nabla \times \boldsymbol{u})^2$, at a single computational time.

For the w-velocity field, the colours red and blue denote upward and downward motions respectively. The enstrophy density highlights the intensity of the vorticity field, where bright and opaque colours denote strong values of the field, whereas weak values are more translucent. Most of the vorticity is generated at the interface between the stable and unstable regions. The motion in the upper convection layer is of asymmetric nature, with narrow regions of rapid downflow and broad regions of relatively slow upflow due to buoyancy braking. As reported by Hurlburt *et al.* (1984), such asymmetry is stemming from the combined effects of compressibility and stratification.

The background density stratification within the convectively unstable layer varies approximately by a factor of 5, and by a factor of 58 across the entire domain. The presence of the stably stratified lower layer decelerates the motion as it overshoots from above, in addition to reducing the strength of the overturning flow. It is to note that the convective plumes may continue

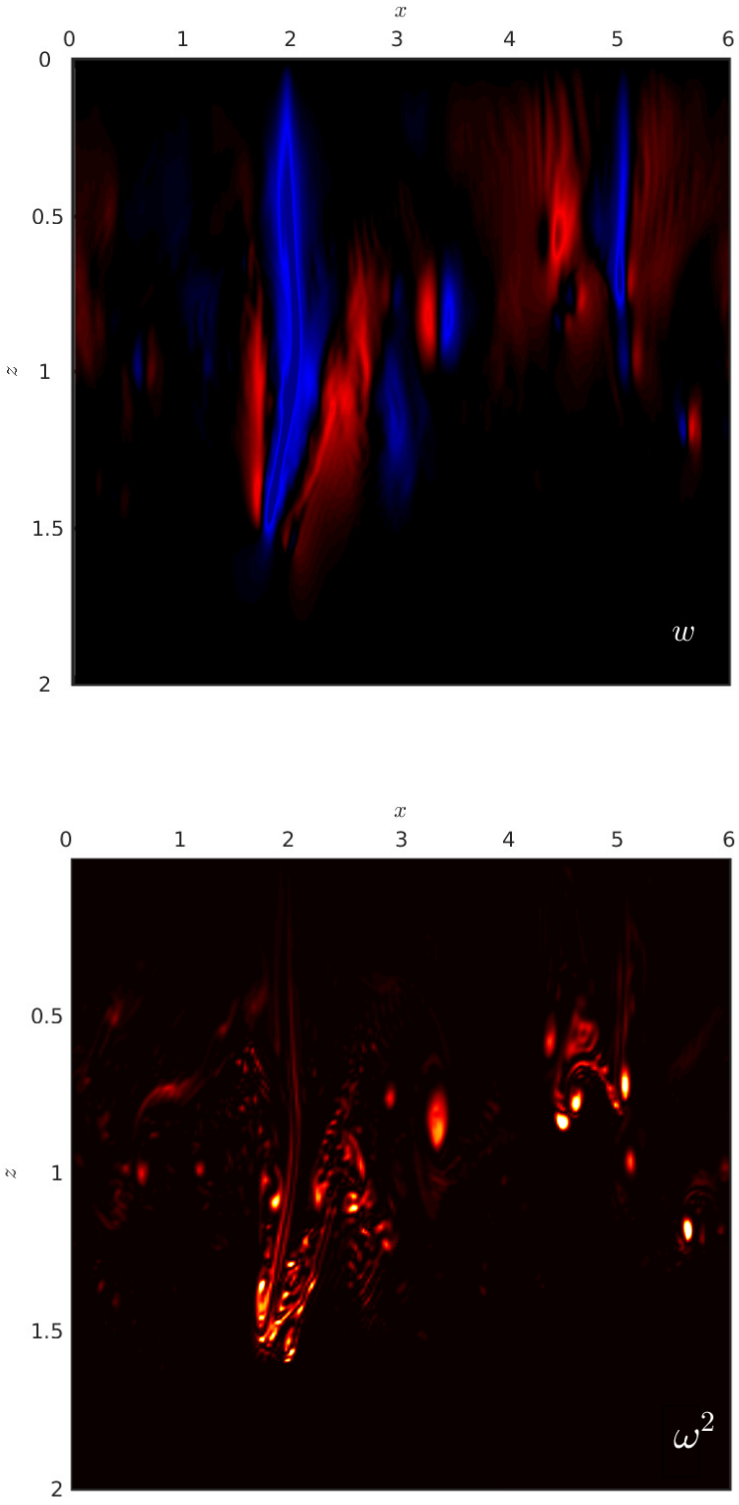

Figure 4.3: Snapshots of the vertical velocity field (top panel) and enstrophy (bottom panel) for $\sigma = 0.01$ at computational time $t = 64.12$. The colours red and blue in the velocity field correspond to upward and downward convective motions respectively. Strong enstrophy densities are yellow, whereas weaker densities are dark and translucent.

to progress through the stable region, and are not confined to the convective region. The extent of overshooting depends largely on the choice of parameters.

To relate the convection simulations to the γ-pumping in Barker *et al.* (2012) and Chapter 3, I look at achieving a scale separation of the motion and extracting the fluctuation field. A simple way to obtain scale separation is by decomposing the velocity field in terms of mean and fluctuating parts (Steenbeck *et al.*, 1966; Moffatt, 1983; Currie, 2016). Given that the pumping in the investigations of Barker *et al.* (2012) and Chapter 3 was depth-dependent, I choose to look at the fluctuation field of the vertical velocity in the z-direction. Figure 4.4 displays temporal line graphs of the average w-velocity, $\bar{w}$, and the small-scale fluctuations, w', over horizontal coordinates for the parameters in Table 4.1 with $\sigma = 0.01$, and two additional turbulent flows with $\sigma = 0.1$ and 0.5. This is such that $Ra = 4.9 \times 10^6$, 4.9×10^5 and 9.8×10^4 respectively.

Figure 4.4 shows, as expected, that at high supercritical Rayleigh numbers non-linear effects lead to the further development of turbulence (Busse, 1985; Koschmieder, 1993), and so introduces greater variability in the field. The γ-pumping extracted in the previous work of Barker *et al.* (2012) and Chapter 3, does seem appropriate to portray this small-scale turbulence of the field in a simplified manner and isolate the action of turbulence on the large-scale magnetic field. Note that the vertical fluctuation scales are extremely small, as opposed to the γ-pumping amplitudes imposed in Barker *et al.* (2012) and Chapter 3. This is due to the computationally feasible choices of Ra in this model, which are small compared to that of the Sun, where $Ra \sim 10^{20}$ (Spiegel, 1971).

As opposed to a dynamo-generated magnetic field (see, for example, Cline *et al.*, 2003; Vasil and Brummell, 2008; Silvers *et al.*, 2009), the magnetic slab is introduced to the non-convective region, similar to the approach conducted by Tobias *et al.* (1998, 2001). Once the convective flow has fully developed for

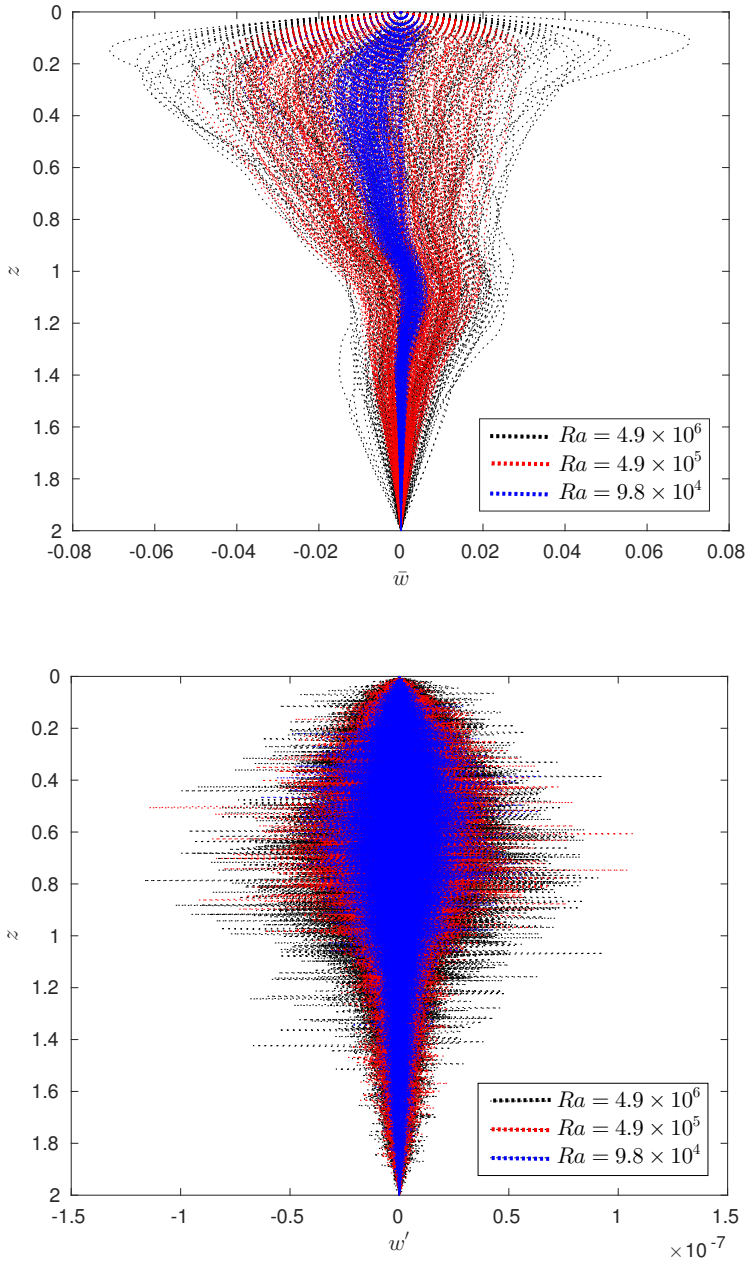

Figure 4.4: Temporal line graphs of the average component (top panel) and fluctuating component (bottom panel) of the w-velocity field for several Ra values.

$\sigma = 0.01$, the horizontally aligned magnetic field is inserted in the stable region of the domain. The magnetic field is imposed in the region $1.35 \leq z \leq 1.65$ by balancing the magnetic pressure and the gas pressure, to maintain the original pressure distribution. The discontinuity in the initially imposed magnetic field rapidly leads to diffusion at the interface. More significantly, the field is susceptible to instabilities driven by magnetic buoyancy. The convective motion penetrating the stably stratified layer induces distortion in the magnetic layer, with some of the magnetic flux transported through the convection zone, while the bulk of the field is maintained in the overshoot region.

To highlight the magnetoconvection interactions, Figure 4.5 shows snapshots of the horizontal component of the magnetic field, together with the vertical velocity field, for magnetic strength $F = 0.0001$. Initially, the field in Figure 4.5(a) appears as a thin slab of strong horizontal magnetic field embedded in the lower region. After a short time, the buoyancy-driven magnetic field interacts with the overshooting convection. Magnetic flux can be seen to rise in Figure 4.5(b), resulting from the combined effects of magnetic buoyancy and advection by the upflows (as indicated in red).

Figures 4.5(c)-4.5(d) depict strong downward plumes piercing into the stable layer, with local magnetic field amplification occurring within the vicinity of the downflow due to stretching of the magnetic field lines, in addition to the complex interactions due to the small-scale vortical motions. This behaviour was also identified in Barker *et al.* (2012) and Chapter 3 as the magnetic field interacts with the overlying downward turbulent pumping. The system acts to restrain the magnetic field in regions where the motion is downward. Figures 4.5(f)-4.5(h) continue to show the dynamics of the magnetic field as it interacts with the overlying plumes, while it is largely maintained in the stable layer.

To define the magnetic buckling effects as structures of sufficient strength that are able to overcome the convective region or simply the advection of the

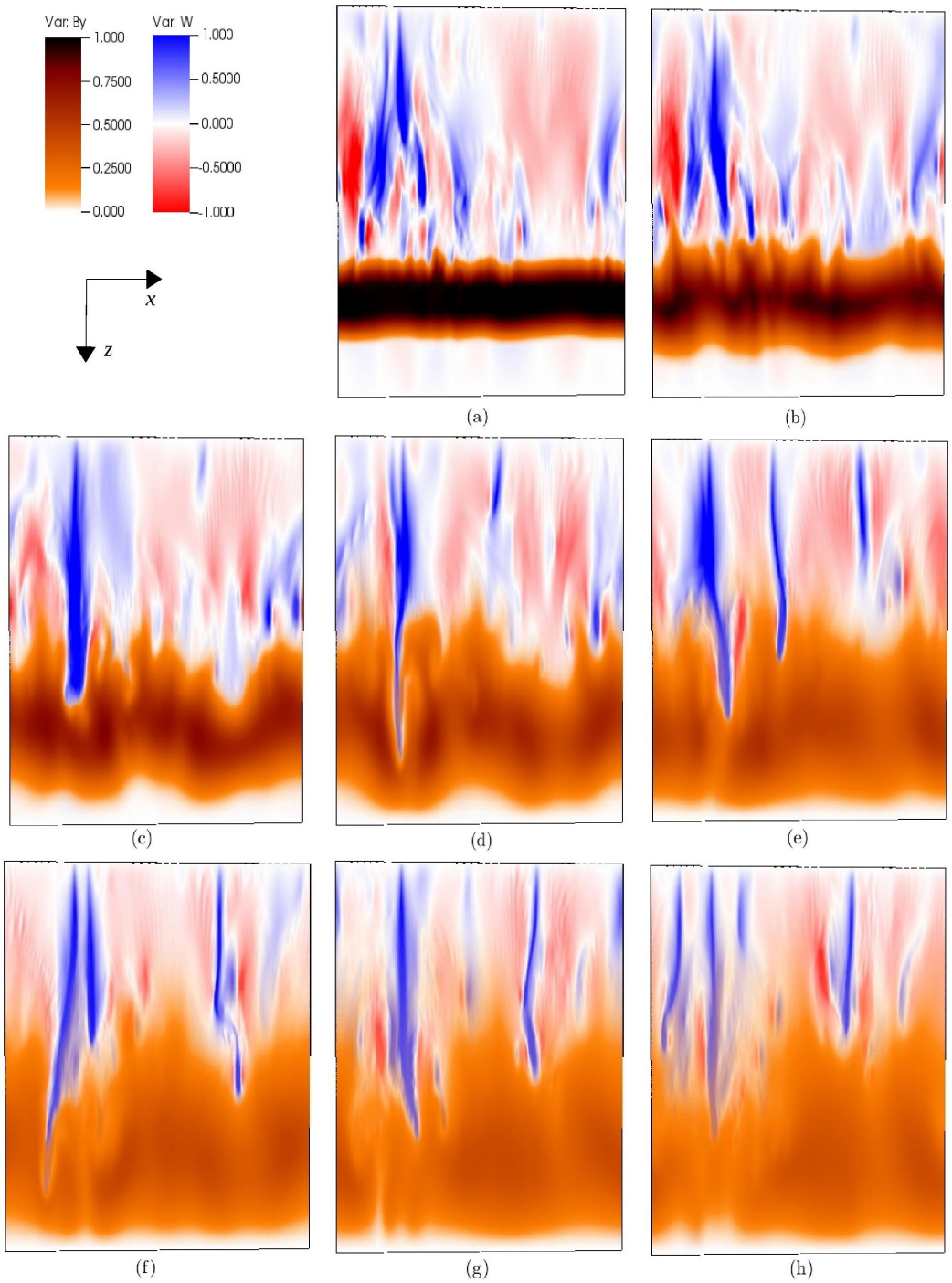

Figure 4.5: Snapshots of the z-component of the velocity field overlaid with the y-component of the magnetic field at computational times (a) $t = 40.68$, (b) $t = 41.21$, (c) $t = 42.03$, (d) $t = 43.04$, (e) $t = 44.50$, (f) $t = 45.73$, (g) $t = 46.87$, and (h) $t = 47.92$ respectively.

magnetic field by the flow in a passive manner, kinetic and magnetic energies need to become comparable (equipartition), given that the back reaction of the magnetic field becomes of significant importance (Cattaneo and Vainshtein, 1991; Silvers, 2008). Magnetic fields need to achieve an equipartition strength with the flow, on a local scale, to escape through the convective motions, as found in the turbulent pumping model of Barker *et al.* (2012) and Chapter 3, or otherwise are transported passively. Initially, on a global scale, the magnetic field appears to be a weak field. Though, this could give rise to local small-scale structure of the magnetic field with energy comparable to the kinetic energy of the flow.

To distinguish the behaviour of the magnetic field, the equipartition of energy is investigated in Figure 4.6 for a stronger magnetic field strength $F = 0.1$, by calculating the ratio of kinetic energy to magnetic energy. Values greater than unity suggest that the magnetic field is influenced by the surrounding convective motions, whereas values less than unity suggest that the magnetic field is able to resist the surrounding motions, and so rises. According to the equipartition measure, the magnetic field in Figure 4.6(a) predominantly behaves with respect to the surrounding motions, which in this case causes buoyant magnetic structures to rise further. As time evolves, Figure 4.6(b) reveals small-scale magnetic structures of equipartition strength developing at various regions in the domain. However, these structures do not progress further through the upper layer, as one would imagine, due to the frequent mixing of the overlying turbulent convection. The locality of the equipartition strength achieved by the magnetic field does not overcome the motion as the magnetic structure continues to rise.

From Figure 4.6(c), less than 4% the strength of the initially imposed magnetic field emerges through the convective layer, as a result of magnetic buoyancy and advection by the upflows, with some stages where the magnetic energy overcomes the kinetic energy. However, unlike in the previous investigations

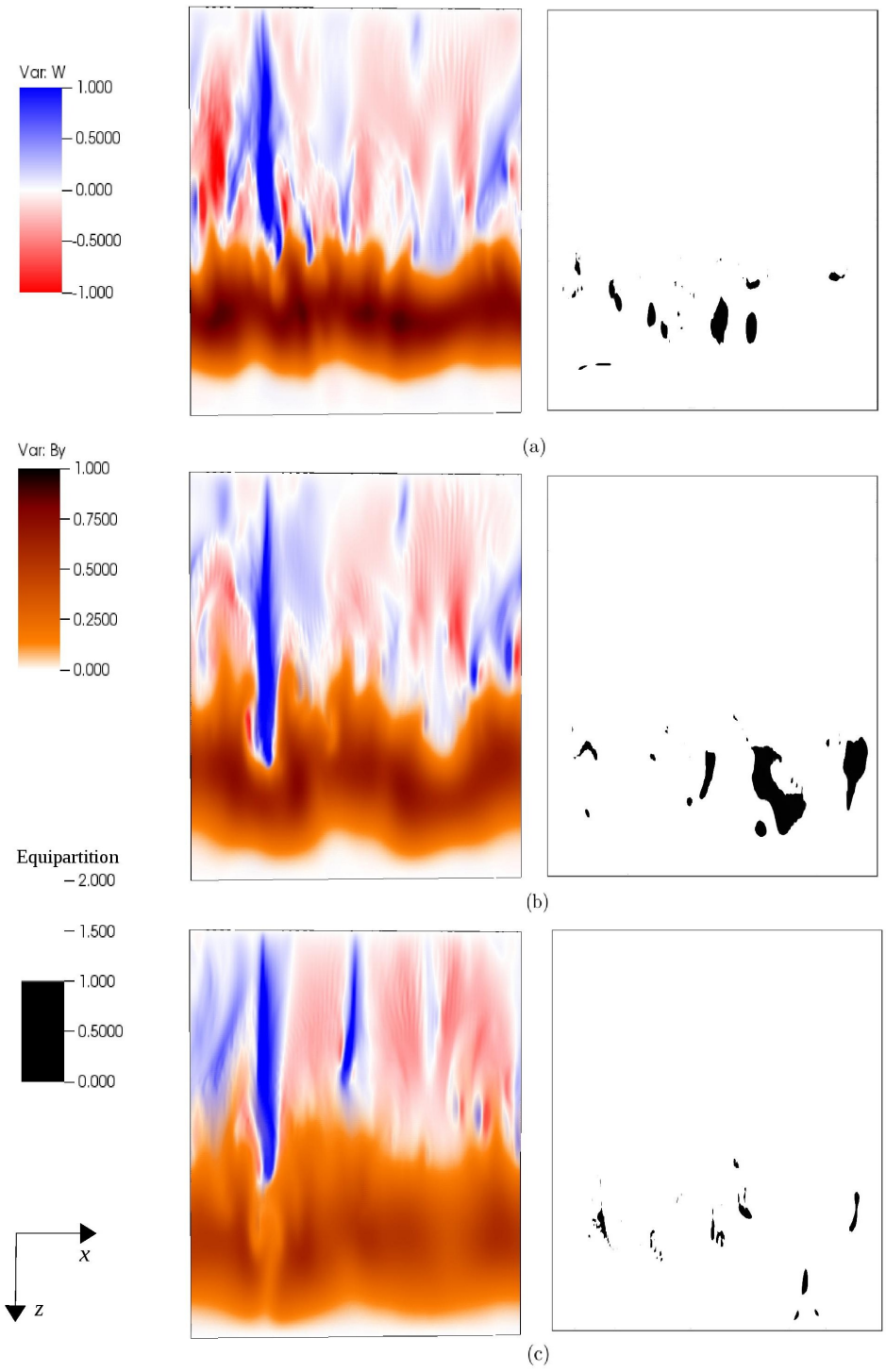

Figure 4.6: Snapshots of the the z-component of the velocity field overlaid with the y-component of the magnetic field (left) and ratio of the kinetic to magnetic energy (right) at (a) $t = 40.68$, (b) $t = 41.21$, and (c) $t = 42.03$ respectively.

of Barker *et al.* (2012) and in Chapter 3, the efficient rise of equipartition-strength magnetic structures are not yet clearly captured.

By increasing the strength of the field to $F = 1.0$, one allows magnetic structures of equipartition level to be reached easily. Figure 4.7 reveals a stage where a magnetic structure escapes to the convective layer. From the equipartition plot, the magnetic energy overcomes the kinetic energy throughout the region of emergence, thus suggesting the rise of the magnetic field despite the surrounding convective motions. This behaviour continues at various locations in Figures 4.7(a) and 4.7(b). However, these findings remain inadequate to conclude the emergence of magnetic structures, comparable to equipartition strength, throughout the convection zone. This is partially due to turbulent motions appearing weak when emergence takes place in the regime where the magnetic energy overcomes the kinetic energy – in addition to the possible contribution of increasing F, which involves amplitude reduction of convective motions in the traverse direction due to magnetic tension, and enhanced buoyancy effect of localised magnetic structures due to magnetic pressure (Bushby and Archontis, 2012).

The redistribution of the magnetic field is examined by calculating the evolution of the average horizontal magnetic field in the y-direction, for various magnetic strengths in the range $10^{-4} \leq F \leq 1$. Generally, the mean magnetic field plays a passive role for all cases and is relatively insensitive to the choices of F on a global scale, as was also identified in Tobias *et al.* (2001). Accordingly, I choose to fix $F = 0.01$, and display the analysis of the horizontally-averaged magnetic field for $\sigma = 0.01$ and $\sigma = 0.1$.

Figure 4.8 represents the magnetic flux redistribution as line graphs for equally-spaced time intervals, and as colour-coded spacetime diagrams that display a colour, with respect to the amplitude of the magnetic field, in both space and time. For both flows, $\sigma = 0.01$ (top panel of Figure 4.8) and $\sigma = 0.1$ (bottom

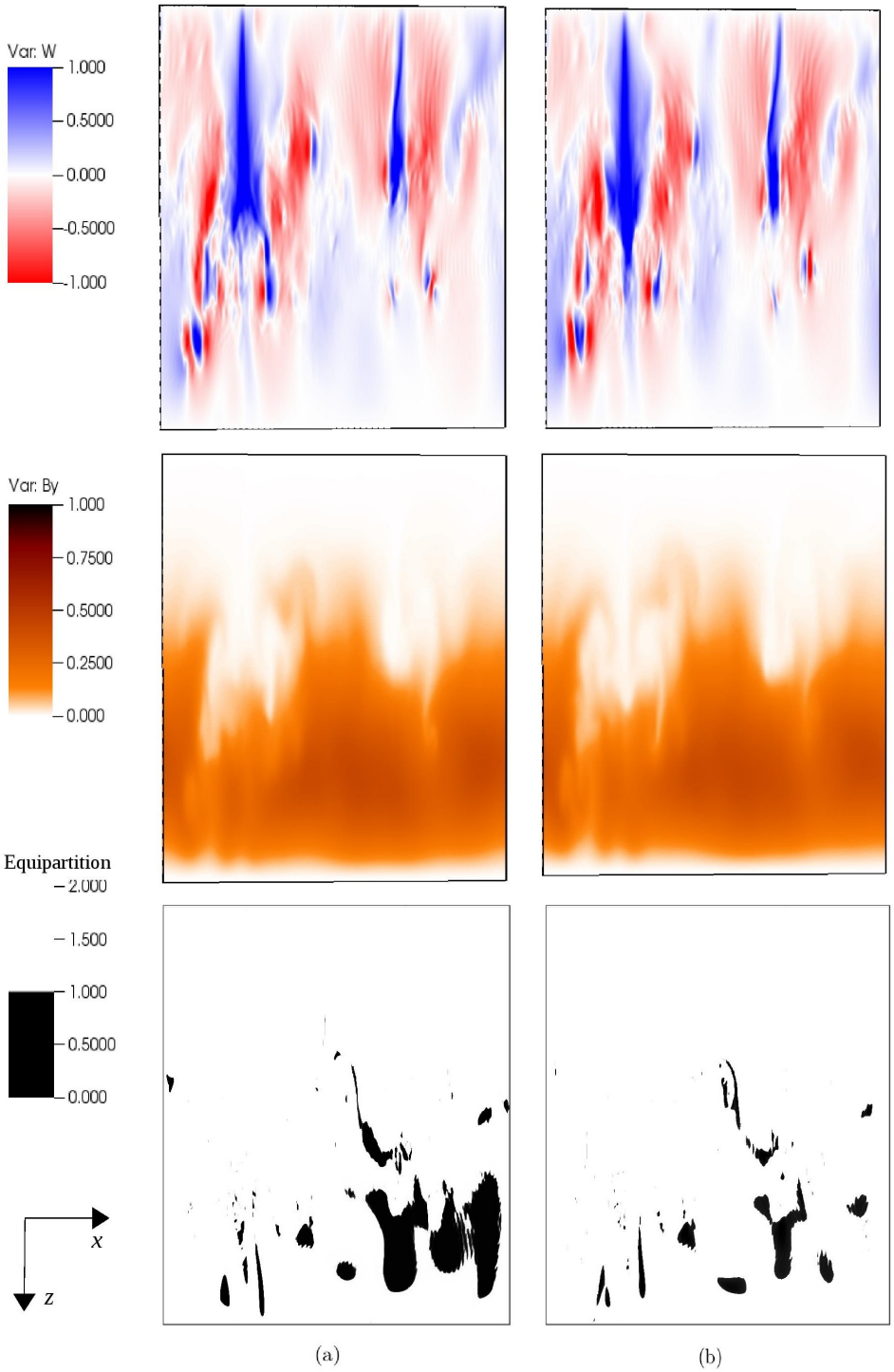

Figure 4.7: Snapshots of the z-component of the velocity field (top), the y-component of the magnetic field (middle) and ratio of the kinetic to magnetic energy (bottom) at (a) $t = 46.31$ and (b) $t = 46.56$ respectively.

panel of Figure 4.8), the evolution starts with the magnetic field contained in the region where it is initially introduced (as displayed in solid line). The peak strength remains located within that region, while it decreases in magnitude as it spreads toward the unstable layer. Some of the flux can be seen to escape through the boundaries, hence reducing the total amount of magnetic flux. Additionally, as time evolves, the magnetic field decays in strength due to the absence of mechanisms that generate the field. This is expected as this model represents magnetoconvection rather than dynamo interactions.

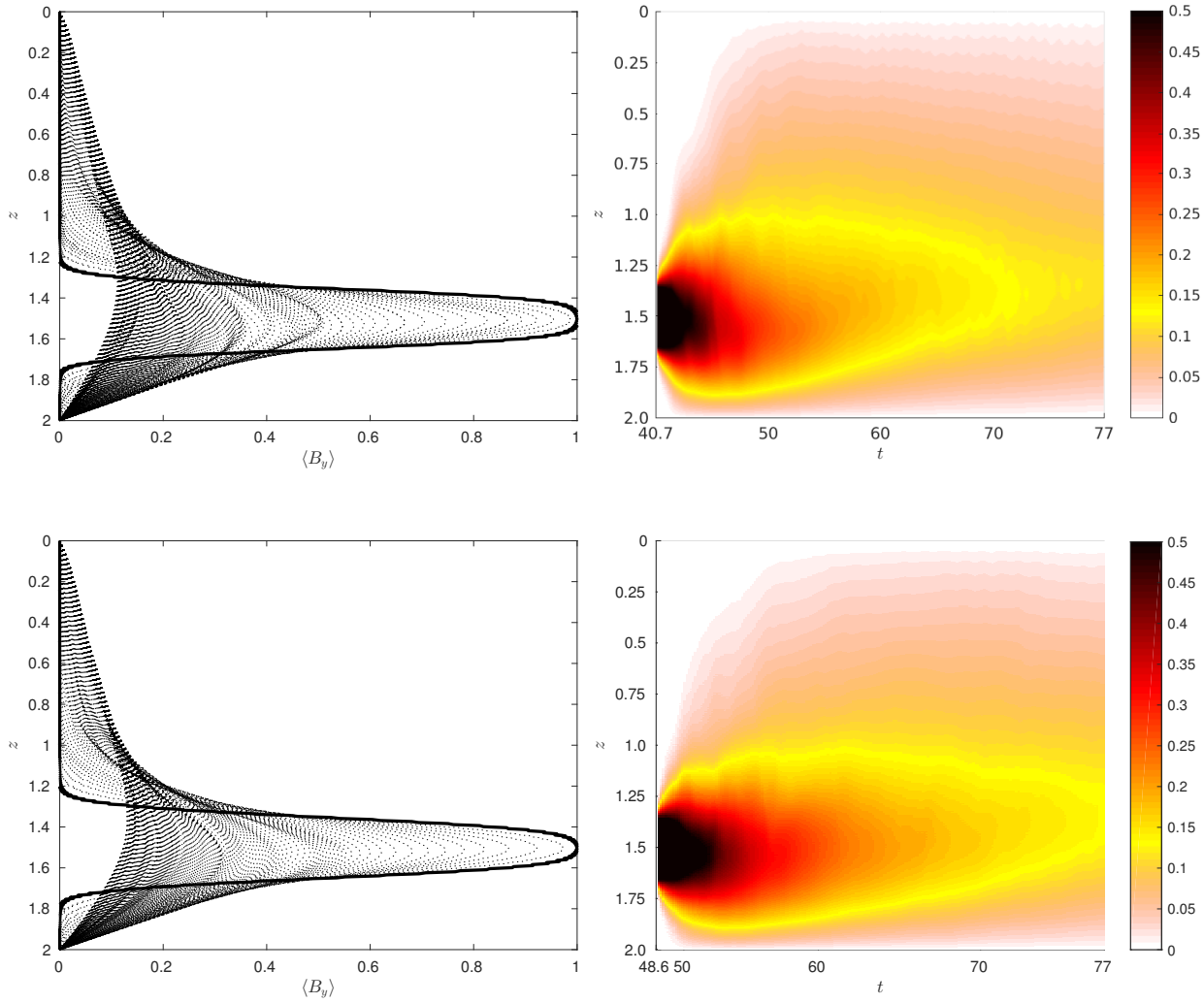

Figure 4.8: Line graphs (left) and colour spacetime diagrams (right) of the horizontal average of the magnetic field in the y-direction, B_y for $\sigma = 0.01$ (top panel) and $\sigma = 0.1$ (bottom panel), where $F = 0.01$.

From both line graphs and spacetime diagrams, greater dispersal of the magnetic field can be noticed for $\sigma = 0.01$. This is a result of the local amplification of the field in the more turbulent flow that leads to the emergence of small-scale, equipartition strength magnetic structures, in addition to the transport of the field by ascending flows.

The fraction of magnetic flux present in the part of the domain above the initial location of the magnetic field ($z_1 = 1.35$), and the measure of depth with respect to the maximum value are quantified by

$$\Phi = \int_0^{1.35} \langle B_y \rangle \, \mathrm{d}z \Big/ \int_0^1 \langle B_y \rangle \, \mathrm{d}z \,, \tag{4.13}$$

and

$$z_{max} = z \Big| \max_z \langle B_y \rangle (z) \,, \tag{4.14}$$

respectively. Figure 4.9 displays Φ and z_{max}, for $\sigma = 0.01, 0.1$ and 0.5, for 30 time units after the field is imposed, in order to minimise the influence of the upper boundary as the simulation progresses. Given that the field is imposed at different computational times for each flow, time is normalised to unity to allow direct comparisons. Interestingly, as fluctuations in the convective flow increase, Φ reveals a greater proportion of magnetic flux in the upper layer during the early stages of the interaction. This indicates the contribution of the equipartition relation in transporting magnetic structures, which is more pronounced as the flow increases in turbulence (case $\sigma = 0.01$). However, as time evolves the strength of magnetic structures reduce, as noted in Figure 4.8, and so equipartition-strength magnetic structures are unlikely to play a significant role. Therefore, advection becomes the predominant mechanism for magnetic field transport, where the least turbulent convective flow (case $\sigma = 0.5$) succeeds in carrying larger quantities of magnetic field throughout the upper domain.

The measure z_{max} emphasises the effectiveness of the overlying pumping on

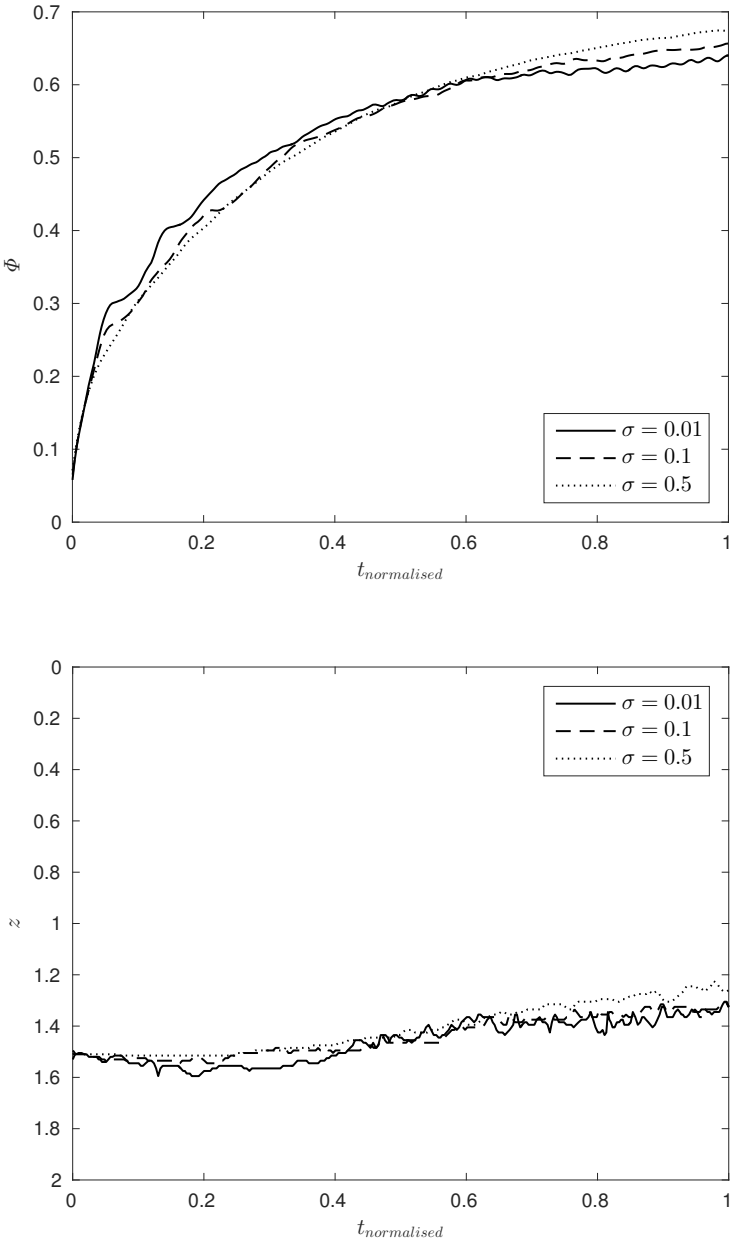

Figure 4.9: The temporal evolution of the magnetic flux fraction contained above the initial location of magnetic field, Φ, (top panel) and the location of the maximum magnetic field, z_{max} (bottom panel).

the imposed magnetic field. From all three cases of σ, strong concentrations of the field are shown to be maintained deeper, with respect to z, for flows of enhanced turbulence. This means that overshooting convective plumes are more efficient in pushing magnetic fields downwards in the case where $\sigma = 0.01$.

4.3.2 Three-Dimensional Simulations

To allow a fuller treatment of the problem, three-dimensional simulations are conducted for some of the cases considered in the preceding subsection. Several differences in the physical properties of the convective flow become apparent, as the 3D simulations are compared with their equivalent quasi 2D simulations. Snapshots of the vertical velocity for $\sigma = 0.1$ are shown in Figure 4.10 in both quasi 2D and full 3D, at different stages in time once the convective patterns are developed. It emerges, from the vertical velocity field in quasi 2D and the horizontal cross-section at $y = 1$ in 3D, that plume structures become noticeably different near the interface region. In 3D, the flow is dominated by small convective structures, while contrastingly, quasi 2D reveals more coherency within the flow, in addition to the effective penetration towards the underlying stably stratified layer.

Evaluation of the horizontally average vertical velocity profiles in Figure 4.11 depicts the substantial change in the dynamics of the convective flow as one transitions from quasi 2D simulations to fully 3D simulations. In the three-dimensional framework, the average vertical motion varies smoothly in time, with smaller amplitudes in comparison to the more chaotic quasi 2D regime. The constrained motion in the two-dimensional plane triggers the accumulation of energy, as displayed in the kinetic energy profiles in Figure 4.12, which consequently leads to the rapid variation of velocity in time. Analogous findings were also established in Van der Poel *et al.* (2013), where flows are consistently more turbulent in 2D, and converge at large Prandtl numbers.

To capture the dynamics associated with the transport of the magnetic field

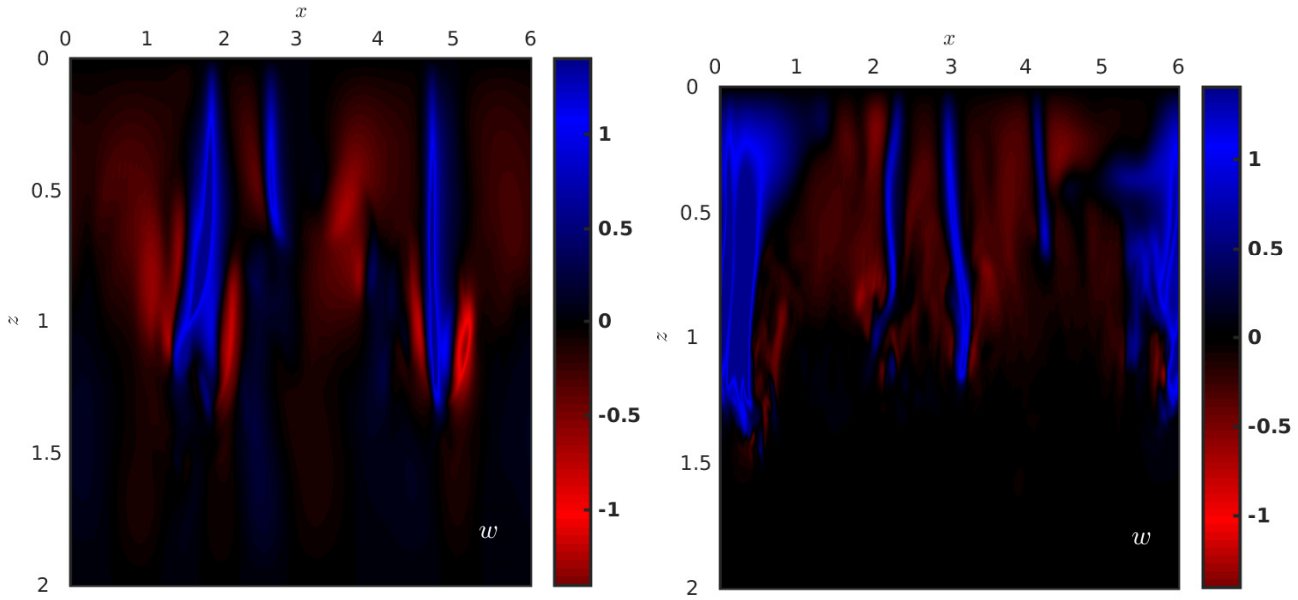

(a)

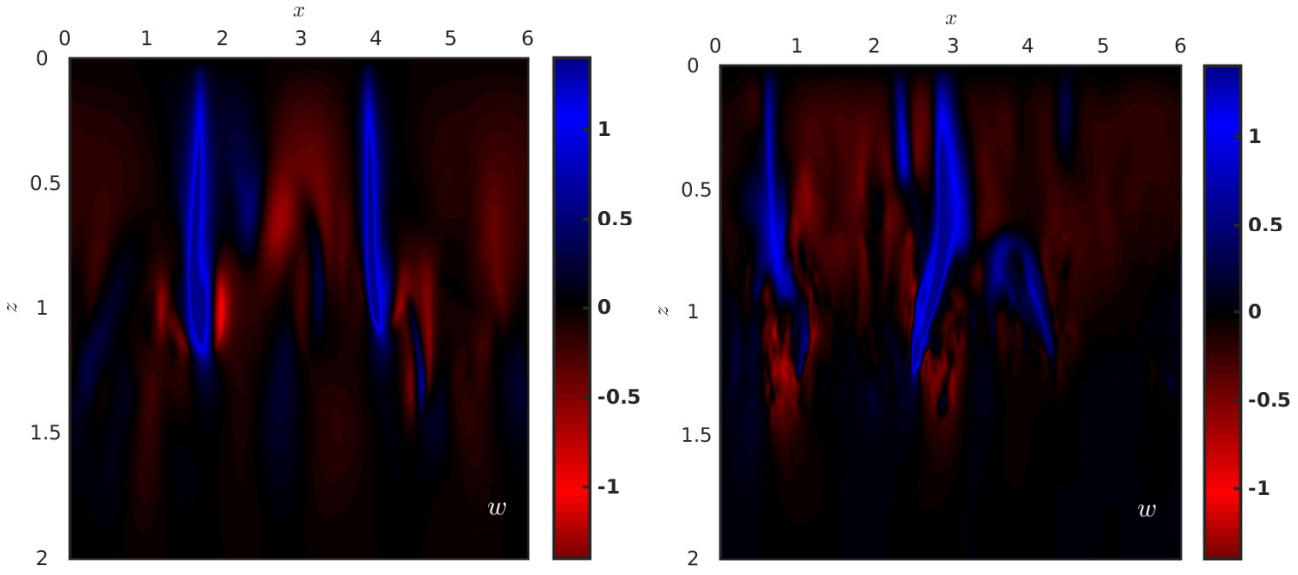

(b)

Figure 4.10: The vertical velocity field at computational times (a) $t \approx 26$ and (b) $t \approx 35$ for the case $\sigma = 0.1$ in two-dimensions (left) and three-dimensions (right).

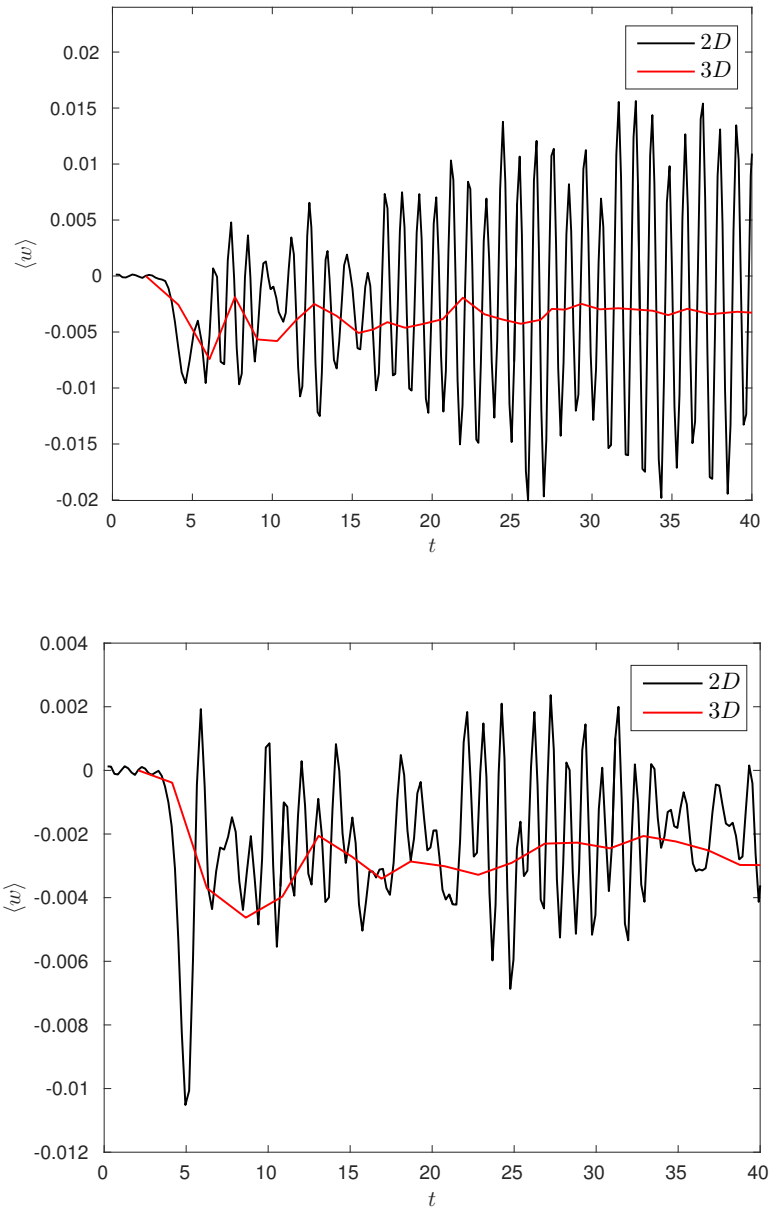

Figure 4.11: Temporal evolution of the average vertical velocity for $\sigma = 0.1$ (top panel) and $\sigma = 0.5$ (bottom panel) in two- and three-dimensions.

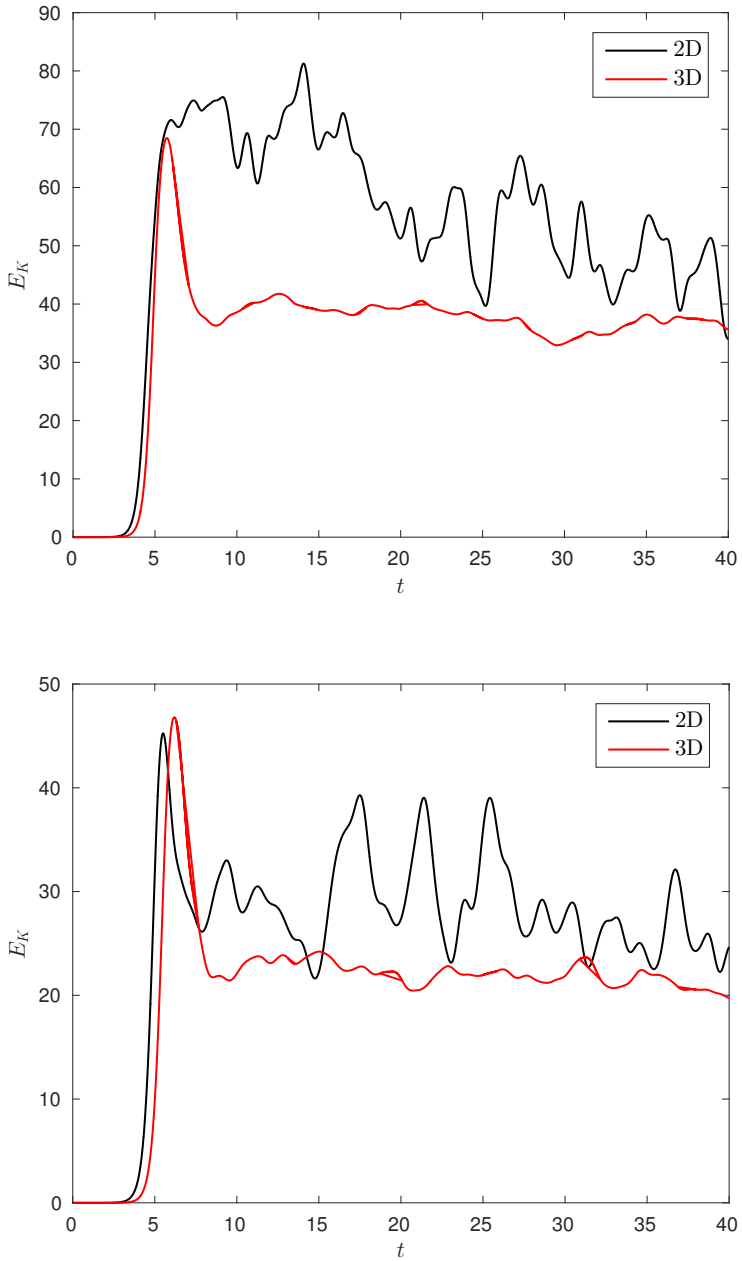

Figure 4.12: Temporal evolution of the total kinetic energy for $\sigma = 0.1$ (top panel) and $\sigma = 0.5$ (bottom panel) in two- and three-dimensions.

through the turbulent convecting region in three-dimensions, a horizontal magnetic layer is inserted at computational time $t \approx 42$, in the case where the Prandtl number $\sigma = 0.1$ and magnetic field strength $F = 0.01$. Snapshots of the 3D magnetoconvection interactions in Figure 4.13 generally reveal similar characteristics to that determined in two-dimensions (Figure 4.5). The effects of convection and turbulence can clearly be viewed in Figures 4.13(a)-4.13(k), where the buoyancy-driven magnetic field undergoes suppression and amplification as it competes with the overlying convective motion to escape.

Figure 4.14 highlights the equipartition-strength magnetic structures for the 3D simulation, by displaying snapshots of the vertical velocity, horizontal magnetic field, and ratio of kinetic energy to magnetic energy, at several computational times. The transport of the magnetic field through the convective layer is predominantly a result of advection. Magnetic structures of equipartition-strength occur at the interface region, and almost remain within the lower domain as the strength of the field is insufficient to overcome the relatively stronger, overlying convective downflows. Therefore, to rise further through the domain, magnetic structures must be transported by the convective upflows.

Focusing on the global distribution of the magnetic field, Figure 4.15 shows Φ and z_{max}, as defined in Equations (4.13) and (4.14) respectively, for $\sigma = 0.1$ and $\sigma = 0.5$. The magnetic field is found to behave differently, in comparison to the quasi 2D cases. Here, a smoother time evolution of the profiles Φ and z_{max} is noticed. This is expected, given the reduced turbulence as the additional dimension is introduced. For the least turbulent flow in 3D, $\sigma = 0.5$, a greater amount of magnetic field is present in the upper domain. This agrees with the pattern determined in the final stages of the quasi 2D evolution, where advection overtakes as the more active process in transporting the magnetic field, and so suggests that the degree of turbulence in the 3D cases is insufficient to highlight the contribution of equipartition-strength magnetic structures in

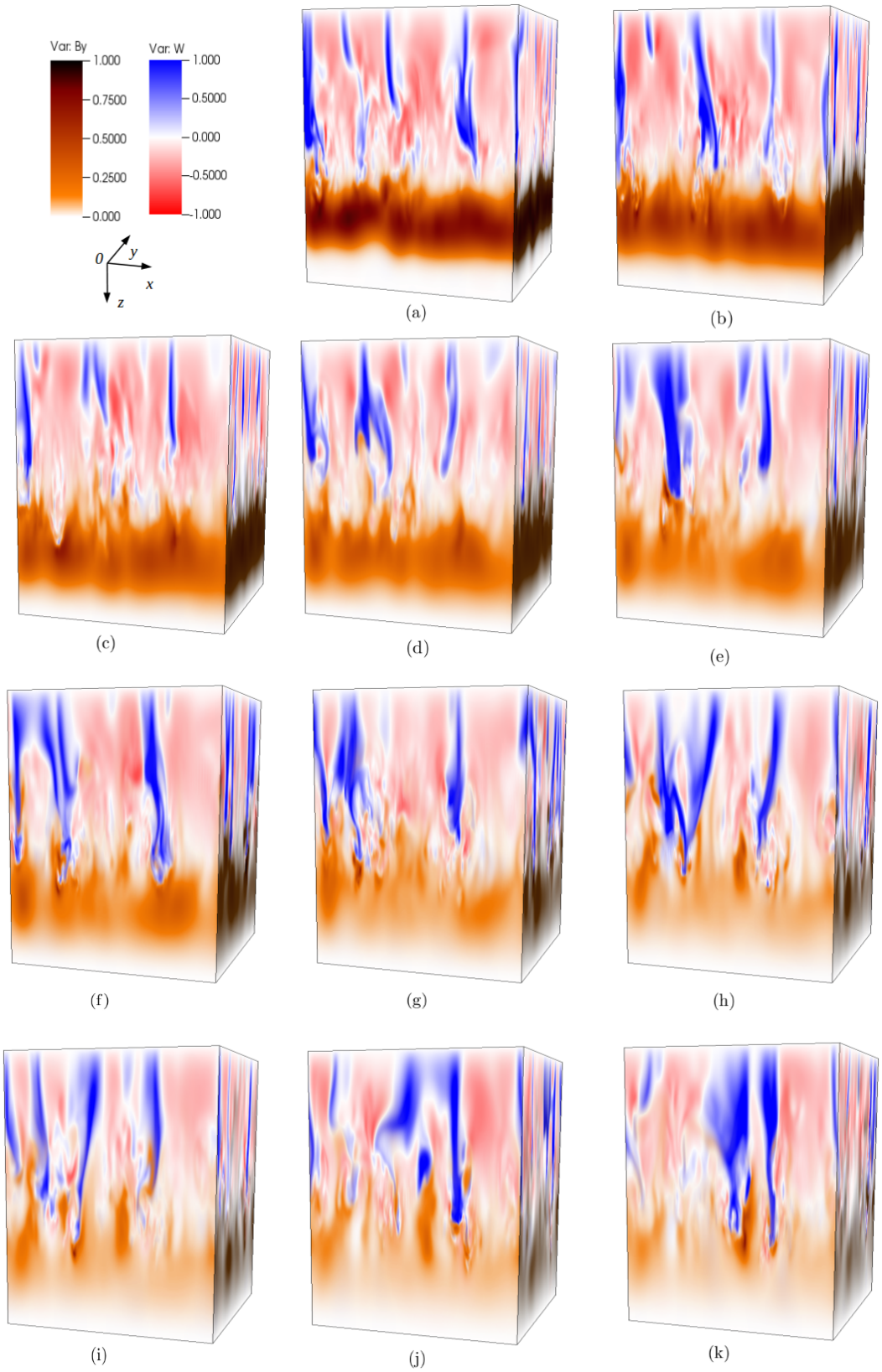

Figure 4.13: Snapshots of the z-component of the velocity field overlaid with the y-component of the magnetic field in three-dimensions at computational times (a) $t = 41.78$, (b) $t = 43.02$, (c) $t = 44.15$, (d) $t = 46.40$, (e) $t = 48.60$, (f) $t = 49.80$, (g) $t = 52.16$, (h) $t = 54.66$, (i) $t = 55.61$, (j) $t = 57.37$ and (k) $t = 58.69$ respectively.

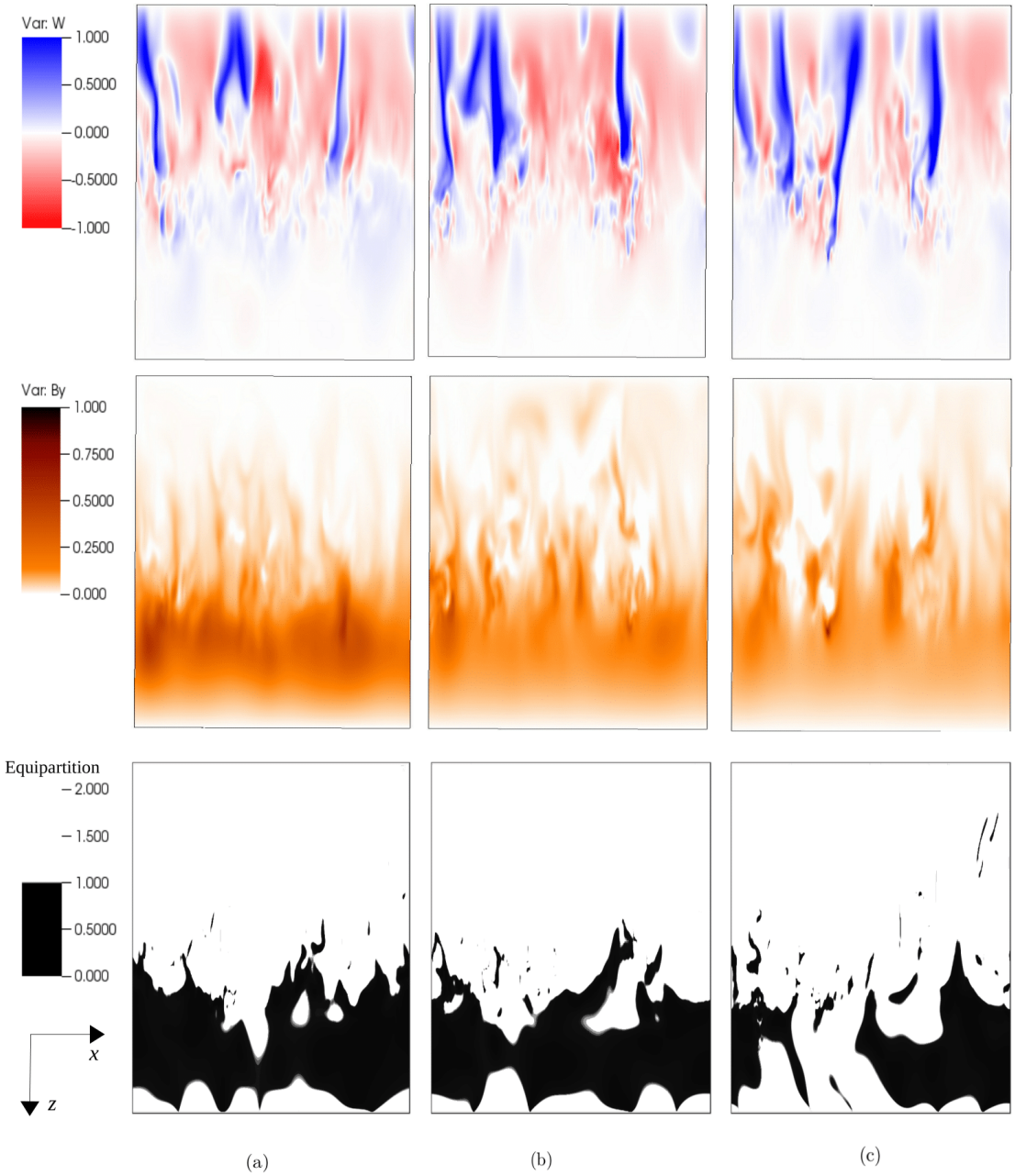

Figure 4.14: Snapshots of the z-component of the velocity field (top), the y-component of the magnetic field (middle) and ratio of the kinetic to magnetic energy (bottom) at $y = 0$ for times (a) $t = 45.3$, (b) $t = 50.9$, and (c) $t = 55.6$ respectively.

enhancing the rate of flux emergence.

The profile of z_{max} reveals similar features to the earlier quasi 2D findings; maximum field strength is maintained deeper for turbulent flows of greater velocity fluctuations, in this case $\sigma = 0.1$.

4.4 Conclusion

Starting from the fundamentals of MHD and the key equations governing the interactions between electrically conducting fluid and magnetic field, I adapted an idealised numerical model to explore the non-linear interaction between convective flows and buoyancy-driven magnetic structures, in a regime resembling the solar interior where the convection zone meets the tachocline, and address the nature of emergence of magnetic structures. Initially, prior to exploring the MHD model, various convective flows were established with respect to the non-dimensional Rayleigh number. The magnetic field was later introduced in a stably stratified region, positioned below the convectively unstable region once the hydrodynamic convection was fully developed, and the evolution of the magnetic field was investigated.

The quasi two-dimensional results, revealed two possibilities to explain the behaviour of the rising magnetic field. It was found that the magnetic field, while it is largely maintained in the vicinity where it was initially prescribed, can rise passively via convective motions, or alternatively strong magnetic structures, comparable to the surrounding motions, can rise without getting distracted by the overlying complexities of convection as was shown in Barker *et al.* (2012) and Chapter 3. Given the extreme conditions in the solar interior, the second possibility is most likely to occur. However, this equipartition phenomenon was complicated and difficult to solidly highlight due to the limitation of the simplified model.

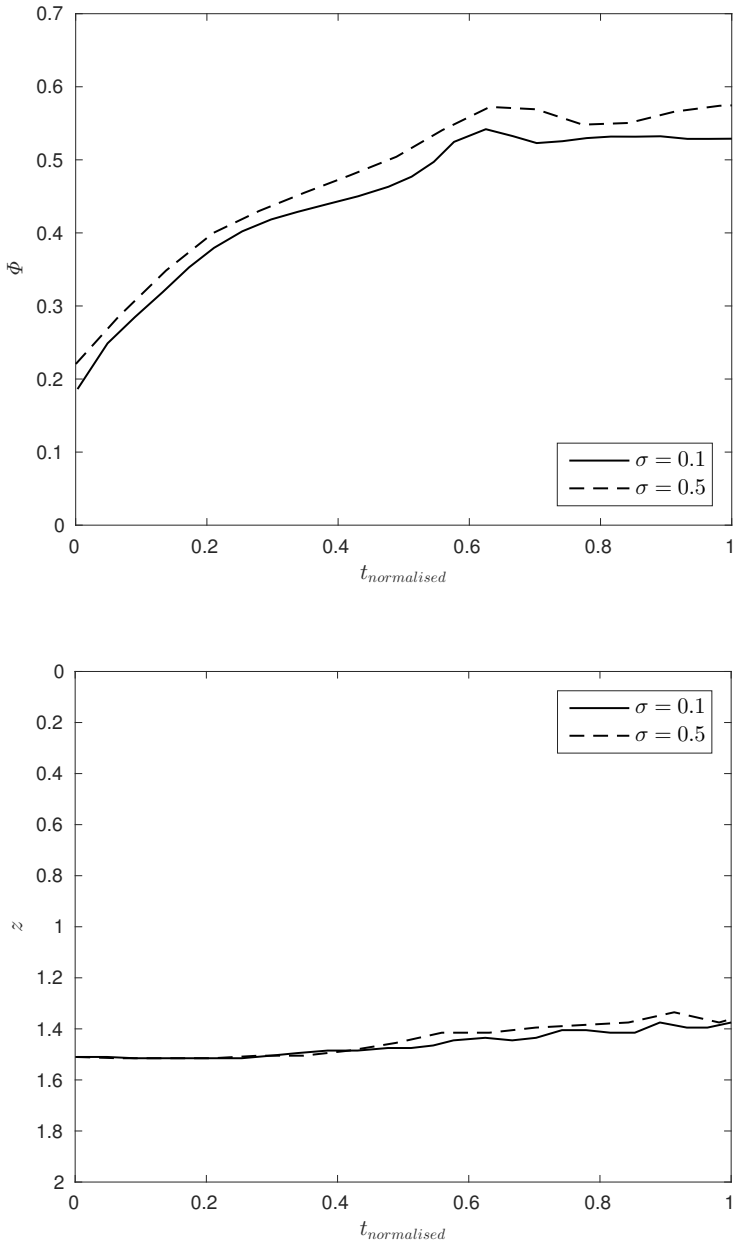

Figure 4.15: The temporal evolution of the magnetic flux fraction contained above the initial location of magnetic field, Φ, (top panel) and the location of the maximum magnetic field, z_{max} (bottom panel).

In the presented simulations, the transport of the field was mainly passive through the upper layer, but in the lower layer it was observed that small-scale, equipartition strength magnetic structures were reached. These magnetic structures were easily captured for larger values of F and were found to escape fractionally, however, they cannot rise unhindered given the inescapable, larger velocities present further through the upper region. Hence, the only possible way to escape completely is through the combination of both mechanisms.

The equipartition criterion of Barker *et al.* (2012) and Chapter 3 was found to appear on a local scale, and does contribute towards the global behaviour of the magnetic field, particularly as the flow becomes more turbulent. Greater fluctuations in the velocity field revealed an increased fraction of magnetic flux escaping through the convection zone. This is a result of the effective pumping and local amplification of the field due to turbulence, that enhances the emergence of equipartition-strength magnetic structures. However, the absence of mechanisms for generating magnetic fields led to a reduction in the magnetic field as time evolves. Consequently, the occurrence of equipartition-strength magnetic structures become less likely, and so advection overtakes as the primary source of field transport.

In this work, I also provided an insight into the magnetoconvection interactions in three-dimensions by conducting some of the quasi two-dimensional cases in three-dimensions. The additional degree of freedom was found to smoothen the variability and reduce the fluctuations of the velocity field. Therefore, unlike the quasi 2D simulations, equipartition-strength magnetic structures were not found to globally contribute toward the transport of magnetic field through the overlying convective layer. Results in quasi 2D highlight the findings of Barker *et al.* (2012) and Chapter 3, in terms of the effective role of turbulent pumping in transporting and maintaining the magnetic field. To capture similar dynamics to the quasi 2D calculations in 3D, further calculations of high-Rayleigh number turbulent convection must be investigated in 3D space.

It is important to note, however, due to the gap between numerical calculations and observations, our understanding of the Sun remains incomplete. The extreme conditions within the Sun cannot be retrieved in numerical simulations of convection, for instance. The desired Rayleigh number that portrays the property of convection in the solar interior cannot be simulated as the available computational capacity remains a major constraint to achieving the strong turbulence required. Therefore, the adaption of simplified models, such as the γ-pumping in Barker *et al.* (2012) and Chapter 3, might be a better approach to shed further light on the effect of turbulence in the solar convection zone.

Chapter 5

The Effect of Non-Constant Transport Coefficients on the Onset of Compressible Convection

5.1 Introduction

High-resolution observations of the solar surface are continually revealing a bewildering variety of multi-scale magnetic features (Harrison, 2008; Wiegelmann *et al.*, 2014), that are governed by the closely interacting magnetic fields and convectively-driven motions. With the purpose of exploring these structures and activities on the solar surface, an impressive number of studies have been conducted, and the role of the underlying convective processes are known to significantly contribute to the overall dynamics on the surface of the Sun (e.g. Galloway and Weiss, 1981; Cattaneo *et al.*, 2003).

Generally, convection plays a fundamental role in the many processes of stellar fluid dynamics (Weiss and Proctor, 2014; Kupka and Muthsam, 2017). In understanding convection in stellar interiors, extensive research over the past

several decades has been carried out to explore the onset of thermal convection (see, for example, Goody, 1956; Jones and Moore, 1978; Zappoli *et al.*, 2014). The onset of convection is based on the idea of a layer of fluid heated from below, which subsequently creates a vertical density variation resulting from the effects of thermal expansion and compression. As the thermal variation across the layer becomes larger, the fluid parcel becomes subject to an upward buoyancy force (see Section 2.1).

The seminal work of Rayleigh (1916) formed the foundation of convective instabilities, which has opened doors for further investigations over a wide range of physical phenomena. A comprehensive survey of the onset of thermal convection is given by Chandrasekhar (1961) using linear stability analysis, where a variety of features are examined, e.g. the effects of rotation and magnetic field.

Despite the great effort in exploring such complex systems, our understanding of the convective onset in different contexts is far from complete. The formalism of many of the early models introduced simplifying mathematical assumptions to reduce the complexity of the problem considerably, and allow employing analytical methods, in order to provide a preliminary exploration of the physical processes. Most studies of convective instability relied on the Boussinesq approximation, in which density variations are neglected in the governing equations, except when the gravitational force and buoyancy are considered (Boussinesq, 1903; Spiegel and Veronis, 1960).

In some astrophysical and geophysical systems, particularly the Sun, the inevitable large length scales result in substantial density variations through the deep convective layer. Therefore, the Boussinesq approach is an oversimplication to explore the many scale heights of solar convection. Accordingly, Spiegel (1965) constructed the linearised system for a fully compressible medium, to determine the onset of steady convection, and provide an insight into the non-linear evolution of compressible convection. Including compressibility was

found to reveal important effects on convection such as the occurrence of asymmetrical flows (Spiegel, 1965; Mizerski and Tobias, 2011).

It is essential to note that despite incorporating compressibility, constructed models involve some form of simplifying assumptions regarding the transport coefficients. The thermal conductivity and viscosity are usually approximated to be spatially uniform, and independent of the thermodynamic variables, to enable a more straightforward form of the equations describing the system, and reduce the computational effort when solved (see, for example, Ossendrijver *et al.*, 2001; Botha *et al.*, 2011; Bushby *et al.*, 2018). In some situations, it may be acceptable to consider such approximations, i.e. if the vertical extent of temperature is sufficiently small, but generally, the transport coefficients are not constant and depend on both the magnetic field and temperature (Priest, 1982; Spitzer, 2006).

Few attempts have been undertaken in order to understand the effect of non-constant transport coefficients in linear studies of convection, in a compressible atmosphere. Vickers (1971), for example, considered a position-dependent viscosity and a conductivity that was a function of temperature, while Graham and Moore (1978) included various forms of viscosity and conductivity. For a fully ionized plasma, both viscosity and thermal conductivity are dominantly proportional to $T^{5/2}$ (e.g. Priest, 1982; Spitzer, 2006). Thus, dependency will be important for calculations where there is a large temperature difference between the top and bottom of the domain, and there is the potential for complex local dynamics.

Appropriate non-constant transport coefficients, as outlined in Spitzer (2006), can significantly alter the stability threshold of a convecting fluid (Glatzmaier and Gilman, 1981; Drew *et al.*, 1995). This chapter will explore the effect of non-constant transport coefficients by deriving the hydrodynamic equations for marginal stability to incorporate the Spitzer relation, for the first time,

and use linear stability analysis to investigate the onset of instability of a fully compressible stratified system. This investigation will serve to understand the future magnetohydrodynamical problem, when magnetic fields are incorporated, and will inform subsequent fully non-linear calculations.

5.2 Model and Method

Prior to introducing the model, to study the linear stability of the desired system, it is convenient to briefly elaborate on the notion of stability. That is, the ability of a system in a state of equilibrium to adjust to disturbances. According to Żak (2013), the definition of an equilibrium state, i.e. the basic state of a system, is given as follows. *A vector $\boldsymbol{x}_e$ is called an equilibrium point for a system $\dot{\boldsymbol{x}}$ if once the state vector is equal to $\boldsymbol{x}_e$ it remains equal to $\boldsymbol{x}_e$ for all future times.*

The stability of a system is classified through perturbing the basic state, by adding small amplitude disturbances. If initial perturbations decay in time, then the system is called stable. Otherwise, a system is called unstable if the initial perturbations grow or persist. In a mathematical context, the notion of stability can be formalised based on the concept of Lyapunov stability for which *an equilibrium state $\boldsymbol{x}_e$ is stable if for any given $\epsilon > 0$ there exist $\delta > 0$ such that if $||\boldsymbol{x}(t=0) - \boldsymbol{x}_e(t=0)|| < \delta$ then $||\boldsymbol{x}(t) - \boldsymbol{x}_e(t)|| < \epsilon$ for all $t \geq 0$* (Lappa, 2009; Żak, 2013).

On this mathematical basis, linear stability analysis techniques can be applied to determine the conditional stability of a given system (Joseph, 1976; Lappa, 2009). By decomposing the various physical variables describing the system into background and infinitesimally small perturbation components, that is $f(\boldsymbol{x}, t) = f_e(\boldsymbol{x}) + \delta f(\boldsymbol{x}, t)$, linear equations governing the evolution of the disturbances can be derived, and therefore solved to examine the stability of the system.

5.2.1 Derivation of Linear Stability Equations

The system considered here consists of a three-dimensional domain in a Cartesian geometry, with the x and y coordinates representing the horizontal directions, and the z-axis pointing vertically down, parallel to the constant gravitational acceleration. In dimensional form, the set of equations for the evolution of a compressible hydrodynamic system, as outlined in Chapter 2, is:

$$\frac{\partial \rho}{\partial t} + \nabla \cdot (\rho \boldsymbol{u}) = 0, \tag{5.1}$$

$$\rho\left(\frac{\partial \boldsymbol{u}}{\partial t} + (\boldsymbol{u} \cdot \nabla)\boldsymbol{u}\right) = -\nabla p + \rho g \hat{\boldsymbol{z}} + \nabla \cdot (\mu \boldsymbol{\tau}), \tag{5.2}$$

$$\rho c_v\left(\frac{\partial T}{\partial t} + (\boldsymbol{u} \cdot \nabla)T\right) = -p\nabla \cdot \boldsymbol{u} + \nabla \cdot \big(K \nabla T\big) + \frac{\mu \tau^2}{2}, \tag{5.3}$$

where the perfect gas law

$$p = R_* \rho T, \tag{5.4}$$

(R_* is the gas constant) and the viscous stress tensor

$$\tau_{ij} = \frac{\partial u_i}{\partial x_j} + \frac{\partial u_j}{\partial x_i} - \frac{2}{3}\frac{\partial u_k}{\partial x_k}\delta_{ij}. \tag{5.5}$$

The transport coefficients K and μ are assumed to be functions of temperature, and take the following form:

$$K = K_0\left(\frac{T}{T_*}\right)^q, \tag{5.6}$$

$$\mu = \mu_0\left(\frac{T}{T_*}\right)^r, \tag{5.7}$$

where T_*, K_0, and μ_0 are the reference temperature, thermal conductivity, and viscosity respectively, taken to be the value at the top of the domain. The indices q and r are assumed constants that will be varied.

Let $\rho = \rho_0 + \rho'$, $T = T_0 + T'$, $\boldsymbol{u} = \boldsymbol{u}_0 + \boldsymbol{u}'$, and $p = p_0 + p'$, where ρ_0, T_0, $\boldsymbol{u}_0$, and p_0 are the static solutions of the governing equations and ρ', T', $\boldsymbol{u}'$, and p' are to have infinitesimal amplitudes. The static solutions are found by neglecting time-derivatives, and assuming a basic state where $\boldsymbol{u}_0 = \boldsymbol{0}$, $T = T_0(z)$, and $\rho = \rho_0(z)$. Hence, from the above equations, one obtains

$$\frac{dp_0}{dz} = g\rho_0, \tag{5.8}$$

$$K\frac{dT_0}{dz} = \text{constant}, \tag{5.9}$$

and

$$p_0 = R_*\rho_0 T_0. \tag{5.10}$$

The equations for the evolution of the perturbed quantities are derived by inserting the decomposed variables, adapting the basic state assumptions, and linearising. Therefore, starting with Equation (5.1):

$$\frac{\partial(\rho_0 + \rho')}{\partial t} + \nabla \cdot ((\rho_0 + \rho')(\boldsymbol{u}_0 + \boldsymbol{u}')) = 0,$$

and so,

$$\frac{\partial \rho'}{\partial t} + \nabla \cdot (\rho_0 \boldsymbol{u}') = \frac{\partial \rho'}{\partial t} + \rho_0 \nabla \cdot \boldsymbol{u}' + \boldsymbol{u}' \cdot \nabla \rho_0 = 0.$$

Note that ρ_0 is only a function of z, thus the above equation yields

$$\frac{\partial \rho'}{\partial t} + \rho_0 \nabla \cdot \boldsymbol{u}' + w' \frac{\partial \rho_0}{\partial z} = 0. \tag{5.11}$$

Next, considering Equation (5.2):

$$\rho \frac{\partial \boldsymbol{u}}{\partial t} + (\boldsymbol{u} \cdot \nabla)\boldsymbol{u} = -\nabla p + \rho g \hat{\boldsymbol{z}} + \frac{\mu_0}{T_*^r} \nabla \cdot (T^r \boldsymbol{\tau}). \tag{5.12}$$

Perturbing Equation (5.12) gives

$$\rho_0 \frac{\partial \boldsymbol{u}'}{\partial t} = -R_* \rho' \nabla T_0 - R_* \rho_0 \nabla T' - R_* T' \nabla \rho_0 - R_* T_0 \nabla \rho' + \rho' g \hat{\boldsymbol{z}} + \frac{\mu_0}{T_*^r} \nabla \cdot (T_0^r \boldsymbol{\tau}'), \tag{5.13}$$

where $\boldsymbol{\tau}'$ is the stress tensor for the perturbed component of the velocity.

For the temperature, Equation (5.3) becomes

$$\rho c_v \left(\frac{\partial T}{\partial t} + (\boldsymbol{u} \cdot \nabla) T \right) = -p \nabla \cdot \boldsymbol{u} + \frac{K_0}{T_*^q (q+1)} \nabla^2 (T^{q+1}) + \frac{\mu \tau^2}{2}, \tag{5.14}$$

and by perturbing, one obtains

$$\rho_0 c_v \frac{\partial T'}{\partial t} + \rho_0 c_v w' \frac{\partial T_0}{\partial z} = -R_* \rho_0 T_0 \nabla \cdot \boldsymbol{u}' + \frac{K_0}{T_*^q} \nabla^2 (T_0^q T'). \tag{5.15}$$

Note that the basic state condition for $\boldsymbol{u}$ means that there will be no contribution to the linear equation from the heating terms.

The non-dimensional form of Equations (5.11), (5.13), and (5.15) are given following an appropriate choice of scales. The unit of length is scaled by the depth of the layer, d. Density and temperature are scaled by their initial values at the upper surface, ρ_* and T_* respectively. Velocity is scaled by the sound travel time across the layer in terms of the isothermal sound speed, $\sqrt{R_* T_*}$, and is related to the unit of time $d/\sqrt{R_* T_*}$. Thus, for the mass equation (Equation 5.11) this gives

$$\frac{\partial \rho'}{\partial t} + \rho_0 \nabla \cdot \boldsymbol{u}' + w' \frac{\partial \rho_0}{\partial z} = 0. \tag{5.16}$$

The momentum equation (Equation 5.13) becomes

$$\rho_0 \frac{\partial \boldsymbol{u}'}{\partial t} = -\rho' \nabla T_0 - \rho_0 \nabla T' - T' \nabla \rho_0 - T_0 \nabla \rho' + \rho' \left. \frac{\mathrm{d} T_0}{\mathrm{d} z} \right|_* (m+1) \hat{\boldsymbol{z}} + \sigma C_k \nabla \cdot (T_0^r \boldsymbol{\tau}'), \tag{5.17}$$

where the polytropic index $m = -1 + g/R_*(dT_0/\mathrm{d}z)|_*$, the Prandtl number $\sigma = \mu_0 c_p/K_0$, and the dimensionless thermal diffusivity $C_k = K_0/\rho_* c_p d\sqrt{R_* T_*}$.

For the temperature equation (Equation 5.15), the non-dimensional form reads

$$\rho_0 \frac{\partial T'}{\partial t} + \rho_0 w' \frac{\partial T_0}{\partial z} = -(\gamma_s - 1)\rho_0 T_0 \nabla \cdot \boldsymbol{u}' + \gamma_s C_k \nabla^2 (T_0^q T'). \tag{5.18}$$

where $\gamma_s = c_p/c_v$ is the ratio of specific heats.

Given the depth-dependent equilibrium state, each perturbed quantity can be expressed through the typical normal-mode ansatz $f(z)\exp(ikx + ily + st)$, where $k, l \in \mathbb{R}$ are the horizontal wave numbers, $s = s_r + is_i \in \mathbb{C}$ with s_r being the growth rate of the instability, and f describes the variation of the disturbances across the layer (Tobias and Hughes, 2004; Favier *et al.*, 2012; Crouch, 2016). Henceforth, the equations that govern the development of small-amplitude perturbations can be cast in the following form:

$$s\rho' = -iku'\rho_0 - ilv'\rho_0 - D(w'\rho_0), \tag{5.19}$$

$$\begin{aligned} \rho_0 s u' = -\rho_0 ikT' - T_0 ik\rho' + \sigma C_k T_0^r \left(D^2 u' + \frac{1}{3} ikDw' - \frac{4}{3}k^2 u' - l^2 u' - \frac{1}{3} klv' \right) \\ + r\sigma C_k T_0^{r-1} DT_0 (Du' + ikw'), \end{aligned} \tag{5.20}$$

$$\begin{aligned} \rho_0 s v' = -\rho_0 ilT' - T_0 il\rho' + \sigma C_k T_0^r \left(D^2 v' + \frac{1}{3} ilDw' - \frac{4}{3}l^2 v' - k^2 v' - \frac{1}{3} klu' \right) \\ + r\sigma C_k T_0^{r-1} DT_0 (Dv' + ilw'), \end{aligned} \tag{5.21}$$

$$\rho_0 s w' = -D(T_0\rho') - D(\rho_0 T') + \rho' DT_0|_*(m+1) + \sigma C_k T_0^r \left(\frac{4}{3}D^2 w' + \frac{1}{3}ikDu' + \frac{1}{3}ilDv' - w'k^2 - w'l^2\right) + r\sigma C_k T_0^{r-1} DT_0 \left(\frac{4}{3}Dw' - \frac{2}{3}iku' - \frac{2}{3}ilv'\right), \tag{5.22}$$

$$\rho_0 s T' = -\rho_0 w' DT_0 - (\gamma_s - 1)\rho_0 T_0 (iku' + ilv' + Dw') + \gamma_s C_k (-k^2 - l^2 + D^2)(T_0^q T'), \tag{5.23}$$

To simplify the problem, it is possible to reduce the three-dimensional set of linearised equations to an equivalent two-dimensional problem, without losing information about the stability properties in the three-dimensional framework.

Squire's theorem (Squire, 1933; Drazin and Reid, 2004) states that *to each unstable three-dimensional disturbance there corresponds a more unstable two-dimensional one.* The proof of the theorem was formulated to transform an inviscid fluid; however, it can be applied to a viscous fluid, if a Squire's transformation is found. The coordinate transformation in this framework exists and is as follows: $\tilde{k} = \sqrt{k^2 + l^2}$, $\tilde{k}\tilde{u'} = ku' + lv'$, $\tilde{\rho_0} = \rho_0$, $\tilde{\rho'} = \rho'$, $\tilde{T_0} = T_0$, $\tilde{T'} = T'$, $\tilde{s} = s$, $\tilde{w'} = w'$, where tilde denotes two-dimensional quantities.

On substituting, and dropping the tildes, Equations (5.19)-(5.23) are reduced to an equivalent two-dimensional problem:

$$s\rho' = -iku'\rho_0 - D(w'\rho_0), \tag{5.24}$$

$$\rho_0 s u' = -\rho_0 ikT' - T_0 ik\rho' + \sigma C_k T_0^r \left(D^2 u' + \frac{1}{3} ikDw' - \frac{4}{3} k^2 u' \right) + r\sigma C_k T_0^{r-1} DT_0 (Du' + ikw'), \tag{5.25}$$

$$\rho_0 s w' = -D(T_0 \rho') - D(\rho_0 T') + \rho' DT_0|_*(m+1) + \sigma C_k T_0^r \left(\frac{4}{3} D^2 w' + \frac{1}{3} ikDu' - w' k^2 \right) + r\sigma C_k T_0^{r-1} DT_0 \left(\frac{4}{3} Dw' - \frac{2}{3} iku' \right), \tag{5.26}$$

$$\rho_0 s T' = -\rho_0 w' DT_0 - (\gamma_s - 1)\rho_0 T_0 (iku' + Dw') + \gamma_s C_k (-k^2 + D^2)(T_0^q T'), \tag{5.27}$$

which can be written in the form $s\boldsymbol{f} = A\boldsymbol{f}$, where the vector $\boldsymbol{f} = (\rho', u', w', T')$ is the solution vector containing the eigenfunctions, and A is a 4×4 matrix that consists of linear differential operators in z.

Equations (5.24)-(5.27) are solved numerically by dividing the layer depth $0 \leq z \leq d$ into n uniformly distributed points, and the differential operators are approximated using a central fourth-order finite-difference approximation (see Subsection 3.2.5). The method used in this model is adapted from the general method discussed in Favier *et al.* (2012) and Witzke *et al.* (2015), where the Schur factorisation is utilised to determine the eigenvalues and eigenvectors.

5.2.2 Boundary and Initial Conditions

To complete the description of the problem, impermeable, stress-free velocity, and constant temperature boundary conditions are employed on the top and

bottom boundaries:

$$\begin{gathered}\frac{\partial u'}{\partial z}=\frac{\partial v'}{\partial z}=w'=0 \qquad \text{at} \qquad z=0 \quad \text{and} \quad z=d, \\ T'=T_* \quad \text{at} \quad z=0 \quad \text{and} \quad T'=T_*(1+\theta) \quad \text{at} \quad z=d.\end{gathered} \tag{5.28}$$

At this stage, it is convenient to explicitly define the equilibrium temperature and density distributions. Starting with Equation (5.9):

$$K_0\left(\frac{T_0}{T_*}\right)^q\frac{\partial T_0}{\partial z}=A,$$

which implies that

$$T^q\frac{\partial T_0}{\partial z}=B.$$

Thus,

$$\frac{T_0^{q+1}}{q+1}=Bz+C,$$

and so

$$T_0=(Dz+E)^{\frac{1}{q+1}},$$

where A, B, C, D, E are all constants. Using boundary conditions $T(0)=T_*$ and $T(1)=1+\theta$, and non-dimensionalising gives

$$T=T_*\left[\left((1+\theta)^{q+1}-1\right)\frac{z}{d}+1\right]^{\frac{1}{q+1}}. \tag{5.29}$$

For density, starting from Equation (5.8):

$$R_*\frac{\partial(\rho_0 T_0)}{\partial z}=\rho_0 g.$$

Non-dimensionalising gives,

$$\frac{R_*\rho_* T_*}{d}\frac{\partial(\rho_0 T_0)}{\partial z}=\rho_*\rho_0 g,$$

and so,

$$\frac{R_* T_*}{d}\left(\rho_0\frac{\partial T_0}{\partial z}+T_0\frac{\partial \rho_0}{\partial z}\right)=\rho_0 g.$$

Using the definition of the polytropic index, the above equation becomes

$$T_0\frac{\partial\rho_0}{\partial z} = \rho_0\left(\frac{gd}{R_*T_*} - \frac{\partial T_0}{\partial z}\right) = \rho_0\left(\frac{R_*(dT_0/\mathrm{d}z)|_*(m+1)d}{R_*T_*} - \frac{\partial T_0}{\partial z}\right).$$

Thus,

$$\int\frac{1}{\rho_0}\partial\rho_0 = \frac{(m+1)\big((1+\theta)^{q+1}-1\big)}{q+1}\int\frac{1}{T_0}\partial z - \int\frac{\partial T_0/\partial z}{T_0}\partial z.$$

At this step, it is crucial to have knowledge of the value of q. Integrating the above equation, for non-zero q, gives

$$\ln\rho_0 = \frac{d(m+1)}{qT_*}\left[\big((1+\theta)^{q+1}-1\big)\frac{z}{d}+1\right]^{\frac{q}{q+1}} - \ln T_0 + F,$$

where F is a constant. Using conditions $\rho(0)=\rho_*$ and $T(0)=T_*$, one deduces

$$F = \ln(\rho_*T_*) - \frac{d(m+1)}{qT_*}.$$

Therefore,

$$\ln\left(\frac{\rho_0T_0}{\rho_*T_*}\right) = \frac{d(m+1)}{qT_*}\left[\left(\big((1+\theta)^{q+1}-1\big)\frac{z}{d}+1\right)^{\frac{q}{q+1}}-1\right],$$

and finally,

$$\rho_0 = \rho_*\left(\big((1+\theta)^{q+1}-1\big)\frac{z}{d}+1\right)^{-\frac{1}{q+1}}\exp\left\{\frac{d(m+1)}{qT_*}\left[\left(\big((1+\theta)^{q+1}-1\big)\frac{z}{d}+1\right)^{\frac{q}{q+1}}-1\right]\right\}. \tag{5.30}$$

The background state of density and temperature varies depending on the values of q and is unaffected by r since viscosity, in this case, does not modify the basic state. Figure 5.1 highlights the differences in the initial temperature and density profiles for several q values. The temperature at the top and bottom of the domain is held fixed for all q, as imposed by the boundary conditions

(Equation 5.28). However, as q increases, the temperature gradient continually changes with depth (see Figure 5.2), and the temperature distribution is no longer linear. Interestingly, the density distribution is found to increase exponentially, as the value of q grows, introducing high density contrasts across depth.

5.2.3 Parameter Choices

For this preliminary investigation, the principal objective is to understand the general influence of non-constant transport coefficients on stability. Therefore, the parameters that characterise the system do not necessarily provide direct insight into the dynamics of the Sun. I choose to present the survey of critical values of instability by fixing the thermal stratification, θ, and the Prandtl number, σ, to unity in all cases while the variable parameters are the polytropic index, m, thermal conductivity index, q, and viscosity index, r.

It is known that for a monoatomic ideal gas, where the specific heat ratio of $\gamma_s = 5/3$ is employed, the polytrope is stable for $m \geq 1.5$. In this case, I fix $m < 1.5$ and accordingly analyse the effect of varying polytropic index on the instability of the system. A summary of the input parameters is shown in Table 5.1. The resolution of this problem has been carefully selected and tested for the results quoted in this work. Note that, owing to the large density con-

Parameter	Description	Value
σ	Prandtl number	1.0
C_k	Thermal diffusivity	Variable
θ	Thermal stratification	1.0
γ_s	Ratio of specific heats	5/3
m	Polytropic index	Variable
q	Thermal conductivity index	Variable
r	Viscosity index	Variable
d	Vertical depth of layer	1.0

Table 5.1: The choice of parameters for the linear stability model.

trast as q increases, the choices of q are limited. For example, for $q = 2.5$, the

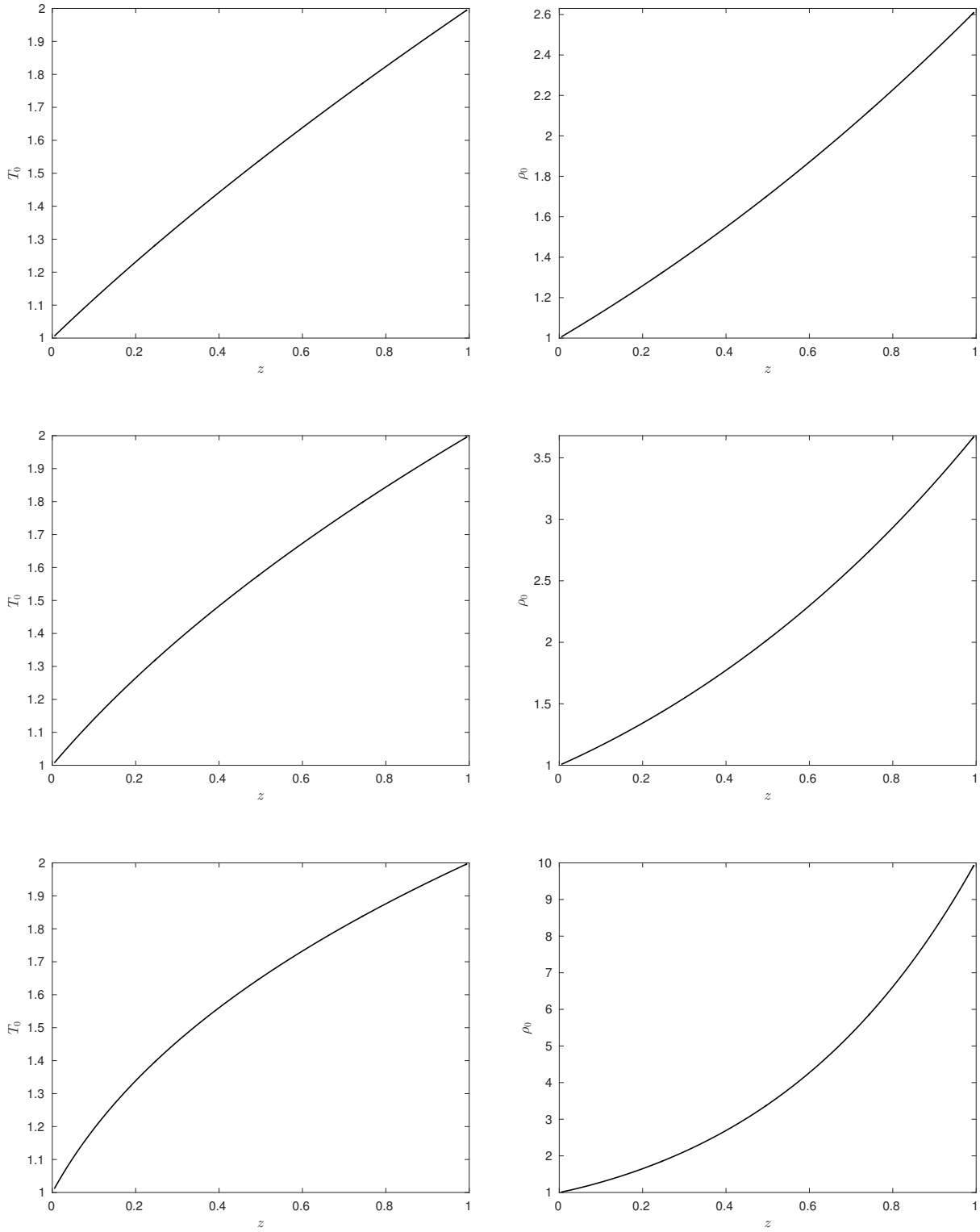

Figure 5.1: The background thermal profile (left) and density profile (right) for $q = 0.5$ (top panel), $q = 1$ (middle panel), and $q = 2$ (bottom panel), where $T_* = \rho_* = d = m = \theta = 1$.

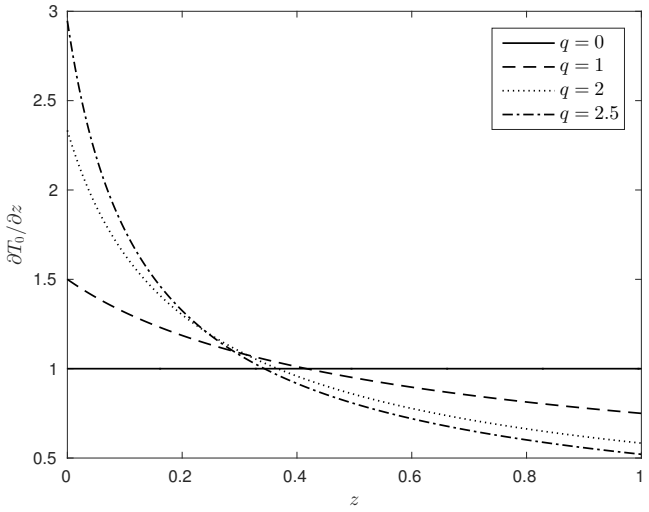

Figure 5.2: The temperature gradient profile for different values of the thermal conductivity index, q, where $T_* = d = \theta = 1$.

system remains under-resolved as it requires more points than computational resources allow.

5.3 Results

Here attention is focused on the stability threshold of the pure hydrodynamical system, while the characteristics of the transport coefficients are varied. The complete Equations (5.24)-(5.27) are solved numerically for a range of wave numbers, with stability threshold solutions discussed in terms of the critical Rayleigh number, in addition to the thermal diffusivity, for varying polytropic index, thermal conductivity index, and viscosity index. By setting the transport coefficients' indices to zero, one falls in the common framework of constant thermal conductivity and viscosity. Therefore, the presented results can partially be compared to Gough *et al.* (1976).

In keeping with the standard derivation of the non-dimensional Rayleigh number, the governing parameter for thermal convection (see Section 2.1 for details), the definition of Vickers (1971) for which the framework was built on

the foundation of similar assumptions to this model is given by

$$Ra = \frac{(\mathrm{d}T_1/\mathrm{d}z)\rho_1^2 g c_p d^4}{T_1 K_1 \mu_1}, \tag{5.31}$$

where subscript 1 refers to the value of the variable evaluated at an arbitrary level within the layer. Note that, the definition of the Rayleigh number in Equation (5.31) differs slightly from Spiegel (1965), where constant transport coefficients are considered. However, to enable direct comparisons between constant and non-constant transport coefficients, through varying q and r, the definition of the Rayleigh number in this model (Equation 5.31) is modified to allow the factor

$$1 - \frac{g}{(\mathrm{d}T_1/\mathrm{d}z)c_p} = \frac{3-2m}{5}, \tag{5.32}$$

as in Speigel's definition of the Rayleigh number. As illustrated in Figure 5.3, the depth-dependent Rayleigh number is highly variable and so, the common convention of expressing Ra in terms of the mid-layer value is followed (Brandenburg *et al.*, 1990; Hurlburt *et al.*, 1994).

To determine the critical Rayleigh number, Ra_c, the eigenvalue problem is solved, such that the most unstable mode is found for each parameter regime. The system is assumed to be stable if the growth rate, s, is zero for all wave numbers, k. Tables 5.2 and 5.3 summarise the results of the numerical simulations. For each fixed m, the critical Rayleigh numbers are found and presented in Table 5.2 for varying q and fixed $r = 0$, and in Table 5.3 for varying r and fixed $q = 0$, such that for $Ra > Ra_c$ convection will ensue. As values of Ra become larger than Ra_c, the band of wave numbers k, in which perturbation grows, expand. It can be noted that the system initiates close to the Boussinesq limit for stability of $Ra_c = 27\pi^4/7$, since the density variation is minimal for small m, q, and r. This signifies the good agreement between the compressible and Boussinesq calculations when density variations are small. As expected, the compressible flow is generally more stable as the polytropic index reaches the adiabatic value of $m = 1.5$.

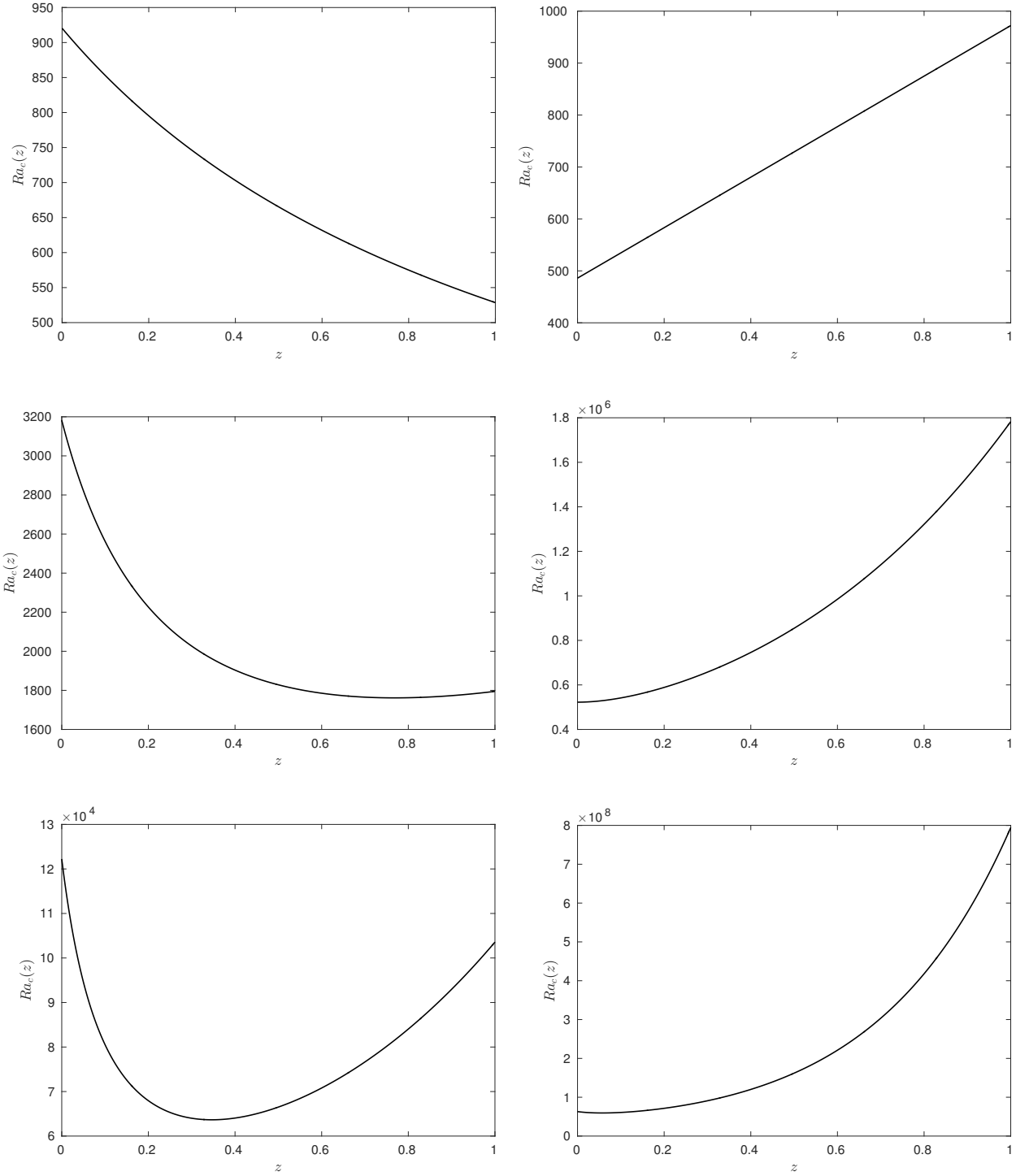

Figure 5.3: Graphs of the critical Rayleigh number as a function of depth for polytropic indices $m = 0.1$ (left panel) and $m = 1$ (right panel), and thermal conductivity indices $q = 0$ (top panel), $q = 1$ (middle panel), and $q = 2$ (bottom panel).

	Ra_c				
q	$m = 0.1$	$m = 0.25$	$m = 0.5$	$m = 1.0$	$m = 1.3$
0	664.90	674.79	690.30	728.40	747.56
0.001	665.22	674.65	691.20	729.00	751.56
0.01	669.31	679.45	697.60	744.20	789.82
0.1	712.77	731.00	770.00	916.80	1554.72
0.5	994.67	1086.25	1347.20	12350.20	1884433.52
1.0	1828.40	2429.00	6980.80	854356.80	97909022.64
1.5	6166.16	20463.50	140300.80	14391648.84	*
2.0	66514.00	207128.00	1466010.40	162759215.00	*
2.5	518030.24	1704571.50	12956050.00	*	*

Table 5.2: The critical Rayleigh number, Ra_c, for a range of q and m, for fixed $r = 0$. Values presented here are rounded to two decimal places. The asterisk (*) represents unachieved values due to the insufficient resolution available for these cases.

	Ra_c				
r	$m = 0.1$	$m = 0.25$	$m = 0.5$	$m = 1.0$	$m = 1.3$
0	664.90	674.79	690.30	728.40	747.56
0.001	664.93	674.79	690.86	728.43	748.25
0.01	666.80	676.27	692.74	728.43	750.32
0.1	690.30	700.01	718.38	750.76	773.72
0.5	795.57	806.14	823.66	862.84	888.91
1.0	958.10	969.72	991.47	1033.04	1060.16
1.5	1160.48	1172.75	1195.79	1241.93	1272.86
2.0	1421.55	1428.60	1451.70	1502.70	1535.72
2.5	1739.67	1749.28	1774.14	1829.30	1864.62

Table 5.3: The critical Rayleigh number, Ra_c, for a range of r and m, for fixed $q = 0$. Values presented here are rounded to two decimal places.

Of interest in this chapter is to discover how Ra_c behaves with varying q and r. The quantitative indication of the results reveals the stabilisation of the compressible medium as both q reaches the Spitzer limit ($q = 2.5$) in Table 5.2, and r reaches the Spitzer limit ($r = 2.5$) in Table 5.3. However, stabilisation is more effective for increasing q. This remark mainly lies in the effect of the large density stratifications. In other words, the substantial growth in Ra is primarily due to the exponential, depth-varying background density profile, that is incorporated in the definition of the Rayleigh number. This is in agreement with the results of Gough *et al.* (1976) and Calkins *et al.* (2014), where increasing stratification was found to lead to a growth in the critical Rayleigh number.

The plots in Figure 5.4 illustrates how variations in q (for fixed r) and r (for fixed q) influence the marginal stability for convection in terms of the thermal diffusivity, C_k, for a range of polytropic indices, m. By employing a logarithmic scale, a monotonic decrease in C_k is noticed with increasing q. The onset of C_k becomes significantly smaller as q grows, which escalates the critical Rayleigh values (as shown in Table 5.2) and delays the onset of convective instability. As mentioned earlier, at this stage it was found challenging to pin down the onset of convection for large values of q and m.

With varying viscosity in terms of r, an almost linear decay in the thermal diffusivity was found in Figure 5.4. Similar behaviour in the rate of decay was noticed for different values of the polytropic index. Intriguingly, a criticality was found around $m \approx 0.7$, where for smaller values of the polytropic index the thermal diffusivity threshold for convective instability proves to be higher. This criticality was also observed for varying thermal conductivity when $q \lesssim 0.5$. The thermal diffusivity transition, with respect to the polytropic index, cannot be extracted directly from Tables 5.2 and 5.3, given the definition of the Rayleigh number. This is because both the reduction of C_k

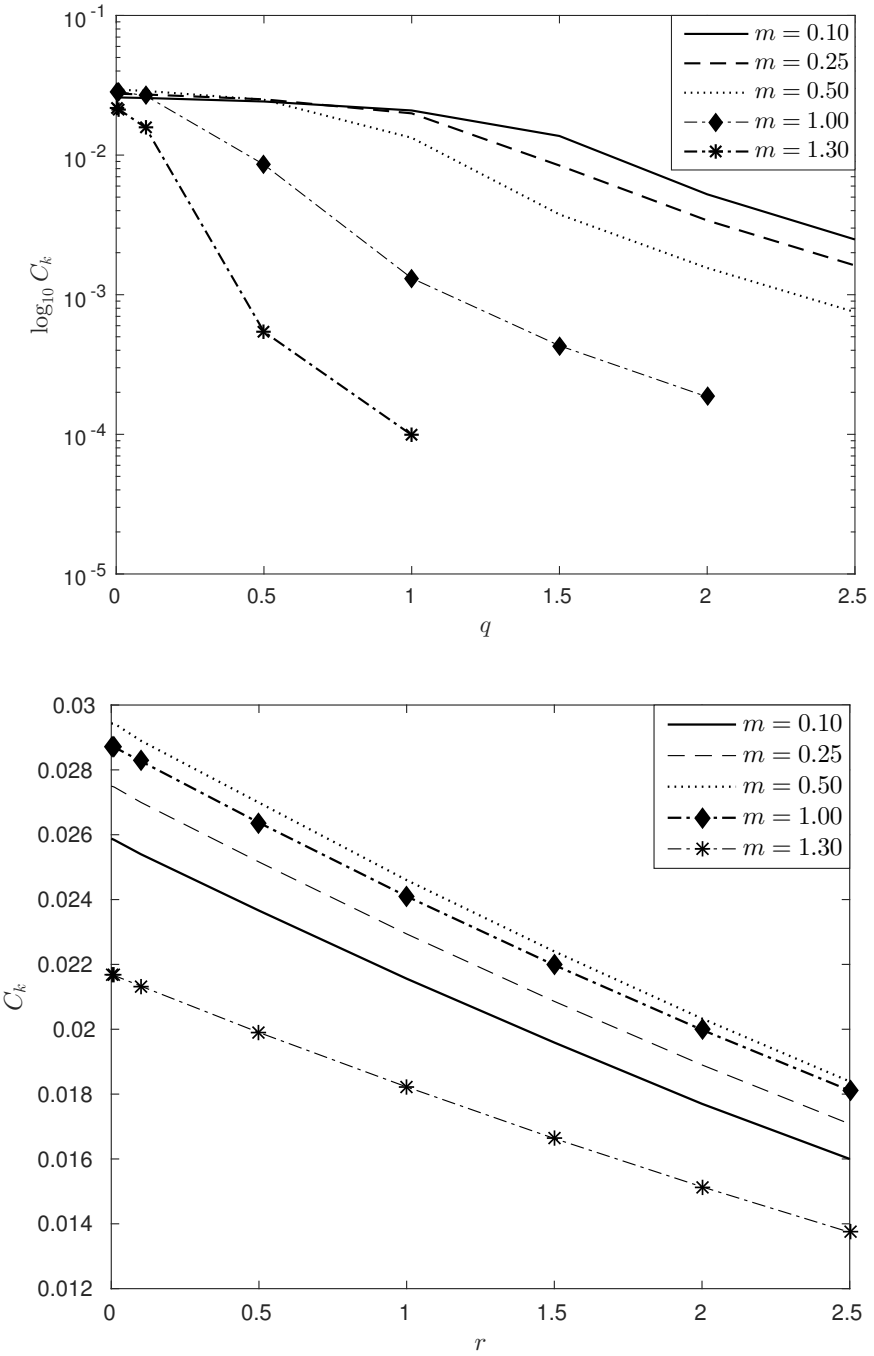

Figure 5.4: Onset of instability expressed in terms of the thermal diffusivity, C_k, for varying q and fixed $r = 0$ (top panel) and for varying r and fixed $q = 0$ (bottom panel).

and the increase of the polytropic index promotes system stability, i.e. the growth of the dimensionless Rayleigh number.

Vertical profiles of the marginal eigenfunctions for the vertical velocity, temperature, and density are shown in Figure 5.5, to provide a better insight into the local dynamical properties. The eigenfunctions displayed in this figure are for two values of the polytropic index, $m = 0.1$ and $m = 1$, for different values of q. In the constant transport coefficient regime, where $q = 0$, the shape of the temperature eigenfunctions can be seen to be parabolic in nature with a symmetry around $z = 0.5$ for both $m = 0.1$ and $m = 1$. However, by increasing q, changes in the general form of the eigenfunctions are revealed. The symmetry of the eigenfunctions breaks and becomes skewed towards the upper boundary. This can be explained as follows, the temperature gradient (Figure 5.2) as q increases becomes steeper near the top of the layer, therefore is prone to convective instability, and produces this deviation in the eigenfunctions. Generally, growth in temperature produces a decline in density, which consequently causes fluid motion due to pressure and other forces when differences in density occur under the influence of gravity (Böhm-Vitense, 1992; Subramanian and Balasubramaniam, 2001). This pattern can be seen in both eigenfunctions of density and velocity, where the peak height increases with increasing q.

By comparing the eigenfunctions for $m = 0.1$ and $m = 1$ in Figure 5.5, one inspects that the skewness to the top boundary is faster with sharper peaks for large m. Further, the eigenfunctions vanish at the bottom, and the onset of convection takes place at a sublayer near the upper domain. This returns to the nature of the background density, where the system is less dense at the upper boundary (as imposed by the boundary conditions) and buoyancy force is driving the motion. As the fluid becomes more stratified along with depth, buoyancy braking overtakes as the dominant mechanism driving the flow, and so leads to enhanced stability. Massaguer and Zahn (1980) and

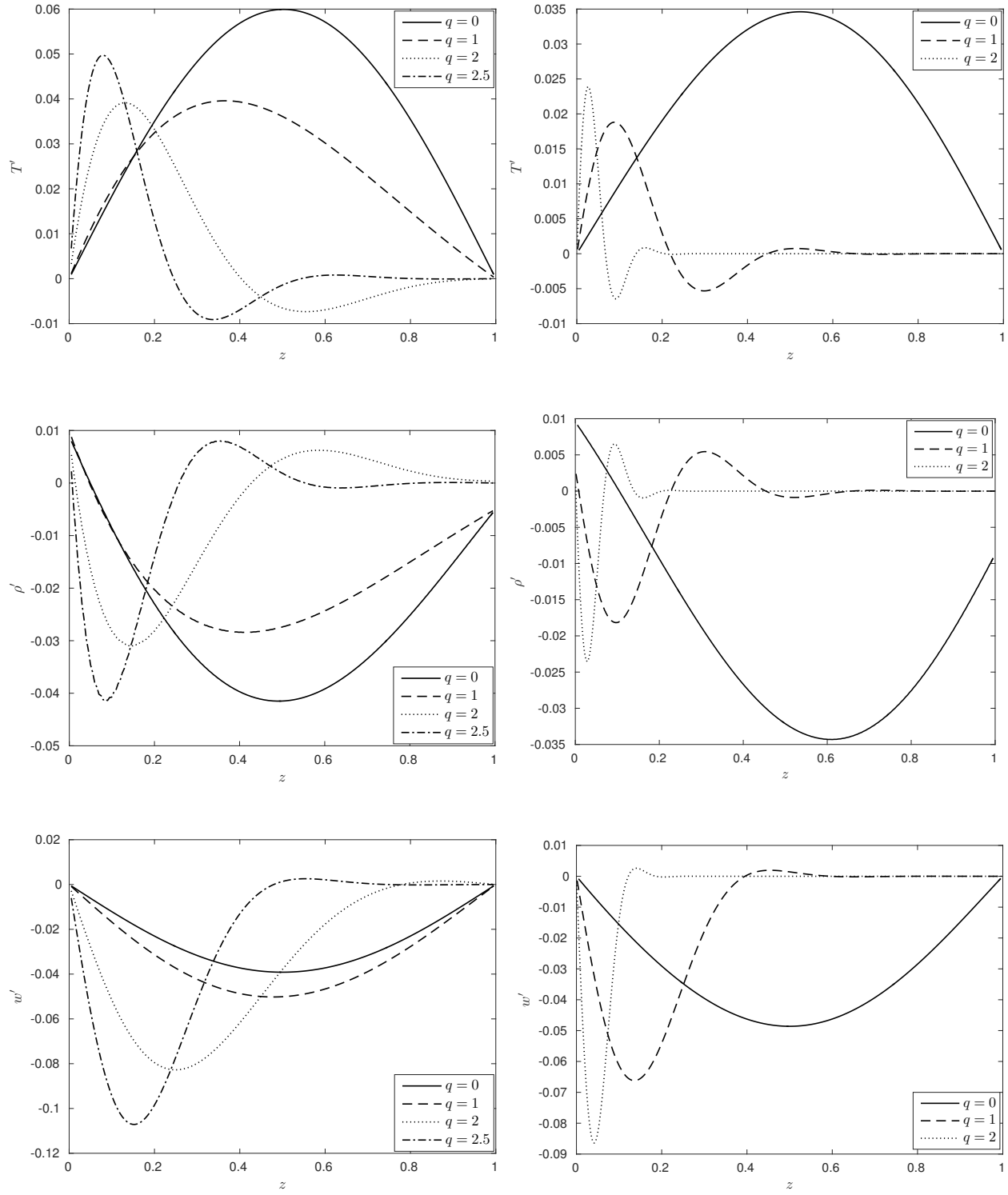

Figure 5.5: Eigenfunctions of the perturbed temperature field (top panel), density (middle panel), and vertical velocity (bottom panel) for polytropic indices $m = 0.1$ (left) and $m = 1$ (right), for several q values.

Hurlburt (1983) have indeed reported that buoyancy braking is responsible for the enhancing effect of stabilisation in layers with large density.

The perturbed temperature, density, and vertical velocity eigenfunctions for constant and temperature-dependent viscosities, as specified by r, are similarly depicted in Figure 5.6. The distributions are exact for both $r = 0$ (Figure 5.6) and $q = 0$ (Figure 5.5), given both transport coefficients are assumed constant. However, a different behaviour emerges in the eigenfunctions as r is varied. The symmetry is largely maintained with increasing r and is mildly skewed towards the upper layer. This is mainly because the basic state remains unchanged for varying r, as opposed to varying q. The eigenfunctions at onset indicate that the temperature-dependence of viscosity enhances the temperature perturbation about the midpoint of the layer, which accordingly attenuates density. However, as the viscosity proportionality with temperature increases, the effect on convective instability becomes evident. The vertical velocity reveals that increasing r is to inhibit the fluid flow, and hence, its effect is to delay the onset of convection. For increasing m, a qualitatively comparable behaviour is observed, with the addition of the enhanced impact of stabilisation due to density stratification.

5.4 Conclusion

With the ultimate objective of closely computing the intricate dynamics within the Sun, this chapter addressed a crucial issue regarding the simplifying assumptions in the mathematical modelling of MHD problems. The form of the transport coefficients, such as the dynamic viscosity and thermal conductivity, are often simplified to a constant value in space. To explore the impact of non-constant transport coefficients in the modelling of convective instabilities, a general form of the equations governing thermal convection in a compressible polytropic atmosphere, using the Spitzer relations for temperature-varying thermal conductivity and viscosity, were derived for the first time, and the sta-

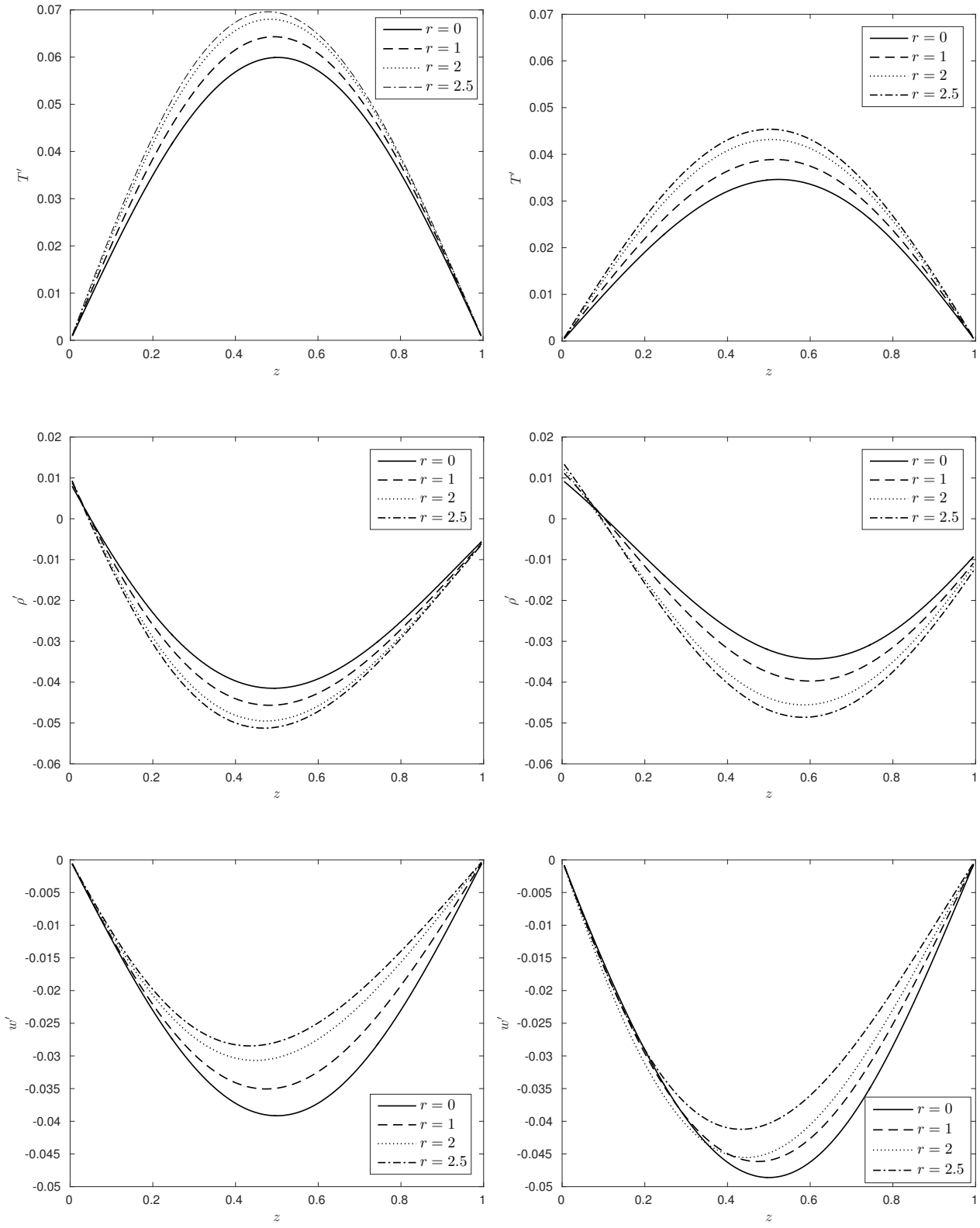

Figure 5.6: Eigenfunctions of the perturbed temperature field (top panel), density (middle panel), and vertical velocity (bottom panel) for polytropic indices $m = 0.1$ (left) and $m = 1$ (right), for several r values.

bility of the system was examined using linear stability analysis for each non-constant transport coefficient separately. The linear equations were solved numerically to determine the nature of the unstable modes, together with the structure of the eigenfunctions.

This investigation, though far from being comprehensive, provides an insight into the complexity introduced by non-constant transport coefficients. Here, I chose to initially present the conditions for instability, and not focus upon the growth rate of individual modes. The occurrence of convective instability was analysed by using the dimensionless Rayleigh number, and the thermal diffusivity, for several values of the polytropic index m, thermal conductivity index q, and viscosity index r. Accordingly, a range of critical parameters that determined the loss of stability was established. In all cases, the calculated values of the critical Rayleigh number for marginal stability was found to be consistently higher as the indices q and r increased. For large q, the onset of convection required huge computational efforts, which restricted the survey of analysis. Nevertheless, given that the structure of the static atmosphere was to a large extent determined by q, increasing q was found to produce large density stratifications, which led to delaying the onset of convection significantly.

For fluids with high viscosity, resulting from increasing the parameter r, the stabilising effect was found to be weaker, in comparison to varying q. This is presumably due to the small changes in the distribution of the basic temperature and density profiles, as r was varied. The polytropic index in all the cases investigated in this study was shown to stabilise the system as it reached the adiabatic limit. An interesting result is the criticality identified around $m = 0.7$, where higher values of the thermal diffusivity were determined at the onset of instability for smaller values of m. While the cause of this phenomenon remains unclear in this study, I aim to embark on this feature in future investigations.

The general behaviour of the eigenfunctions for the temperature-dependent transport coefficients revealed a far more interesting impact on the convecting fluid. This reinforces the notion that the choice of transport coefficients can have a great influence on the overall dynamics of convection, and thus should be carefully selected to investigate different convective atmospheres. Given that this study is a preliminary step to understand convective instability, it must be kept in mind that many other potential instabilities could contribute to the overall instability. In the Sun, for instance, instabilities can be driven by differential rotation and magnetic fields (see, for example, Tobias, 2005).

Ultimately, our interest lies in the rich behaviour that is expected to emerge in the fully non-linear development of instability. Prior to undertaking full non-linear calculations of convection regimes, it is important to understand the combined effect of non-constant viscosity and thermal conductivity, by means of linear stability analysis. Besides, I also aim to assess the influence of varying the Prandtl number on the onset of convection. Furthermore, it is necessary to consider the full magnetohydrodynamic problem, by incorporating the effect of the temperature-dependent magnetic diffusivity, that is $\eta \sim T^{3/2}$ (Schmidt, 1966; Spitzer, 2006), to further understand the interaction between magnetic fields and thermal convection, and to explain complex regions within stars, such as sunspots on the surface of the Sun.

Chapter 6

Discussion and Future Prospects

In this thesis, a number of results has been obtained. Here I shall provide a summary of the important findings, and discuss their implications for our present understanding of the interaction between convection and magnetic fields in the solar interior, particularly in the tachocline region. I also shall discuss some avenues for future research.

The transport of magnetic structures in the Sun is a complex phenomenon that is not well understood. As a step in the direction of tackling such a problem, this thesis focused on plausible mechanisms that drive magnetic structures throughout the solar convection zone. It is unquestionable that convection plays an essential role in the magnetic emergence process. In the first study (Chapter 3), I chose to demonstrate the competition between magnetic buoyancy and turbulent convection using the mean-field approximation in a numerical set-up that resembles the base of the solar convection zone, where the three-dimensional, fully compressible, non-linear magnetohydrodynamics equations were solved.

Describing the effect of small-scale turbulence on the large-scale magnetic field in a parameterised manner enabled us to filter out important information regarding the efficiency of magnetic field transport. The interactions of the net downward, time-dependent, γ-pumping overlying an imposed layer of magnetic

fluid revealed that equipartition of energy, between the magnetic and kinetic components, must be reached for buoyancy-driven magnetic structures to rise into the pumping region. The temporal variation of the γ-pumping was shown to significantly affect the evolution and other features of the emerging magnetic flux structures. The rate of emerging structures, the strength of magnetic concentrations, and the extent to how far magnetic field can travel were all found to depend on the timescale of the γ-pumping.

These findings shed new light on the timescale of convective turbulence and its influential role on the transport of magnetic fields. Depending on the timescale of the γ-pumping, magnetic structures were shown to concentrate and disperse accordingly. Frequent rise of weak magnetic structures was linked to highly-variable turbulent pumping profiles in time, while relatively infrequent emergence of stronger magnetic concentrations was found for turbulent pumping profiles that varied at a slower rate in time.

The presented results are encouraging in that they highlight the properties of magnetic structures that are distributed over granulation scales on the photospheric region of the Sun. The emergence rate and strength of magnetic fields link to the timescales and velocities associated with the solar surface convection (see, for example, Priest, 2014). However, it is necessary to realise that the solutions were obtained from a highly-simplified model, where several assumptions and limitations have been imposed, such as the parameterisation of turbulent pumping, and therefore is considered very simple to directly capture solar observations.

To bring the identified features of the simplified γ-pumping model a step closer to solar interior conditions, Chapter 4 incorporated fully-developed convection in the system to achieve the mean pumping imposed in Chapter 3 naturally. Additionally, a two-layer configuration was adapted to resemble the interface region embedded between the radiation zone and the convection zone inside

the Sun. This approach, as expected, brought some additional difficulties to extract information on the magnetoconvection interactions. Notably, the equipartition criterion was found challenging to clearly identify, due to the turbulent nature of convection.

The numerical simulations were performed in both quasi two-dimensional and fully three-dimensional geometries. The analysis of several magnetoconvection regimes revealed that the equipartition criterion does contribute globally in the flux emergence process as fluctuating motions in turbulent flows become more energetic. The results were found to be less pronounced in the three-dimensional simulations due to the effectively reduced fluctuations as an additional dimension was introduced into the model.

In Chapter 5, I addressed an important issue regarding the assumptions involved in the governing magnetohydrodynamics equations that determine the dynamics of the Sun. Temperature-dependent transport coefficients were found to be more complicated than its constant counterpart, and does modify the stability condition of convecting fluids. These preliminary findings, based on linear stability analysis, were shown to provide an effective stabilising mechanism as transport coefficients exhibit the dependency on temperature, and therefore suggesting that non-linear calculations of temperature-dependent coefficients may alter the dynamics further.

For future work, there are several interesting directions of research to extend and improve the work presented in this thesis. The frameworks proposed in Chapters 3 and 4 can be built on by considering the effect of various factors that are present in the Sun, and exploring their impact on the efficiency of pumping and properties of emerging magnetic structures. Such factors include shear, rotation, and nature of the magnetic field.

Furthermore, I intend to extend the investigations conducted in Chapter 4 to

consider three-dimensional flows of higher Rayleigh numbers. Though numerically demanding to perform, these simulations will allow us to reach convective flows of relatively comparable turbulence to the quasi two-dimensional simulations, and therefore enable us to examine and directly compare the mechanisms of magnetic field transport in quasi two-dimensional and three-dimensional frameworks.

Moving attention to Chapter 5, I aim to carry out further calculations to determine the onset of convection in the presence of magnetic fields, for temperature-dependent transport coefficients. This is followed by conducting non-linear calculations of the temperature-dependent coefficients and comparing them with the constant coefficient models, in order to better understand their contribution to the overall evolution of the desired system.

Finally, it is worth mentioning that the physics of the Sun have not been thoroughly understood yet and remain a great challenge, however by focusing on the pieces, and tailoring approaches to provide an insight into the physical interactions, we are gradually being able to build a coherent picture of the dynamics in the interior regions of the Sun, and other stars.

Appendix A

The Interplay between Convection Patterns and Magnetic Field

Various convectively-driven plumes are considered, with their dynamics examined as they interact with the underlying magnetic field. The preliminary work discussed in this Appendix is to merely provide an insight into the influence of different convective motions (laminar to turbulent) on the action of magnetic flux structures. Using the exact set-up in Chapter 4, a localised two-layer Cartesian plane of a compressible fluid in quasi two-dimensions is considered, where the dynamical evolution is described by the set of coupled, non-linear, dimensionless MHD Equations (4.1)-(4.6), subject to the boundary conditions specified in Equation (4.9). The system of equations is solved numerically on a uniform computational grid using the parallel hybrid finite-difference/pseudo-spectral code discussed in Subsection 3.2.5.

In the absence of magnetic field, a series of numerical simulations are carried out to find a range of parameter combinations that give steady and various time-dependent convection. The parameter settings in this model are not intended to reflect on the conditions in the inner layers of the Sun. Since the extreme diffusivities present in the Sun cannot be fully resolved using current

processing power, the dissipative length-scales chosen are of larger scales compared to the solar interior, but the same order of diffusivities is maintained, i.e. $1 \gg \zeta_0 \gg \sigma$ and $C_k \ll 1$ (Barker *et al.*, 2012). One way to observe these convection patterns is by varying the values of the Rayleigh number, Ra, defined by Equation (4.8). Hence, I choose to fix all parameters and vary the Prandtl number, which appears in the Rayleigh number, to give rise to the different types of convection, as listed in Table A.1.

Parameter	Description	Value
σ	Prandtl number	Variable
C_k	Thermal diffusivity	0.35
θ	Thermal stratification	4.0
γ_s	Ratio of specific heats	5/3
m_T, m_B	Polytropic indicies	1.0, 4.0
λ_x, λ_y	Box horizontal aspect ratio	8.0, 8.0
d	Vertical depth of box	2.0

Table A.1: The choice of parameters for the hydrodynamic cases.

The onset of buoyancy-driven convection, as we recall, occurs once Ra exceeds a critical threshold value. The developmental transition from stable to unstable can be demonstrated by the temporal evolution of the total kinetic energy, defined by Equation (3.31). The evolution for a range of Prandtl numbers is displayed in Figure A.1. Primarily, the initial peaks in the kinetic energy of the system, as clearly shown in Figure A.1(a), pursue from the initial perturbations in the equilibrium state to trigger instabilities. The amplitude of perturbations in Figure A.1(a) simply decays in time, which denotes the stability of the system. On the other hand, in Figures A.1(b)-(f), the perturbations begin to grow later in time and the onset of convective instabilities is the dominant phenomena, with various unstable flows emerging, that range from laminar to turbulent, as the values of the Prandtl number decrease in this set-up. For smaller values of the Prandtl number, i.e. larger values of the Rayleigh number, irregular oscillations appear with higher kinetic energy levels.

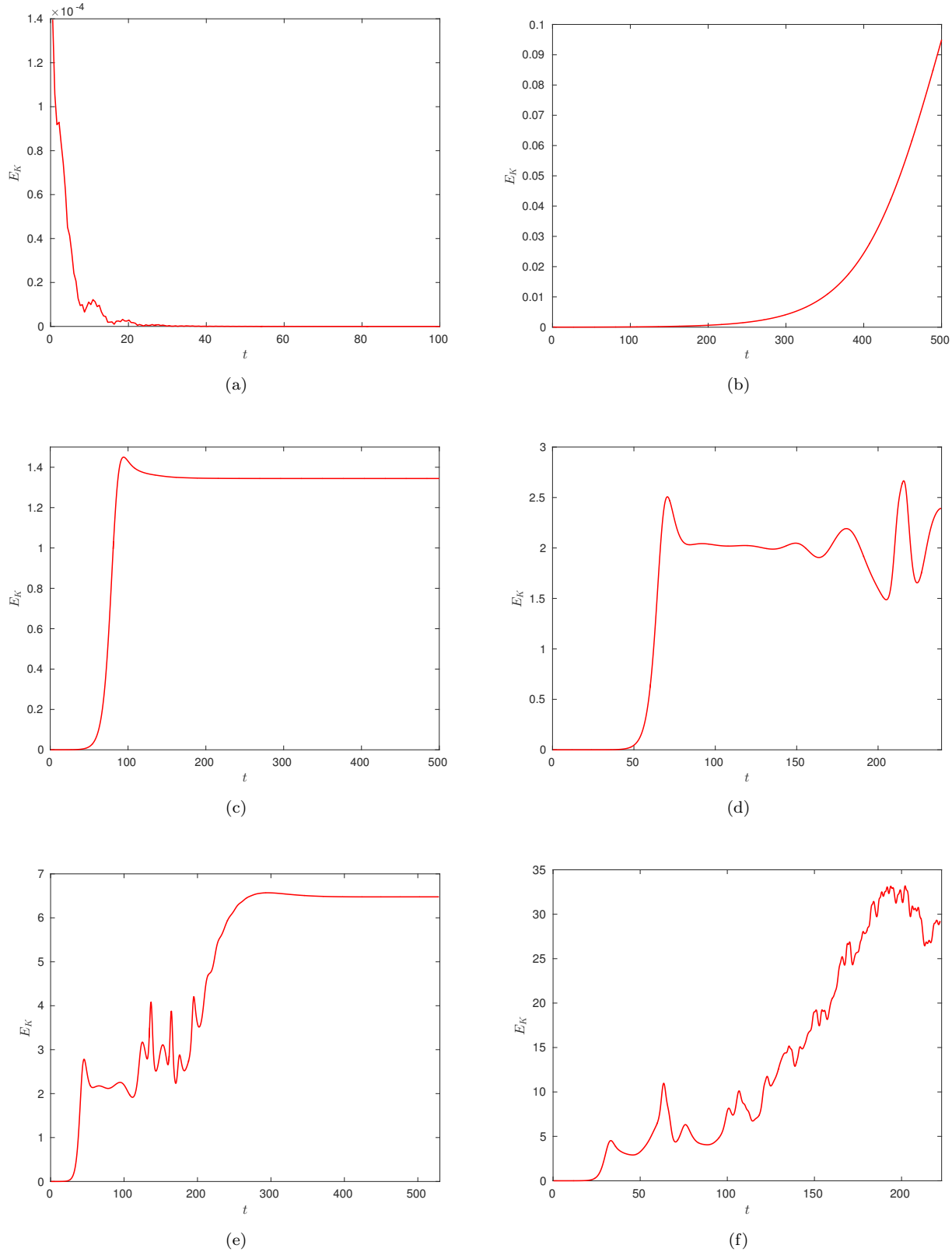

Figure A.1: Temporal evolution of the total kinetic energy E_k for (a) $\sigma = 0.3$, $Ra = 522.39$, (b) $\sigma = 0.2$, $Ra = 783.58$, (c) $\sigma = 0.15$, $Ra = 1044.77$, (d) $\sigma = 0.11$, $Ra = 1424.69$, (e) $\sigma = 0.1$, $Ra = 1567.16$, and (f) $\sigma = 0.05$, $Ra = 3134.32$ respectively.

The current resolution of $256 \times 1 \times 300$ is downscaled, in some cases, to $128 \times 1 \times 200$ in order to reduce the computational time. However, the choices of resolution are carefully tested for numerical instabilities by investigating the global kinetic energy spectrum in each simulation. The energy at each wave number, k, is tracked by transforming the results from real to Fourier space. At initial modes, large energy levels are expected that should reach fairly small or zero energy levels before reaching the cut-off frequency $2k/3$. Figure A.2 illustrates the logarithmic plot of the kinetic energy spectrum for low- and high-resolution calculations of $\sigma = 0.11$. Although both plots, in Figure A.2, are statistically about the same, the right plot is a better choice as to ensure accurate results since there is no discontinuity in the kinetic energy spectrum.

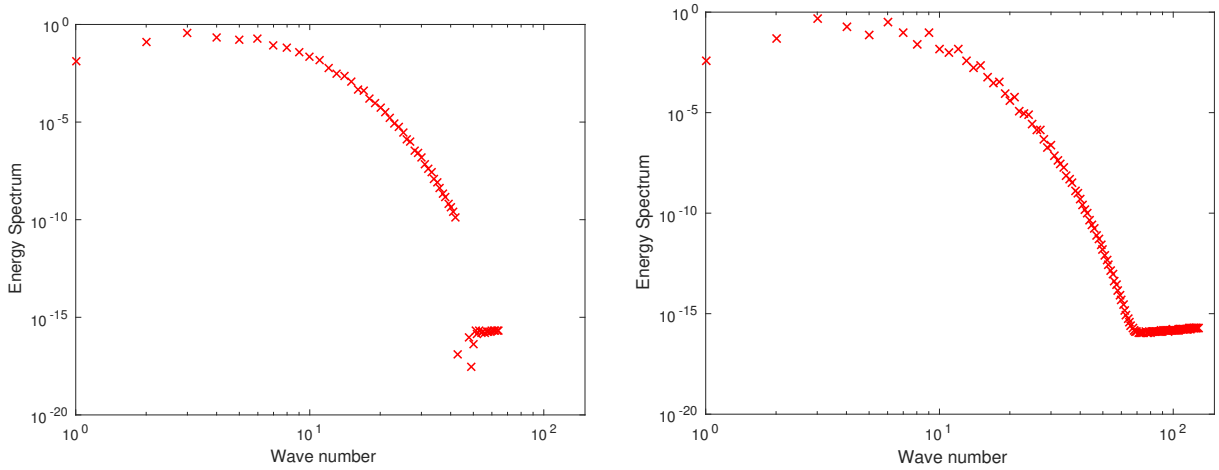

Figure A.2: The energy spectrum versus wave number on logarithmic scales for a low resolution simulation of $128 \times 1 \times 200$ (left), and a high resolution simulation $256 \times 1 \times 300$ (right).

All numerical experiments have been performed for sufficiently long enough to ensure that the system is settled and to define the convection patterns correctly. From Figure A.1(b), one could conclude steady convection by noticing the saturation of the kinetic energy plot up to $t \approx 120$. For steady convection, an additional measure is taken by calculating the slope of the energy level, and ensuring a zero gradient.

Figures A.3 and A.4 highlight the motion of convective plumes by displaying pseudo-colour snapshots of the horizontal and vertical components of the velocity field for the steady, and moderately turbulent regimes respectively. Horizontally, the colour blue (red) indicates right-moving (left-moving) convective cells, while vertically blue (red) indicates a downward (upward) direction of motion. In the steady case, $\sigma = 0.15$, the system consists of three equally-spaced convection cells undergoing circular motion at almost constant speeds.

However, moving attention to time-dependent convective patterns, Figure A.4 shows snapshots of the velocity for case $\sigma = 0.05$, in both horizontal and vertical directions. Unlike the steady case, the motion in the time-dependent cases involves transitions in the number of cells. As the Prandtl number becomes smaller, the configurations of the convective cells become random and lead to more vigorous convective flows in time.

Similar to the approach conducted in Chapter 4, a horizontal magnetic slab is introduced to the non-convective region in the bottom layer once the convective flows are established in the upper layer of the domain. The horizontally aligned magnetic field in the y-direction, $B_y = 1$, is inserted in the lower region, where no significant motion is present due to the composite polytropic configuration. The magnetic field is imposed in the region $1.6 \leq z \leq 1.8$ and is in an initial magnetostatic equilibrium with its surroundings.

Given the choice of parameters in the hydrodynamic regime (Table A.1), magnetic diffusivity must yield to significantly high diffusion rates to satisfy the condition $1 \gg \zeta_0 \gg \sigma$. Thus, convection becomes insufficient to suppress and interact with the underlying magnetic field. To see this, Figure A.5 shows the evolution of the field B_y when imposing one of the various field strengths tested, and choosing the magnetic diffusivity such that $1 \gg \zeta_0 = 0.1 \gg \sigma = 0.06$ for a turbulent convective flow. The evolution of the horizontal magnetic field,

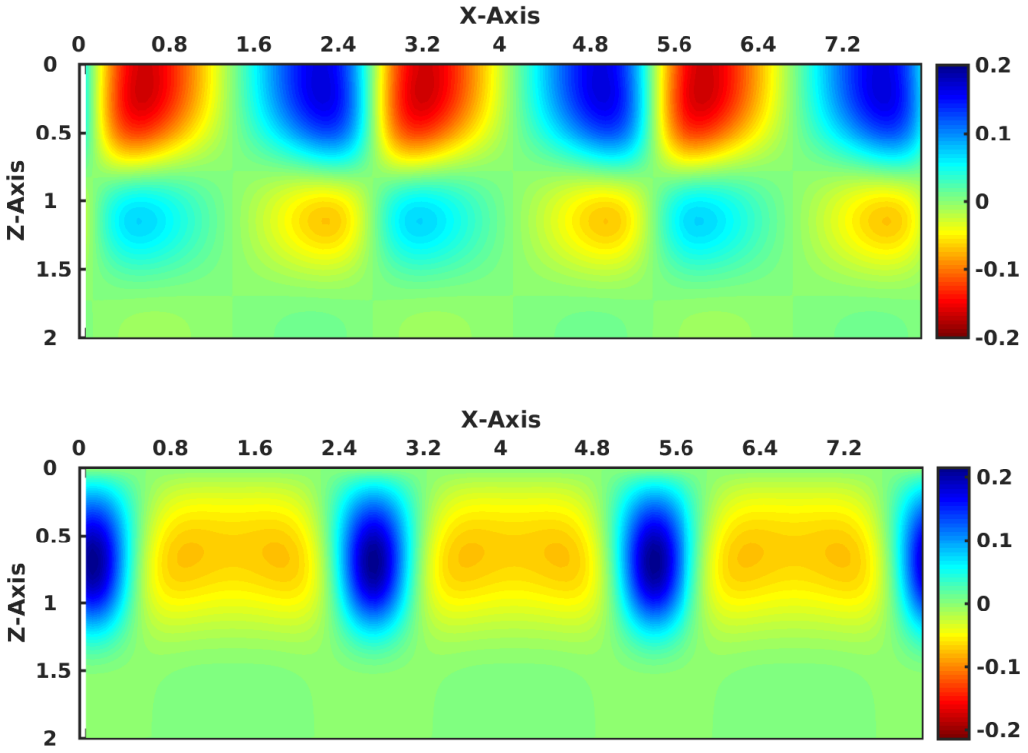

(a)

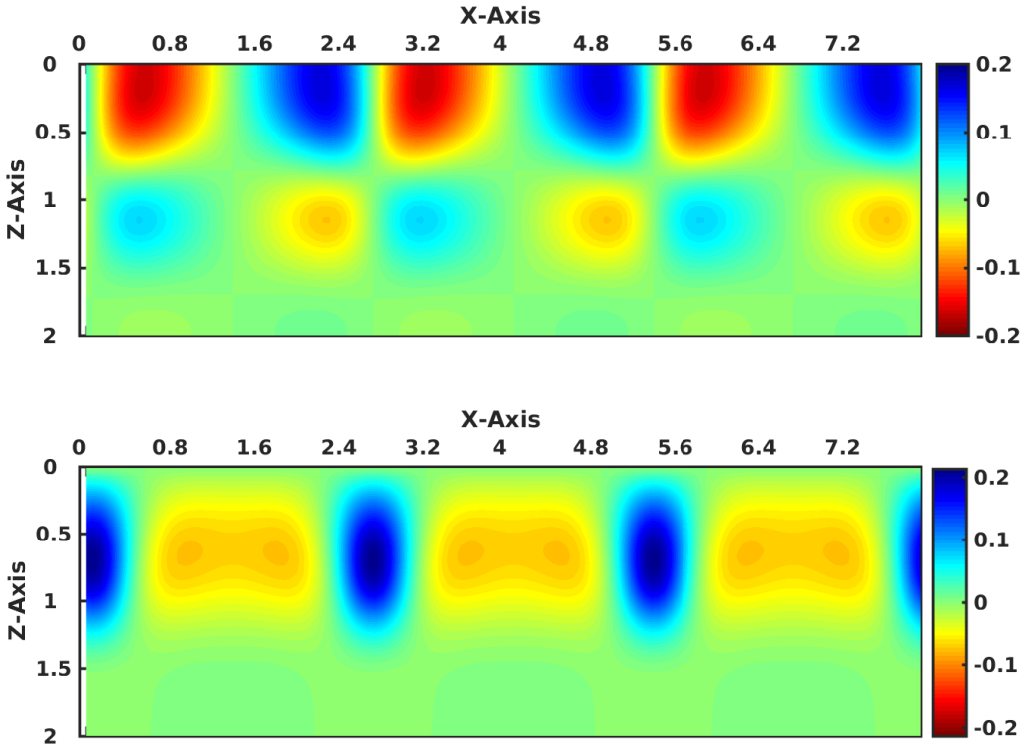

(b)

Figure A.3: Snapshots of the horizontal component (top panel) and vertical component (bottom panel) of the velocity field for $\sigma = 0.15$ at computational times (a) $t = 215.8$ and (b) $t = 323.3$.

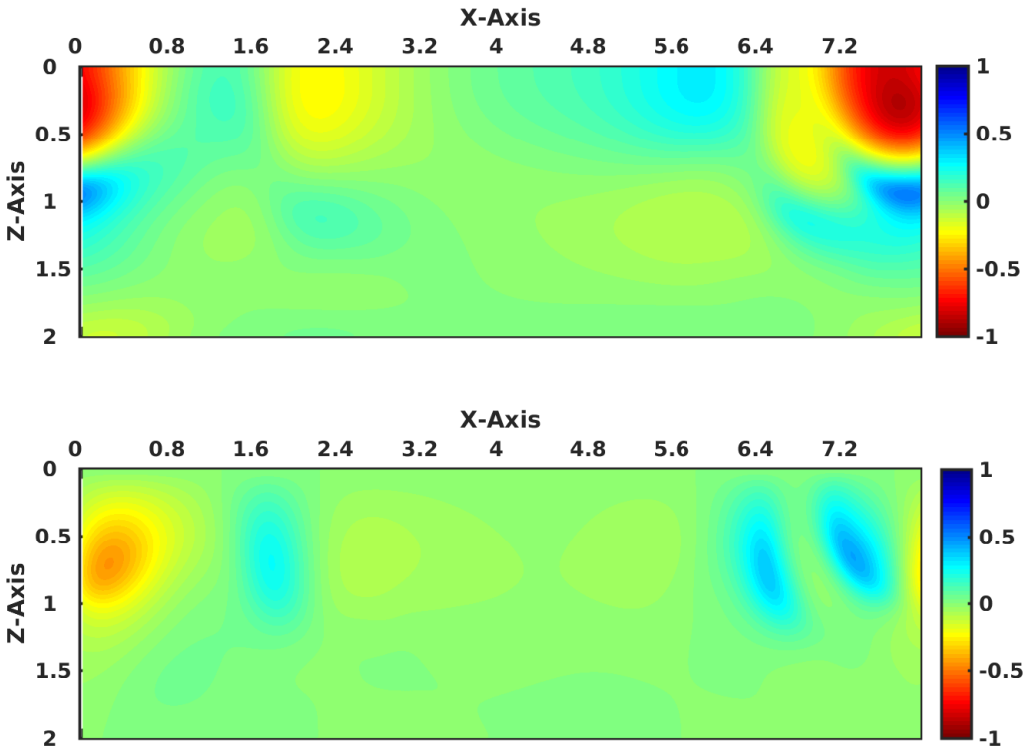

(a)

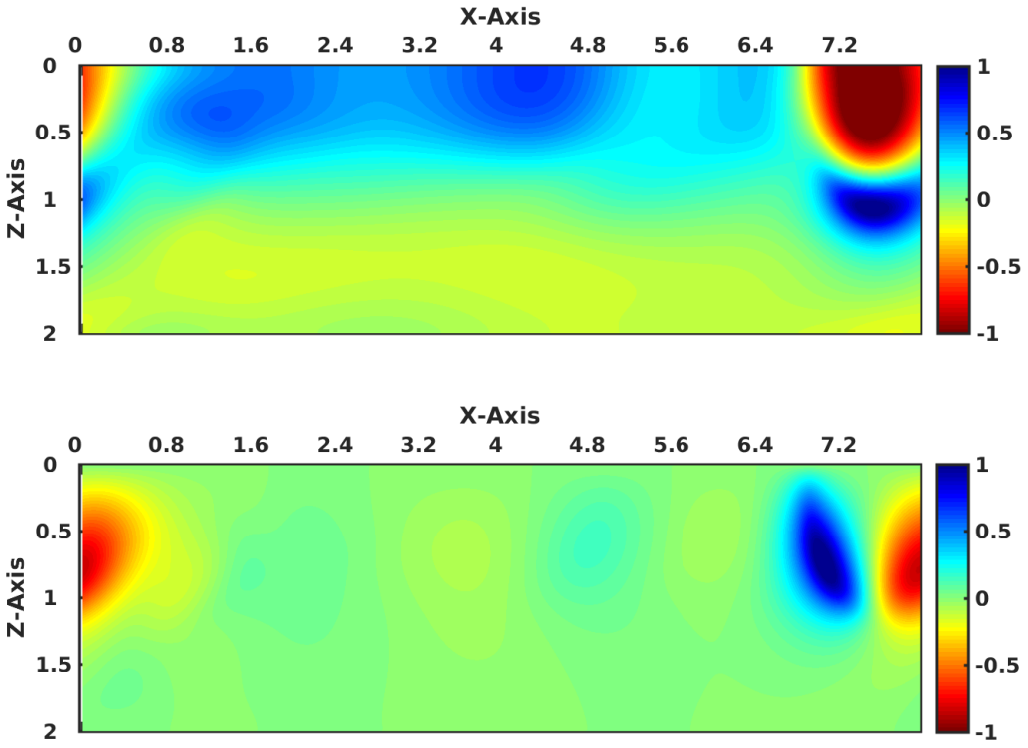

(b)

Figure A.4: Snapshots of the horizontal component (top panel) and vertical component (bottom panel) of the velocity field for $\sigma = 0.05$ at computational times (a) $t = 118.3$ and (b) $t = 222.1$.

B_y, shows that the field is highly diffusive, and can easily overcome convection. Therefore, the imposed field rises almost unimpeded, while it decays in strength due to the absence of mechanisms that generate the field.

In this context, it is necessary to reduce the magnetic diffusion term and ensure the order of diffusivities condition remains satisfied. By doing so, the Prandtl number must be scaled down, which is responsible for the different convection patterns in this framework. Additionally, for ease of computation, I choose to reduce the values of the thermal diffusivity and stratification. The modified set of parameters is found in Table A.2.

Parameter	Description	Value
σ	Prandtl number	Variable
C_k	Thermal diffusivity	0.1
θ	Thermal stratification	0.5
γ_s	Ratio of specific heats	5/3
ζ_0	Magnetic diffusivity	0.01
F	Magnetic field strength	Variable

Table A.2: The choice of parameters for the magnetohydrodynamic cases.

For the parameter values in Table A.2, steady and time-dependent convective flows are achieved by setting $\sigma = 0.02$ ($Ra \approx 625$) and $\sigma = 0.001$ ($Ra \approx 12500$) respectively. The total kinetic energy for these regimes are shown in Figure A.6. Contrasting with the kinetic energy plots in Figure A.1, the kinetic energies in these cases indicate broader convective timescales with delays in the onset time of convection. The energy contained in the convective flows, according to the total kinetic energies, also appear to be weaker in these modified parameter regimes.

By setting the magnetic field strength $F = 0.1$, the imposed magnetic field is observed to slowly diffuse until it is held back by the overlying, fully developed convective motion. The system acts to suppress the magnetic field in regions where the motion is downward, as indicated in blue in Figure A.7,

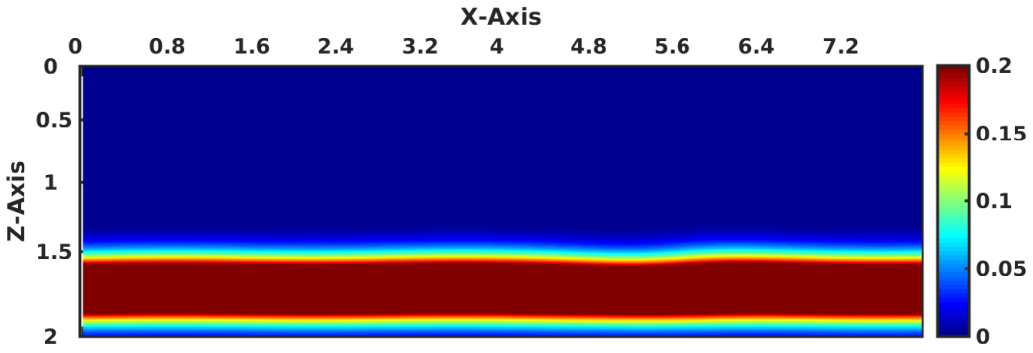

(a)

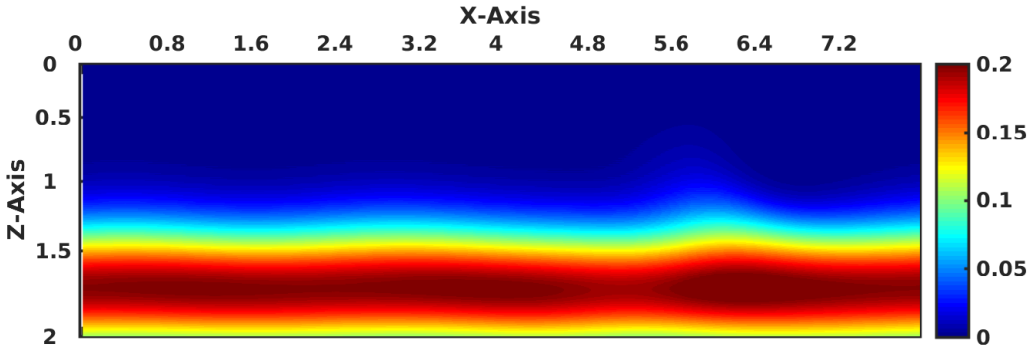

(b)

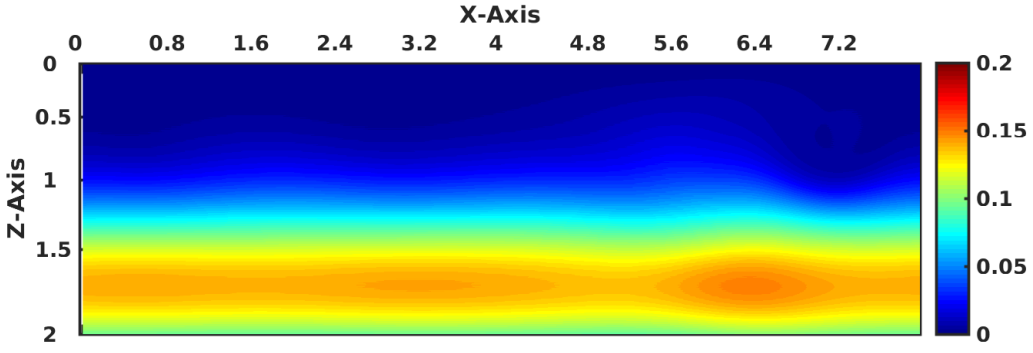

(c)

Figure A.5: Snapshots of the horizontal component of the magnetic field for $\sigma = 0.06$, $F = 0.01$ and $\zeta = 0.1$ at computational times (a) $t = 477.3$, (b) $t = 479.1$ and (c) $t = 481.4$. The magnetic field is imposed at $t = 476.9$ once convection is fully developed in the upper domain.

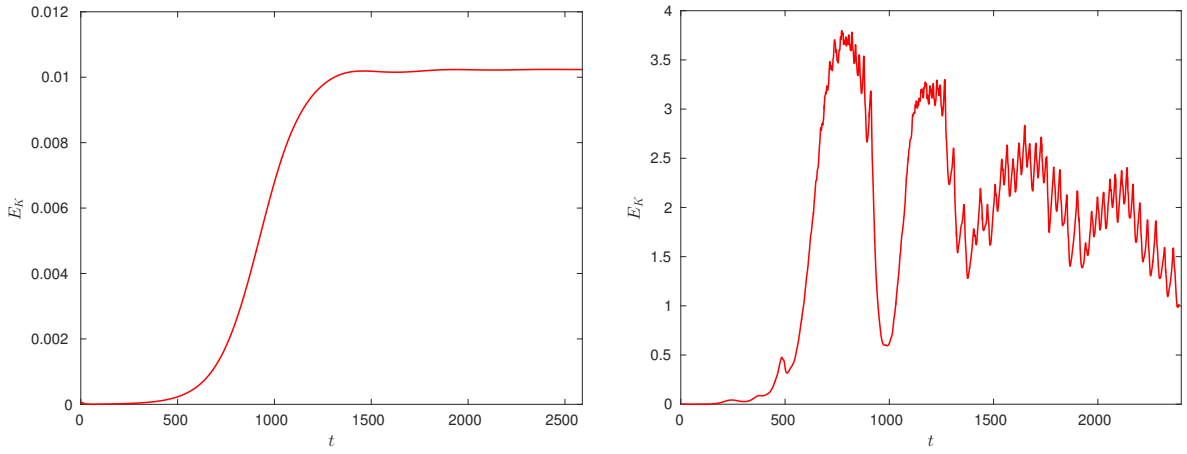

(a) (b)

Figure A.6: Temporal evolution of the kinetic energy E_k for (a) $\sigma = 0.02$, $Ra \approx 625$ and (b) $\sigma = 0.001$, $Ra \approx 12500$.

for the steady case $\sigma = 0.02$. Further, the buckling regions suggest that the magnetic field is being carried by convective upflows to the unstable region, which indicates that advection is the predominant transport process in this regime. However, given the chaotic nature of turbulent convection, it is of interest to analyse the evolution of the field in the regime where $\sigma = 0.001$, and thereafter investigate the mechanisms for magnetic field transport throughout the unstable layer.

For $\sigma = 0.001$, the behaviour of the imposed magnetic field is explored for a range of magnetic field strengths, $0.001 \leq F \leq 1.0$. Figure A.8 captures the magnetoconvection interactions for $F = 0.001$ and $F = 1.0$. Generally, the dynamics reveal the passive role of magnetic fields as the system evolves with time. No apparent evidence is extracted that suggests the contribution of other processes to the transport of the underlying magnetic field.

The convective timescales in these simulations seem to be too long for effective pumping to be achieved in the unstable layer, and thus are not ideal to investigate given that, for instance, magnetic buoyancy occurs on relatively short timescales. Therefore, we chose to further modify the parametric set-

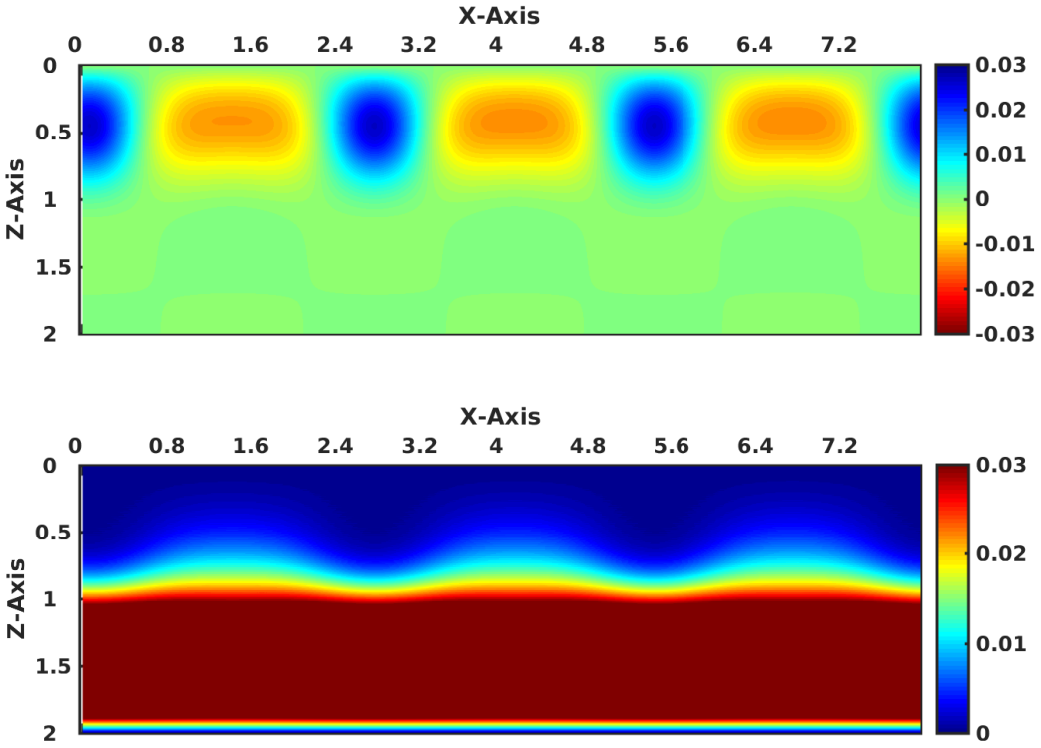

Figure A.7: Snapshots of the vertical component of the velocity field (top panel) and horizontal component of the magnetic field (bottom panel) for $\sigma = 0.02$ and $F = 0.1$ at computational time $t = 2215.6$. The magnetic field is imposed at $t = 2070.8$ once convection is fully developed in the upper domain.

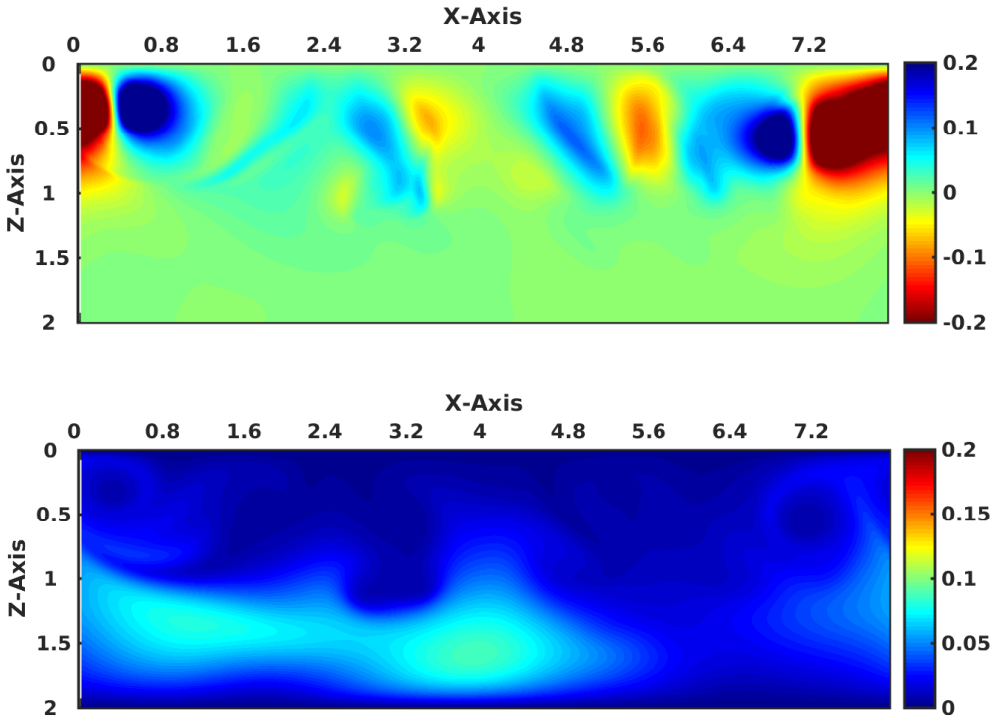

(a)

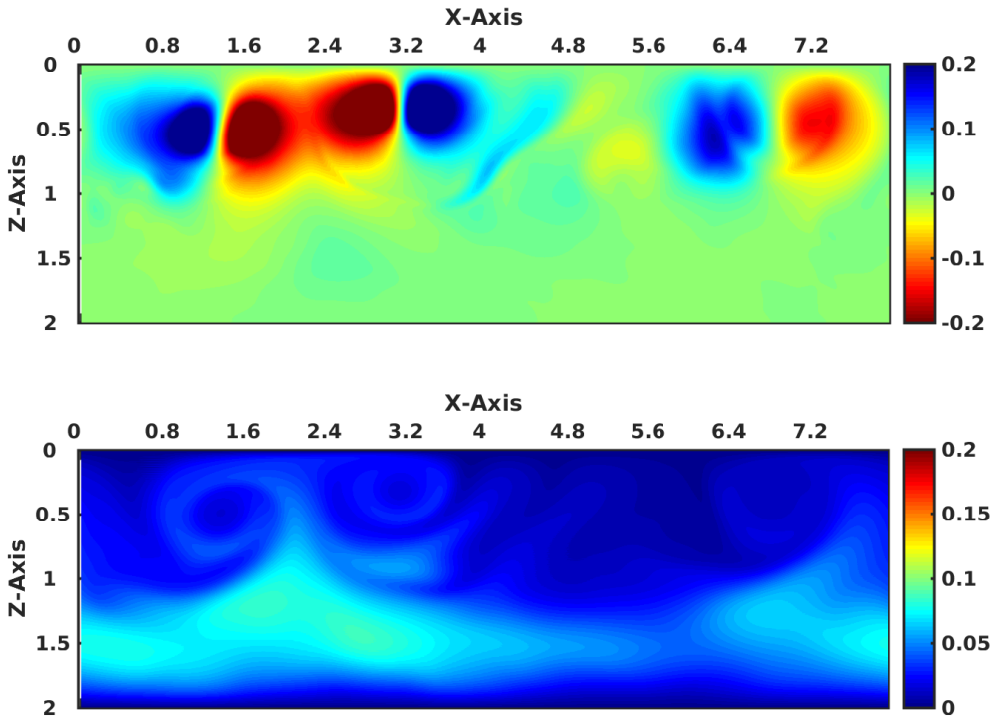

(b)

Figure A.8: Snapshots of the vertical component of the velocity field (top panel) and horizontal component of the magnetic field (bottom panel) for $\sigma = 0.001$ and (a) $F = 0.001$ at computational time $t = 2181.3$ and (b) $F = 1.0$ at computational time $t = 2104.9$. The magnetic field is imposed at $t = 1910.7$ once convection is fully developed in the upper domain.

tings, in a computationally efficient way as proposed in Chapter 4, to promote the effect of turbulent convection.

Bibliography

Ali, A.A. and Silvers, L.J., 2018. The Effect of Time-Dependent γ-Pumping on Buoyant Magnetic Structures. *Geophys. Astrophys. Fluid Dyn.* **112**, 414.

Babcock, H.W., 1961. The Topology of the Sun's Magnetic Field and the 22-Year Cycle. *Astrophys. J.* **133**, 572.

Barker, A.J., Silvers, L.J., Proctor, M.R.E. and Weiss, N.O., 2012. Magnetic Buoyancy Instabilities in the Presence of Magnetic Flux Pumping at the Base of the Solar Convection Zone. *Mon. Not. Roy. Astron. Soc.* **424**, 115.

Battrick, B.T., 1990. *Formation of Stars and Planets and the Evolution of the Solar System: Proceedings of the 24th ESLAB Symposium, 17-19 September, Friedrichshafen.* Noordwijk: ESA ESTEC.

Bhatnagar, A. and Livingston W.C., 2005. *Fundamentals of Solar Astronomy.* World Scientific Publ. Co.

Böhm-Vitense, E., 1992. *Introduction to Stellar Astrophysics.* Cambridge Univ. Press.

Botha, G.J.J., Rucklidge, A.M. and Hurlburt, N.E., 2011. Nonlinear Three-dimensional Magnetoconvection around Magnetic Flux Tubes. *Astrophys. J.* **731**, 108.

Boussinesq, J., 1903. Thêorie Analytique de la Chaleu. *Paris: Gauthier-Vellars.* **2**, 172.

Brandenburg, A., Jennings, R.L., Nordlund, Å., Rieutord, M., Stein, R.F. and Tuominen, I., 1996. Magnetic Structures in a Dynamo Simulation. *J. Fluid Mech.* **306**, 325.

Brandenburg, A. and Subramanian, K., 2005. Astrophysical Magnetic Fields and Nonlinear Dynamo Theory. *Phys.Rep.* **417**, 1.

Brandenburg, A., Tuominen, I., Nordlund, Å., Pulkkinen, P., and Stein, R.F., 1990. 3-D Simulation of Turbulent Cyclonic Magneto-Convection. *Astron. Astrophys.* **232**, 277.

Browning, M.K., Miesch, M.S., Brun, A.S. and Toomre, J., 2006. Dynamo Action in the Solar Convection Zone and Tachocline: Pumping and Organization of Toroidal Fields. *Astrophys. J.* **648**, L157.

Brummell, N., Toomre, J. and Cattaneo, F., 1995. Turbulent Dynamics in the Solar Convection Zone. *Science.* **269**, 1370.

Brun, A.S. and Browning, M.K., 2017. Magnetism, Dynamo Action and the Solar-Stellar Connection. *Living Rev. Solar Phys.* **14**, 4.

Bumba, V. and Suda, J., 1971. Some Remarks on the Statics and Dynamics of Magnetic Field Structure Development in Active Regions. In *Solar Magnetic Fields*, edited by R. Howard. Springer Science & Business Media.

Burnell, S.J.B., 2004. *An Introduction to the Sun and Stars.* Cambridge Univ. Press.

Bushby, P.J. and Archontis, V., 2012. Modelling Magnetic Flux Emergence in the Solar Convection Zone. *Astron. Astrophys.* **545**, A107.

Bushby, P.J., Käpylä, P.J., Masada, Y., Brandenburg, A., Favier, B., Guervilly, C. and Käpylä, M.J., 2018. Large-Scale Dynamos in Rapidly Rotating Plane Layer Convection. *Astron. Astrophys.* **612**, A97.

Busse, F.H., 1985. Transition to Turbulence in Rayleigh-Bénard Convection. In *Hydrodynamic Instablities and the Transition to Turbulence*, edited by H.L. Swinney and J. Gollub. Springer Science & Business Media.

Calkins, M.A., Julien, K. and Marti, P., 2014. Onset of Rotating and Non-Rotating Convection in Compressible and Anelastic Ideal Gases. *Geophys. Astrophys. Fluid Dyn.* **109**, 422.

Canuto, C., Hussaini, M.Y., Quarteroni, A. and Zang, T.A., 2006. *Spectral Methods: Fundamentals in Single Domain*. Springer Science & Business Media.

Carrington, R.C., 1858. On the Distribution of the Solar Spots in Latitudes since the Beginning of the Year 1854. *Mon. Not. Roy. Astron. Soc.*. **19**, 1.

Carrington, R.C., 1859. Description of a Singular Appearance Seen in the Sun on September 1, 1859. *Mon. Not. Roy. Astron. Soc.*. **20**, 13.

Cattaneo, F., Emonet, T. and Weiss, N.O., 2003. On the Interaction between Convection and Magnetic Fields. *Astrophys. J.* **588**, 1183.

Cattaneo, F. and Hughes, D.W., 1988. The Nonlinear Breakup of a Magnetic Layer: Instability to Interchange Modes. *Icarus*. **196**, 323.

Cattaneo, F. and Hughes, D.W., 2001. Solar Dynamo Theory: A New Look at the Origin of Small-Scale Magnetic Fields. *Astron. Geophys.* **42**, 3.18.

Cattaneo, F. and Vainshtein, S.I., 1991. Suppression of Turbulent Transport by a Weak Magnetic Field. *Astrophys. J.* **376**, L21.

Chandrasekhar, S., 1939. *An Introduction to the Study of Stellar Structure*. Univ. Chicago Press.

Chandrasekhar, S., 1952. On the Inhibition of Convection by a Magnetic Field. *Phil. Mag.* **43**, 501.

Chandrasekhar, S., 1961. *Hydrodynamic and Hydromagnetic Stability*. Oxford Univ. Press.

Chandrasekhar, S., 2003. *An Introduction to the Study of Stellar Structure*. Dover Publ. Inc.

Charbonneau, P., 2005. Dynamo Models of the Solar Cycle. *Living Rev. Solar Phys.* **2**, 2.

Charbonneau, P., 2010. Dynamo Models of the Solar Cycle. *Living Rev. Solar Phys.* **7**, 3.

Charbonneau, P., 2014. Solar Dynamo Theory. *Annu. Rev. Astron. Astrophys.* **52**, 251.

Charbonneau, P., Christensen-Dalsgaard, J., Henning, R., Larsen, R.M., Schou, J., Thompson, M.J. and Tomczyk, S., 1999. Helioseismic Constraints on the Structure of the Solar Tachocline. *Astrophys. J.* **527**, 445.

Choudhuri, A.R., 1998. *The Physics of Fluids and Plasma*. Cambridge Univ. Press.

Choudhuri, A.R., 2015. *Nature's Third Cycle: A Story of Sunspots*. Oxford Univ. Press.

Christensen-Dalsgaard, J., 2008. Helio- and Asteroseismology. *Proc. Int. Astron. Union*. **4**, 135.

Christensen-Dalsgaard, J. and Thompson, M., 2007. Observational Results and Issues Concerning the Tachocline. In *The Solar Tachocline*, edited by D.W. Hughes, R. Rosner and N.O. Weiss. Cambridge Univ. Press.

Clarke, C. and Carswell, 2007. *Principles of Astrophysical Fluid Dynamics*. Cambridge Univ. Press.

Cline, K.S., Brummell, N.H. and Cattaneo, F., 2003. On the Formation of Magnetic Structures by the Combined Action of Velocity Shear and Magnetic Buoyancy. *Astron. and Astrophys.* **588**, 630.

Crouch, J.D., 2016. Theory of Instability and Transition. In *Handbook of Fluid Dynamics*, edited by R.W. Johnson. CRC Press.

Currie, L.K., 2016. The Effect of Magnetic Field on Mean Flow Generation by Rotating Two-Dimensional Convection. *Astrophys. J.* **832**, 1.

Davidson, P.A., 2001. *An Introduction to Magnetohydrodynamics*. Cambridge Univ. Press.

Demarque, P. and Guenther, D.B., 1991. Post-Main-Sequence Solar Evolution. In *Solar Interior and Atmosphere*, edited by A.N. Cox, W.C. Livingston and M.S. Matthews. Univ. Arizona Press.

Demarque, P. and Guenther, D.B., 1999. Helioseismology: Probing the Interior of a Star. *PNAS*. **96**, 5356.

Deubner, F.-L., Ulrich, R.K. and Rhodes, E.J., Jr., 1979. Solar p-mode Oscillations as a Tracer of Radial Differential Rotation. *Astron. and Astrophys.* **72**, 177.

Dikpati, M. and Gilman, P.A., 2001. Flux-Transport Dynamos with α Effect from Global Instability of Tachocline Differential Rotation: A Solution for Magnetic Parity Selection in the Sun. *Astrophys. J.* **559**, 428.

Drazin, P.G. and Reid, W.H., 2004. *Hydrodynamic Stability*. Cambridge Univ. Press.

Drew, S.J., Jones, C.A. and Zhang, K.K., 1995. Onset of Convection in a Rapidly Rotating Compressible Fluid Spherical Shell. *Geophys. Astrophys. Fluid Dyn.* **80**, 241.

Durran, D.R., 2013. *Numerical Methods for Wave Equations in Geophysical Fluid Dynamics*. Springer Science & Business Media.

Dziembowski, W. A., Fiorentini, G., Ricci B. and Sienkiewicz, R., 1999. Helioseismology and the Solar Age. *Astron. Astrophys.* **343**, 990.

Fan, Y., 2001. Nonlinear Growth of the Three-Dimensional Undular Instability of a Horizontal Magnetic Layer and the Formation of Arching Flux Tubes. *Astrophys. J.* **546**, 509.

Fan, Y., 2009. Magnetic Fields in the Solar Convection Zone. *Living Rev. Solar Phys.* **6**, 4.

Favier, B., Jouve, L., Edmunds, W., Silvers, L.J. and Proctor, M.R.E., 2012. How can Large-Scale Twisted Magnetic Structures Naturally Emerge from Buoyancy Instabilities?. *Mon. Not. Roy. Astron. Soc.*. **426**, 3349.

Fearn, D.R., 2013, *4H Magnetohydrodynamics Lecture Notes*. Univ. Glasgow.

Foukal, P., 1990. *Solar Astrophysics*. Wiley.

Fox, D.G. and Orszag, S.A., 1973. Pseudospectral Approximation to Two-Dimensional Turbulence. *J. Comp. Phys.* **11**, 612.

Galloway, D.J. and Weiss, N.O., 1981. Convection and Magnetic Fields in Stars. *Astrophys. J.* **243**, 945.

Gilman, P.A., 2005. The Tachocline and the Solar Dynamo. *Astron. Nachr.*. **326**, 208.

Glatzmaier, G.A. and Gilman, P.A., 1981. Compressible Convection in a Rotating Spherical Shell. IV. Effects of Viscosity, Conductivty, Boundary Conditions and Zone Depth. *Astrophys. J. Suppl. Ser.* **47**, 103.

Graham, S., 2000. *Sunspots and the Solar Max*. NASA Earth Observatory.

Graham, E. and Moore, D.R., 1978. The Onset of Compressible Convection. *Mon. Not. Roy. Astron. Soc.* **183**, 617.

Grasselli, M. and Pelinovsky, D., 2008. *Numerical Mathematics*. Jones & Bartlett Learning.

Goody, R.M., 1956. The Influence of Radiative Transfer on Cellular Convection. *J. Fluid Mech.* **1**, 424.

Gough, D.O., 2007. An Introduction to the Solar Tachocline. In *The Solar Tachocline*, edited by D.W. Hughes, R. Rosner and N.O. Weiss. Cambridge Univ. Press.

Gough, D.O., Moore, D.R., Spiegel, E.A and Weiss, N.O., 1976. Convective Instability in a Compressible Atmosphere. II. *Astrophys. J.* **206**, 536.

Hale, G.E., 1908. On the Probable Existence of a Magnetic Field in Sun-spots. *Astrophys. J.*. **28**, 315.

Hale, G.E., Ellerman, F., Nicholson S.B. and Joy, A.H., 1919. The Magnetic Polarity of Sunspots. *Astrophys. J.*. **49**, 153.

Hanasoge, S.M., Miesch, M.S., Schou, J., Schüssler, M. and Thompson, M., 2015. Solar Dynamics, Rotation, Convection and Overshoot. *Space Sci. Rev.*. **196**, 79.

Hanslmeier, A., 2007. *The Sun and Space Weather*. Springer Science & Business Media.

Harrison, R.A., 2008. The Magnetic Sun. *Philos. T. Roy. Soc.* **366**, 1735.

Harvey, J.W., 1988. Solar Internal Rotation from Helioseismology. *In ESA, Seismology of the Sun and Sun-Like Stars*. 55.

Hathaway, D.H., 2015. The Solar Cycle. *Living Rev. Solar Phys.* **12**, 4.

Hathaway, D.H., Beck, J.G., Bogart, R.S., Bachmann, K.T., Khatri, G., Petitto, J.M., Han, S. and Raymond, J., 2000. The Photospheric Convection Spectrum. *Solar Phys.* **193**, 299.

Hendry, A.W., 1993. A polytropic model of the Sun. *Am. J. Phys.* **61**, 906.

Heng, K., 2017. *Exoplanetary Atmospheres: Theoretical Concepts and Foundations*. Princeton Univ. Press.

Herschel, W., 1795. On the Nature and Construction of the Sun and Fixed Stars. *The Royal Society.* **85**, 46.

Hood, A.W. and Hughes D.W., 2011. Solar Magnetic Fields. *Phys. of the Earth and Planetary Interiors*. **187**, 78.

Hoyng, P., 2012. Mean Field Dynamo Theory. In *The Sun: A Laboratory for Astrophysics*, edited by J.T. Schmelz and R. Brown. Springer Science & Business Media.

Hughes, D.W., 2007. Magnetic Buoyancy Instabilites in the Tachocline. In *The Solar Tachocline*, edited by D.W. Hughes, R. Rosner and N.O. Weiss. Cambridge Univ. Press.

Hughes, D.W., Proctor, M.R.E. and Cattaneo F., 2011. The α-Effect in Rotating Convection: A Comparison of Numerical Simulations. *Mon. Not. Roy. Astron. Soc.* **414**, L45.

Hurlburt, N.E., 1983. *Compressible Convection. Ph.D. Thesis.* Univ. Colorado.

Hurlburt, N.E., Toomre, J. and Massaguer, J.M., 1984. Two-Dimensional Compressible Convection Extending Over Multiple Scale Heights. *Astrophys. J.* **282**, 557.

Hurlburt, N.E., Toomre, J., Massaguer, J.M. and Zahn, J.-P., 1994. Penetration Below a Convective Zone. *Astrophys. J.* **421**, 245.

Jeffreys, H., 1926. The stability of a layer of fluid heated below. *London, Ed. and Dub. Philos. Mag. and J. Sci.* **2**, 833.

Jenkins, J.L., 2009. *The Sun and How to Observe it.* Springer Science & Business Media.

Johnson, S.G., 2011, *Notes on FFT-based differentiation - Applied Mathematics.* Massachusetts Institute of Technology.

Jokipii, R., Sonett, P. and Giampapa, S., 1997. *Cosmic Winds and the Heliosphere.* Univ. Arizona Press.

Jones, C.A., Boronski, P., Brun, A., Glatzmaier, G., Gastine, T., Miesch, M., and Wicht, J., 2011. Anelastic Convection-Driven Dynamo Benchmarks. *Icarus.* **216**, 120.

Jones, C.A. and Moore, D.R., 1978. The Stability of Axisymmetric Convection. *Geophys. Astrophys. Fluid Dyn.* **11**, 245.

Jones, C.A., Thompson, M.J. and Tobias, S.M., 2010. The Solar Dynamo. *Space Sci. Rev.*. **152**, 591.

Joseph, D.D., 1976. *Stability of fluid motions.* Springer Science & Business Media.

Kichatinov, L.L., 1991. Turbulent Transport of Magnetic Fields in a Highly Conducting Rotating Fluid and the Solar Cycle. *Astron. and Astrophys.* **243**, 483.

Kim, Y.-C. and Demarque, P., 1996. The Theoretical Calculation of the Rossby Number and the "Nonlocal.

Koschmieder, E.L., 1993. *Bénard Cells and Taylor Vortices.* Cambridge Univ. Press.

Kosovichev, A.G., 2011. Advances in Global and Local Helioseismology: An Introductory Review. In *The Pulsations of the Sun and the Stars*, edited by J.-P. Rozelot and C. Neiner. Springer Science & Business Media.

Krause, F. and Rädler, K.-H., 1980. *Mean Field Magnetohydrodynamics and Dynamo Theory.* Pergamon Press.

Kupka, F. and Muthsam, H.J., 2017. Modelling of Stellar Convection. *Living Rev. Comp. Astrophys.* **3**, 1.

Lang, K.R., 2012. *Sun, Earth and Sky.* Springer.

Lappa, M., 2009. *Thermal Convection: Patterns, Evolution and Stability.* John Wiley & Sons.

Leighton, R.B., Noyes, R.W. and Simon, G.W., 1962. Velocity Fields in the Solar Atmosphere. I. Preliminary Report. *Astrophys. J.* **135**, 474.

Leighton, R.B., 1969. A Magneto-Kinematic Model of the Solar Cycle. *Astrophys. J.* **156**, 1.

LeVeque, R.J., 2007. *Finite Difference Methods for Ordinary and Partial Differential Equations: Steady-State and Time-Dependent Problems*. SIAM.

Livingston, W. and Duvall, T.L., Jr., 1978. Solar Rotation. *Kitt Peak National Observatory*. **61**, 219.

MacGregor, K.B. and Charbonneau, P., 1997. Solar Interface Dynamos. I. Linear, Kinematic Models in Cartesian Geometry. *Astrophys. J.* **486**, 484.

Manolakis, D.G. and Ingle, V.K., 2011. *Applied Digital Signal Processing: Theory and Practice*. Cambridge Univ. Press.

Massaguer, J.M. and Zahn, J.-P., 1980. Cellular Convection in a Stratified Atmosphere. *Astron. Astrophys.* **87**, 315.

Matthews, P.C., Hughes, D.W. and Proctor, M.R.E., 1995a. Magnetic Buoyancy, Vorticity, and Three-dimensional Flux-Tube Formation. *Astrophys. J.* **448**, 938.

Matthews, P.C., Proctor, M.R.E. and Weiss, N.O., 1995b. Compressible Magnetoconvection in Three Dimensions: Planforms and Nonlinear Behaviour. *J. Fluid Mech.* **305**, 281.

Mizerski, K. and Tobias, S.M., 2011. The Effect of Stratification and Compressibility on Anelastic Convection in a Rotating Plane Layer. *Geophys. Astrophys. Fluid Dyn.* **105**, 566.

Moffatt, H.K., 1978. *Magnetic Field Generation in Electrically Conducting Fluids*. Cambridge Univ. Press.

Moffatt, H.K., 1983. Transport Effects Associated with Turbulence with Particular Attention to the Influence of Helicity. *Rep. Prog. Phys.*, **46**, 621.

Mullan, D.J., 2009. *Physics of the Sun: A First Course*. CRC Press.

Muller, J., 2011. The Quiet Solar Photosphere: Dynamics and Magnetism. In *The Pulsations of the Sun and the Stars*, edited by J.-P. Rozelot and C. Neiner. Springer Science & Business Media.

NASA, 2000. *Our Dynamic Sun*. [online] Available at: ⟨http://nssdc.gsfc.nasa.gov/\planetary/factsheet/sunfact.html⟩ [Accessed 03 October 2016].

NASA, 2016. *Sun Fact Sheet*. [online] Available at: ⟨https://pwg.sci.gsfc.nasa.gov/exhibit/dynamic.html⟩ [Accessed 18 January 2019].

Nordlund, Å., Brandenburg, A., Jennings, R.L., Rieutord, M., Ruokolainen, J. and Stein, R.F., 1992. Dynamo Action in Stratified Convection with Overshoot. *Astrophys. J.* **392**, 647.

November, L.J., Toomre, J., Gebbie, K.B. and Simon, G.W., 1981. The Detection of Mesogranulation on the Sun. *Astrophys. J.* **245**, L123.

Nussbaumer, H.J., 2013. *Fast Fourier Transform and Convolution Algorithms*. Springer Science & Business Media.

Ossendrijver, M., 2003. The Solar Dynamo. *Astron. and Astrophys. Rev.* **11**, 287.

Ossendrijver, M., Stix, M. and Brandenburg, A., 2001. Magnetoconvection and Dynamo Coefficients:. Dependence of the Alpha Effect on Rotation and Magnetic Field. *Astron. Astrophys.* **376**, 713.

Ossendrijver, M., Stix, M., Brandenburg, A. and Rüdiger, G., 2002. Magnetoconvection and Dynamo Coefficients: II. Field-Direction Dependent Pumping of Magnetic Field. *Astron. and Astrophys.* **394**, 735.

Parker, E.N., 1955a. The Formation of Sunspot from the Solar Toroidal Field. *Astrophys. J.* **121**, 491.

Parker, E.N., 1955b. Hydromagnetic Dynamo Models. *Astrophys. J.* **122**, 293.

Parker, E.N., 1975. The Generation of Magnetic Fields in Astrophysical Bodies. X - Magnetic Buoyancy and the Solar Dynamo. *Astrophys. J.* **198**, 205.

Parker, E.N., 1979. *Cosmical Magnetic Fields: Their Origin and their Activity*. Oxford Univ. Press.

Parker, E.N., 1993. A Solar Dynamo Surface Wave at the Interface Between Convection and Nonuniform Rotation. *Astrophys. J.* **408**, 707.

Perri, B. and Brandenburg, A., 2018. Spontaneous Flux Concentrations from the Negative Effective Magnetic Pressure Instability Beneath a Radiative Stellar Surface. *Astron. and Astrophys.* **609**, A99.

Powell, K.G., Gombosi, T.I, De Zeeuw, D.L., Ridley, A.J., Sokolov, I.V., Stout, Q.F. and Tóth, G., 2003. Parallel, Adaptive-Mesh-Refinement MHD for Global Space-Weather Simulations. In *Solar Wind Ten: Proceedings of the Tenth International Solar Wind Conference*, edited by M. Velli, R. Bruno and F. Malara. American Institute of Physics.

Priest, E., 1982. *Solar Magnetohydrodynamics*. D. Reidel Publ. Co.

Priest, E., 2014. *Magnetohydrodynamics of the Sun*. Cambridge Univ. Press.

Proctor, M.R.E., 2004. Solar Convection and Magnetic Fields. *Astron. Geophys.* **45**, 4.14.

Pugh, P., 2007. *Observing the Sun with CoronadoTM Telescopes*. Springer Science & Business Media.

Rast, M.P., 2003. The Scales of Granulation, Mesogranulation, and Supergranulation. *Astrophys. J.* **597**, 1200.

Rayleigh, L., 1916. On Convection Currents in a Horizontal Layer of Fluid, when the Higher Temperature is on the Under Side. *London, Ed. and Dub. Philos. Mag. and J. Sci.* **32**, 529.

Ryan, Ø., 2019. *Linear Algebra, Signal Processing, and Wavelets - A Unified Approach*. Springer Science & Business Media.

Ryan, S.G. and Norton, A.J., 2010. *Stellar Evolution and Nucleosynthesis*. Cambridge Univ. Press.

Scheiner, C., 1612. A More Accurate Disquisition Concerning Solar Spots and Stars [i.e., Satellites] Wandering around Jupiter. *Le Opere di Galileo Galilei.* **5**, 39.

Schmidt, G., 1966. *Physics of High-Temperature Plasmas.* Academic Press.

Schou, J., Scherrer, P.H., Bush, R.I., Wachter, R., Couvidat, S., Rabello-Soares, M.C., Bogart, R.S., Hoeksema J.T., Liu, Y., Duvall, T.L., Jr, Akin, D.J., Allard, B.A., Miles, J.W., Rairden, R., Shine, R.A., Tarbell, T.D., Title, A.M., Wolfson C.J., Elmore, D.F., Norton, A.A. and Tomczyk, S., 2012. Design and Ground Calibration of the Helioseismic and Magnetic Imager (HMI) Instrument on the Solar Dynamics Observatory (SDO). *Solar Phys.* **275**, 229.

Schwabe, S.H., 1843. Solar Observations during 1843. *Astron. Nachricht.* **20**, 495.

Schwarzschild, K., 1906. On the Equilibrium of the Sun's Atmosphere. *Nachrichten von der Königlichen Gesellschaft der Wissenschaften zu Göttingen. Math.-phys. Klasse.* **195**, 41.

Silvers, L.J., 2008. Magnetic Fields in Astrophysical Objects. *Philos. T. Roy. Soc.* **366**, 4453.

Silvers, L.J., Bushby, P.J., and Proctor, M.R.E., 2009. Interactions Between Magnetohydrodynamic Shear Instabilities and Convective Flows in the Solar Interior. *Mon. Not. Roy. Astron. Soc.* **400**, 337.

Solanki, S.K., 2003. Sunspots: An Overview. *Astron. and Astrophys. Rev.* **11**, 153.

Spiegel, E.A., 1965. Convective Instability in a Compressible Atmosphere. I. *Astrophys. J.* **141**, 1068.

Spiegel, E.A., 1971. Turbulence in Stellar Convection Zones. *Comments Astrophys. and Space Phys..* **3**, 53.

Spiegel, E.A., 1972. A History of Solar Rotation. *NASA Spec. Publ.* **300**, 61.

Spiegel, E.A. and Veronis, G., 1960. On the Boussinesq Approximation for a Compressible Fluid. *Astrophys. J.* **131**, 442.

Spiegel, E.A. and Weiss, N.O., 1980. Magnetic Activity and Variations in Solar Luminosity. *Nature*. **287**, 616.

Spiegel, E.A. and Zahn J.-P., 1992. The Solar Tachocline. *Astron. Astrophys.* **265**, 106.

Spitzer, L., 2006. *Physics of Fully Ionized Gases*. Dover Publ. Inc.

Squire, H.B., 1933. On the Stability for Three-Dimensional Disturbances of Viscous Fluid Flow between Parallel Walls. *Proc. R. Soc. A Math. Phys. Eng. Sci.* **142**, 621.

Steenbeck, M. and Krause, F., 1969. On the Dynamo Theory of Stellar and Planetary Magnetic Fields. I. AC Dynamos of Solar Type. *Astron. Nachr.*. **291**, 49.

Steenbeck, M., Krause, F. and Rädler, K.-H. 1966. Berechnung der mittleren Lorentz–Feldstärke $\boldsymbol{u}\times\boldsymbol{B}$ für ein elektrisch leitendes Medium in turbulenter, durch Coriolis–Kräfte beeinflußter Bewegung. *Z. Naturforschg.* **21a**, 369.

Stewart, I., 2016. *Calculating the Cosmos: How Mathematics Unveils the Universe*. Profile Books.

Stix, M., 2002. *The Sun: An Introduction*. Springer Science & Business Media.

Subramanian, R.S. and Balasubramaniam, R., 2001. *The Motion of Bubbles and Drops in Reduced Gravity*. Cambridge Univ. Press.

Süli, E. and Mayers, D., 2003. *An Introduction to Numerical Analysis*. Cambridge Univ. Press.

Thompson, W.B., 1951. Thermal Convection in a Magnetic Field. *Phil. Mag.* **42**, 1417.

Thompson, M.J., Christensen-Dalsgaard, J., Miesch, M.S. and Toomre, J., 2003. The Internal Rotation of the Sun. *Annu. Rev. Astron. Astrophys.* **41**, 599.

Tlatov, A.G., 2012. Long-Term Variations of the Solar Supergranulation Size According to the Observations in CaIIK Line. *Astrophys. and Space Sci. Proc.* **30**, 33.

Tobias, S.M., 2005. The Solar Tachocline. In *Fluid Dynamics and Dynamos in Astrophysics and Geophysics*, edited by A.M. Soward, C.A. Jones, D.W. Hughes and N.O. Weiss. CRC Press.

Tobias, S.M., 2009. The Solar Dynamo: The Role of Penetration, Rotation and Shear on Convective Dynamos. *Space Sci. Rev.*. **144**, 77.

Tobias, S.M., Brummell, N.H., Clune, T.L. and Toomre, J., 1998. Pumping of Magnetic Fields by Turbulent Penetrative Convection. *Astrophys. J.* **502**, L177.

Tobias, S.M., Brummell, N.H., Clune, T.L. and Toomre, J., 2001. Transport and Storage of Magnetic Field by Overshooting Turbulent Compressible Convection. *Astrophys. J.* **549**, 1183.

Tobias, S.M. and Hughes, D.W., 2004. The Influence of Velocity Shear on Magnetic Buoyancy Instability in the Solar Tachocline. *Astrophys. J.* **603**, 785.

Tobias, S.M. and Weiss, N.O., 2007. The Solar Dynamo and the Tachocline. In *The Solar Tachocline*, edited by D.W. Hughes, R. Rosner and N.O. Weiss. Cambridge Univ. Press.

Toomre, J., Hurlburt, N.E. and Massaguer, J.M., 1984. Strong Downward Plumes Resulting from Compressibility in Nonlinear Convection and their Coupling to Gravity Waves. In *Small-Scale Dynamical Processes in Quiet Stellar Atmospheres*, edited by S. Kiel. Sunspot: National Solar Observatory.

Van der Poel, E.P., Stevens, R.J.A.M. and Lohse, D., 2013. Comparison Between Two- and Three-Dimensional RayleighBnard Convection. *J. Fluid Mech.* **736**, 177.

Vasil, G.M. and Brummell, N.H., 2008. Magnetic Buoyancy Instabilities of a Shear-Generated Magnetic Layer. *Astrophys. J.* **686**, 709.

Vickers, G.T., 1971. On the Formation of Giant Cells and Supergranules. *Astrophys. J.* **163**, 363.

Vita-Finzi, C., 2008. *The Sun: A User's Manual*. Springer Science & Business Media.

Watanabe, S. and Shibahashi, H., 2001. Solar Models with Helioseismic Constraints and the Solar Neutrino Problem. *Publ. Astron. Soc. Japan.* **53**, 565.

Weiss, N.O., 1981. Convection in an Imposed Magnetic Field. Part 1. The Development of Nonlinear Convection. *J. Fluid Mech.* **108**, 247.

Weiss, N.O., Brownjohn, D.P., Matthews, P.C. and Proctor, M.R.E., 1996. Photospheric Convection in Strong Magnetic Fields. *Mon. Not. Roy. Astron. Soc.* **283**, 1153.

Weiss, N.O. and Proctor, M.R.E., 2014. *Magnetoconvection*. Cambridge Univ. Press.

Weiss, N.O., Thomas, J.H., Brummell, N.H. and Tobias, S.M., 2004. The Origin of Penumbral Structure in Sunspots: Downward Pumping of Magnetic Flux. *Astrophys. J.* **600**, 1073.

Wiegelmann, T., Thalmann, J.K. and Solanki, S.K., 2014. The Magnetic Field in the Solar Atmosphere. *Astron. Astrophys. Rev.* **22**, 78.

Wissink, J.G., Hughes, D.W., Matthews, P.C. and Proctor, M.R.E., 2000. The Three-Dimensional Breakup of a Magnetic Layer. *Mon. Not. Roy. Astron. Soc.* **318**, 501.

Witzke, V., Silvers, L.J. and Favier, B., 2015. Shear Instabilities in a Fully Compressible Polytropic Atmosphere. *Astron. Astrophys.* **577**, A76.

Wriggers, P., 2008. *Nonlinear Finite Element Methods*. Springer Science & Business Media.

Yoshizawa, A., Itoh, S.I. and Itoh, K., 2002. *Plasma and Fluid Turbulence: Theory and Modelling*. CRC Press.

Żak, S.H., 2013, *Notes on Tools for Analysis of Dynamic Systems: Lyapunovs Methods*. Purdue Univ.

Zappoli, B., Beysens, D. and Garrabos, Y., 2014. *Heat Transfers and Related Effects in Supercritical Fluids*. Springer Science & Business Media.

Zel'dovich, Y.B., 1957. The Magnetic Field in the Two-Dimensional Motion of a Conducting Turbulent Liquid. *Sov. Phys. JETP*. **4**, 460.

Zhang, M. and Feng, X., 2016. A Comparative Study of Divergence Cleaning Methods of Magnetic Field in the Solar Coronal Numerical Simulation. *Front. Astron. Space Sci.* **3**, 1.

Zwaan, C., 1985. The Emergence of Magnetic Flux. *Sol. Phys.* **100**, 397.